INFORMATION TO USERS

This manuscript has been reproduced from the microfilm master. UMI films the text directly from the original or copy submitted. Thus, some thesis and dissertation copies are in typewriter face, while others may be from any type of computer printer.

The quality of this reproduction is dependent upon the quality of the copy submitted. Broken or indistinct print, colored or poor quality illustrations and photographs, print bleedthrough, substandard margins, and improper alignment can adversely affect reproduction.

In the unlikely event that the author did not send UMI a complete manuscript and there are missing pages, these will be noted. Also, if unauthorized copyright material had to be removed, a note will indicate the deletion.

Oversize materials (e.g., maps, drawings, charts) are reproduced by sectioning the original, beginning at the upper left-hand corner and continuing from left to right in equal sections with small overlaps. Each original is also photographed in one exposure and is included in reduced form at the back of the book.

Photographs included in the original manuscript have been reproduced xerographically in this copy. Higher quality 6" x 9" black and white photographic prints are available for any photographs or illustrations appearing in this copy for an additional charge. Contact UMI directly to order.

U·M·I

University Microfilms International
A Bell & Howell Information Company
300 North Zeeb Road Ann Arbor MI 48106-1346 USA
313 761-4700 800 521-0600

Order Number 9304747

Resonant nuclear reaction analysis of solid state materials

Yan, Dong, Ph.D.

City University of New York, 1992

U·M·I
300 N. Zeeb Rd.
Ann Arbor, MI 48106

RESONANT NUCLEAR REACTION ANALYSIS OF SOLID STATE MATERIALS

by

DONG YAN

A dissertation submitted to the Graduate Faculty in Physics
in partial fulfillment of the requirements for the degree of
Doctor of Philosophy, The City University of New York

1992

This manuscript has been read and accepted for the Graduate Faculty in Physics in satisfaction of the dissertation requirement for the degree of Doctor of Philosophy.

9/14/92	Prof. Peter M. S. Lesser
Date	Chair of Examining Committee
9/23/92	Prof. Joseph B. Krieger
Date	Executive Officer

Prof. Walter M. Gibson

Prof. Marvin H. Mittleman

Prof. Pedro A. Montano

Prof. Carl M. Shakin

Supervisory Committee

The City University of New York

Abstract

RESONANT NUCLEAR REACTION ANALYSIS OF SOLID STATE MATERIALS

by

DONG YAN

Advisor: Professor Peter M. S. Lesser

We have explored the application of resonant nuclear reaction analysis (RNRA) to the characterization of solid state materials. A wide range of subjects, from semiconductor physics to electro-chemistry, has been included in this study. We have shown that, with a proper choice of resonance and careful normalization, RNRA can be far superior to conventional ion beam analysis using Rutherford backscattering.

The 0.992-MeV resonance in the reaction $^{27}Al(p,\gamma)^{28}Si$ was used to measure the aluminum composition, x, of $Al_xGa_{1-x}As$ samples on GaAs substrates. It was shown that the RNRA determination of x was substantially free of corrections and best represented the true bulk value. The relation between energy gap and composition was established by correlating RNRA

results to low temperature photoluminescence measurements. We also observed the transition from direct to indirect band gap at a composition x=0.37.

The 0.441-MeV resonance in the reaction $^7Li(p,\gamma)^8Be$ was used to profile the lithium depth distribution in electro-deposited amorphous MoS_3 thin film samples. The absolute amount of lithium detected was in close agreement with electro-chemical calculations based on charging conditions. This measurement provided an independent verification of lithium intercalation in amorphous MoS_3.

The 3.05-MeV resonance in the reaction $^{16}O(\alpha,\alpha)^{16}O$ was used to detect oxygen in TiC and WC superlattices on silicon substrates. Oxygen was found throughout the TiC samples, but only at the surface of WC samples. These observations were in agreement with Auger and electron energy loss measurements. The absence of oxygen at interfaces in WC superlattices suggests that they will be quite stable at high temperatures.

The 0.992-MeV resonance in the reaction $^{27}Al(p,\gamma)^{28}Si$ was used to measure the energy loss and straggling of channeled 1-MeV protons near the (001) channeling direction in silicon. The measured angular dependence of the

energy loss agreed very well with earlier results, and the straggling parameter showed an interesting angular-dependent behavior which could largely be attributed to an "averaging" effect of partially channeled ions.

DEDICATIONS

To my parents

for providing a home to grow up in full of love and support

To my fiancée, Irene

for her care, enthusiasm, and encouragement

ACKNOWLEDGEMENTS

I wish to thank my thesis committee members, Profs. Walter M. Gibson, Marvin H. Mittleman, Pedro A. Montano, Carl M. Shakin, and Carroll C. Trail, and especially my mentor, Prof. Peter M. S. Lesser, for their supervisory, guidance, and encouragement. Prof. Lesser's intuitive thoughts have always been a source of inspiration. He worked harder than me in almost every single experiment, from initiation, design to the actual "dirty" work of apparatus setup, data collection and analysis. I am also grateful to Prof. Ming-kung Liou for many helpful discussions.

I have benefitted greatly from former members of the Brooklyn College Dynamitron lab. Dr. Han-sheng Jin's expertise in ion beam analysis and channeling played an indispensable role in the modification and eventually successful operation of the channeling apparatus on the beam line. Mr. Ted Lubicich and William Steuber did an excellent job in keeping up the accelerator which made everything possible. And thanks go to my former fellow graduate students, Drs. Noel A. Guardala, Gardy Cadet, Mr. Jia-nian Feng, Xiao-wen Wu, Huang-he Chen, and Ms. Fei Yao, who together created a warm and friendly

environment and made my life as a graduate student enjoyable and memorable.

I am very much indebted to Prof. Fred H. Pollak who brought to me the world of solid state physics. His exceptional knowledge and heavy participation was the key to success in many of the projects. I also wish to thank members of Brooklyn College Semiconductor Institute, Drs. Edward G. L. Look, Xiao-ming Yin, Mr. Qiang Hao and Yi-chun Yin. Drs. Yan Li and Yuet-loy Chan of Brooklyn College, Hong-en Shen of U.S. Army Electronics and Device lab, and Ying-sheng Huang of the National Taiwan Institute of Technology also provided enormous help and are greatly acknowledged.

Last, but not least, my deepest appreciation goes to my fiancée, Irene, for her understanding, support, as well as patience and confidence in me throughout the years of unsettled life as a graduate student.

TABLE OF CONTENTS

Page

Approval Page ii

Abstract iii

Dedications vi

Acknowledgements vii

List of Tables xii

List of Figures xiii

CHAPTER ONE

Determination of absolute aluminum concentration in $Al_xGa_{1-x}As$ 1

Introduction 1

Background 5

Basic formalism 9

Details of sample preparation 15

Details of experimental setup 16

Details of experiment 23

Discussion of errors and corrections 27

1) Other resonances in the $^{27}Al(p,\gamma)^{28}Si$ reaction 27

2) Channeling 28

3) Straggling 33

4) Contribution to γ-ray yield from $^{15}N(p,\gamma)$ and $^{19}F(p,\alpha\gamma)$ resonances 33

Results and summary 35

CHAPTER TWO

Ion beam analysis of lithium in amorphous MoS_3 40

Introduction 40

The $^{7}Li(p,\gamma)^{8}Be$ reaction at 0.441 MeV 43

RBS cross section 45

Lithium determination 49

Depth profiling 52

Experiment details 57

1) Details of electrochemical analysis 57

2) Details of ion beam analysis 58

3) Identification of features in RBS spectra 63

Discussion and summary 70

CHAPTER THREE

Oxygen measurements in TiC and WC superlattices 75

Introduction 75

Rutherford scattering versus resonant scattering 79

Sample structures 83

Stopping power of ^{4}He in TiC and WC superlattices 87

Details of experiment 90

1) Sample preparation 90

2) Backscattering measurements 91

Results and discussion 92

Summary 103

CHAPTER FOUR

Energy loss and straggling measurements of channeled 1 MeV protons in silicon (001) 104

Introduction 104

Energy loss and straggling in amorphous materials 106

Energy loss and straggling of channeled ions 110

Experimental methods 114

Our study 122

Data analysis 128

Discussion 137

Appendix 142

Bibliography 145

LIST OF TABLES

Page

Table 1.1 Relative yields of the resonances of $^{27}Al(p,\gamma)^{28}Si$ reaction near 1 MeV 28

Table 1.2 Summary of the absolute aluminum composition measurements in $Al_xGa_{1-x}As$ 36

Table 3.1 Configurations of titanium-carbon and tungsten-carbon superlattice samples 84

Table 4.1 Result of energy loss and straggling measurement of 1 MeV H^+ on silicon (001) 136

LIST OF FIGURES

Page

Figure 1.1 Excitation function of the $^{27}Al(p,\gamma)^{28}Si$ reaction 6

Figure 1.2 Stopping power of H^+ in $Al_xGa_{1-x}As$ as a function of energy 14

Figure 1.3 Schematic diagram of the Brooklyn College 3.75-MV Dynamitron accelerator 17

Figure 1.4 Schematic representation of the target chamber for aluminum concentration measurements 19

Figure 1.5 Schematic representation of the electronics block diagram 21

Figure 1.6 RBS spectrum of ~ 1 MeV H^+ on sample P735 (1.1 μm $Al_xGa_{1-x}As$ layer, x=0.825) 25

Figure 1.7 Gamma-ray spectrum of the $^{27}Al(p,\gamma)^{28}Si$ reaction at 0.992 MeV on an AlAs sample 26

Figure 1.8 Relative yields of the resonances of $^{27}Al(p,\gamma)^{28}Si$ reaction near 1 MeV 29

Figure 1.9 Ratio of γ-ray yield to RBS yield as a function of incident angle 32

Figure 1.10 Band-gap of $Al_xGa_{1-x}As$ as a function of alloy composition, x 37

Figure 2.1 Rutherford backscattering on a compound target 48

Figure 2.2 Stopping power of H^+ in MoS_3Li_x 54

Figure 2.3 Energy-depth relation of H^+ in MoS_3Li_x 55

Figure 2.4 Charging-Discharging curve of lithium in MoS_3 59

Figure 2.5 Representative γ-ray spectrum of the $^{7}Li(p,\gamma)^{8}Be$ reaction 60

Figure 2.6 Dynamitron accelerator energy calibration 62

Figure 2.7 Backscattering spectrum of ED-MoS_3(Na)/Ni 64

Figure 2.8 Backscattering spectrum of ED-MoS_3(A)/ITO 65

Figure 2.9 Backscattering spectrum of TD-MoS_3 66

Figure 2.10 Backscattering spectrum of LiF 67

Figure 2.11 Backscattering spectrum of LiCl 68

Figure 2.12 Lithium depth profile of ED-MoS_3(NA)/Ni 71

Figure 2.13 Lithium depth profile of ED-MoS_3(A)/ITO 72

Figure 2.14 Lithium depth profile of TD-MoS_3 73

Figure 3.1 Excitation function of the $^{16}O(\alpha,\alpha)^{16}O$ reaction 80

Figure 3.2 Structure of a titanium carbon superlattice sample 85

Figure 3.3 Structure of a tungsten carbon superlattice sample 86

Figure 3.4 Energy-depth relation of ^{4}He in TiC and WC 88

Figure 3.5 Backscattering spectrum of 2.2 MeV ^{4}He on TiC 93

Figure 3.6 Backscattering spectrum of 3.06 MeV ^{4}He on TiC 94

Figure 3.7 Backscattering spectrum of 3.08 MeV ^{4}He on TiC 96

Figure 3.8 Backscattering spectrum of 3.06 MeV ^{4}He on WC 98

Figure 3.9 Backscattering spectrum of 3.10 MeV ^{4}He on WC 99

Figure 3.10 Backscattering spectrum of 3.18 MeV ^{4}He on WC . . . 100

Figure 3.11 Excitation function of the $^{12}C(\alpha,\alpha)^{12}C$ reaction 102

Figure 4.1 Energy loss and straggling measurement - transmission geometry 115

Figure 4.2 Energy loss and straggling measurement - backscattering geometry 117

Figure 4.3 Energy loss and straggling measurement - resonant nuclear reaction method 119

Figure 4.4 Schematic diagram of the target chamber for energy loss and straggling measurements 125

Figure 4.5 Cross sectional profile of a thin silicon (001) crystal sample 126

Figure 4.6 Backscattering spectra of 1 MeV H^+ near silicon (001), random and aligned 129

Figure 4.7 Backscattering yield of 1 MeV H^+ near silicon (001) as a function of incident angle 132

Figure 4.8 Representative least-squares fit of the $^{27}Al(p,\gamma)^{28}Si$ γ yield function 135

Figure 4.9 Energy loss of 1 MeV H^+ near silicon (001) as a function of angle 138

Figure 4.10 Straggling of 1 MeV H^+ near silicon (001) as a function of angle 140

Chapter One

Determination of Absolute Aluminum Concentration in $Al_xGa_{1-x}As$

Introduction

The $Al_xGa_{1-x}As$ material system (where $0<x<1$) has been the focus of a great deal of study as one of the most promising among new types of semiconductor materials. Applications include devices such as cw room temperature lasers[1], quantum well lasers[2], modulation doped high electron mobility transistors[3], and high efficiency solar cells[4,5], to mention a few. As with many other ternary alloys, the electronic and optical properties of such a material, and therefore the properties of the devices made from it, depend strongly on the alloy composition x. For example, the energy gap of GaAs ($x=0$) is 1.42 eV (direct band gap material), that of AlAs ($x=1$) is 2.95 eV (indirect band gap material). It is relatively easy to detect even a fraction of a percent change in x by optical techniques such as photoreflectance (PR) and photoluminescence (PL), which measure the fundamental energy gap, E_g, of the material to within a few meV. Other techniques, such as Raman scattering spectroscopy (RSS), are also sensitive to composition. However, the relation

between fundamental energy gap and alloy composition for these (secondary) optical techniques, or phonon frequency versus alloy composition for RSS, must be determined experimentally. A linear interpolation between the values of the two end-points (x=0 and 1) is generally incorrect. Without an independent calibration, the optical techniques are limited to detecting relative changes in the alloy composition only, not the absolute amount. Even when such a calibration is established by some primary technique, the precision of optical measurements cannot exceed that of the primary technique.

Prior to this study, the most widely accepted primary technique for determining alloy composition, x, was the electron x-ray microprobe (EM) measurement of the x-ray intensity (yield) from Al and/or Ga and As atoms.[6-12] Because of the strong absorption process involved in the interaction of x-rays with matter, EM requires complicated correction procedures to account for the change in x-ray yield due to so-called "matrix effects." It is also a very time-consuming technique. Another widely used technique, Auger electron spectroscopy (AES), requires layer removal (by sputtering) to eliminate surface oxides and other impurities which interfere with the AES measurements.[12-14] However, the surface-sensitive AES may very well see an alloy composition quite different from that of bulk epilayer because of sputtering-induced surface

changes. Secondary ion mass spectroscopy (SIMS) can also be used to measure alloy composition. This destructive technique provides great depth sensitivity but its determination of absolute quantity is poor. The scatter of values for the relationship between E_g and x for $Al_xGa_{1-x}As$ in the existing literature, not only between different techniques, but also between different laboratories using the same technique, is a good indication of the systematic errors hidden in these measurements. For example, the change in fundamental energy gap with composition, $\Delta E_g/\Delta x$, has been reported by different authors to be from 12.5 meV/%[9] to 16.1 meV/%.[10] Since the optical techniques are well understood, the major contribution to the spread in values is likely to come from uncertainties in the determination of alloy composition.

Recently, the method of resonant nuclear reaction analysis (RNRA, sometimes also referred to as nuclear reaction analysis, NRA), together with Rutherford backscattering spectrometry (RBS), has been demonstrated to be a very promising technique for the depth profiling of an epitaxial layer of $Al_xGa_{1-x}As$ on GaAs.[15,16] By utilizing the very strong and sharp (p,γ) resonance on ^{27}Al at E_p = 0.922 MeV, the depth distribution of the Al concentration in $Al_xGa_{1-x}As$ can be precisely determined.[15] The same technique, with some modifications, can be used to measure the aluminum

composition absolutely.[17,18] Ions with energies in excess of ~ 0.5 MeV are, to a large extent, insensitive to surface conditions and details of the sample's electronic structure. With a penetration depth of the order of 10^4 Å, the alloy concentration determined this way represents the true bulk value. The energy of the γ-rays produced in the $^{27}Al(p,\gamma)$ reaction is of the order of 10 MeV and the sample is completely transparent to these γ-rays. Although the measurements are very time-consuming, data obtained from this nuclear technique are quite free of complicated, ambiguous corrections and other calibrations and/or data-modeling difficulties, and thus provide a very reliable absolute determination of x. Once the secondary optical techniques have been calibrated, their full power can be used to obtain fast and accurate determinations of the alloy composition. The same approach can also be applied to other important semiconductor materials containing aluminum, such as $Al_xGa_{1-x}Sb$ and $Al_xIn_{1-x}As$.

Background

Many light isotopes (A<40) exhibit strong, sharp resonances in elastic scattering and/or reactions with protons (H^+). In particular, for those whose masses are one less than a magic number, i.e., closed shell or subshell for protons (^{7}Li, ^{15}N, ^{19}F, ^{27}Al, etc.), the (p,γ) reaction is energetically favorable because it leads to a much more stable nucleus. The large positive Q-value results in formation of the final nucleus at very high excitation energy and its subsequent decay to the ground state is accomplished by the emission of one or more high-energy γ-rays. Figure 1.1 shows the cross section as a function of incident proton energy (excitation curve) for the reaction ^{27}Al(p,γ)^{28}Si.[19] One of the strongest isolated resonances occurs at a laboratory proton energy of 0.992 MeV. Most of the peaks (resonances) in this reaction have accompanying γ-rays of energy about 10 MeV, a region that is well above natural background radioactivity.

The γ-ray yield from the ^{27}Al(p,γ)^{28}Si resonant reaction is proportional to the number of aluminum nuclei in the target material. If a resonance is strong and well isolated and narrow enough, it can be used to probe the depth

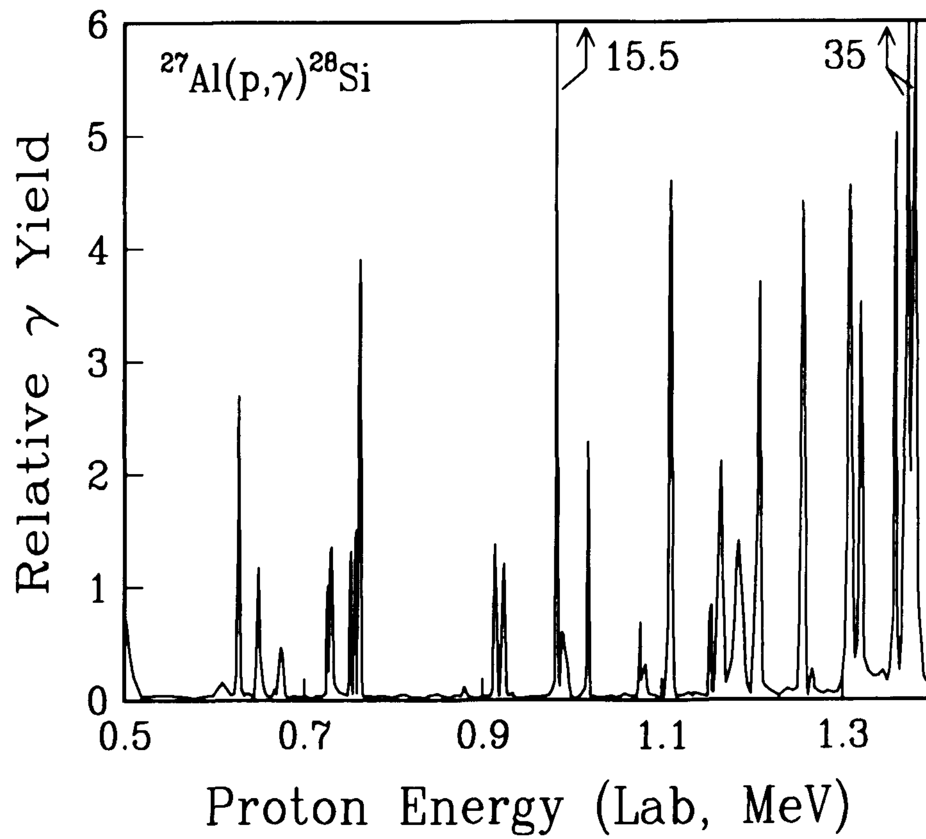

Figure 1.1 Excitation function of the $^{27}Al(p,\gamma)^{28}Si$ reaction. The strong resonance at 0.992 MeV is used in the measurements. From ref. 19.

distribution of aluminum in a sample owing to the fact that the incident proton beam loses energy as it penetrates the target. Thus, the resonant yield of γ-rays occurs only for a very narrow (in depth) region of the target in which the proton energy is "on resonance" and the aluminum is detected exclusively within that narrow region. The region to be sampled within the target can be moved to greater depth simply by increasing the incident beam energy. The depth resolution of this method, near the sample surface, is determined by the width of the resonance; deeper in the sample, the depth resolution is limited by energy straggling of the incident beam. With a suitable resonance, the sensitivity and depth resolution of the resonant reaction technique is far better than conventional RBS, whose depth resolution is limited by the detector resolution, which is typically ~ 20 keV. Thus, for the purpose of high-resolution depth profiling, the $^{27}Al(p,\gamma)$ reaction is superior to RBS. However, simultaneous RBS measurements may be useful in providing a more reliable normalization than direct beam current integration. The proportionality of the γ-ray yield to the number of aluminum atoms can be utilized, together with RBS, and a careful normalization procedure, to measure also the absolute alloy composition in $Al_xGa_{1-x}As$. Since most of the systematic errors are canceled completely by the normalization procedure, the resulting determination of alloy composition does not depend on complicated corrections. The precision of this method can be

made close to 1% in the alloy composition.[17,18]

Another feature that makes RNRA superior to RBS is its high sensitivity to light nuclei. It is well known that RBS is best suited for heavy (high atomic number) impurities residing on surfaces of light substrates. In such a configuration and under optimal conditions, RBS can detect a few monolayers of surface impurity or 0.1% in the bulk. On the other hand, determination of light elements in the presence of heavy elements by RBS can be a very tricky and difficult business. The mass resolution of RBS is not very good, unless it is in the light mass (and therefore not so sensitive) region. For example, a ~ 1 MeV proton beam cannot distinguish signals from Ga and As. RNRA has no such limitations.

Basic Formalism

Let Y_γ be the (p,γ) reaction yield and Y_{RBS} the RBS yield, respectively. For an incident beam with a Gaussian energy distribution much wider than the resonance width[20],

$$Y_\gamma \propto \int_0^\infty \rho_{Al}(z) e^{-\frac{(E(z)-E_R)^2}{2\Omega^2(z)}} dz \tag{1.1}$$

where E(z), Ω(z) are the beam energy distribution parameters (centroid and width) at depth z, E_R is the resonance energy, and ρ(z) is the density of aluminum atoms at depth z. Among the proportionality constants are the detector efficiency and geometry factors, magnitude of the cross section, integrated beam current (dosage), etc. For our purpose we require that the whole width of the resonance be within the sample $Al_xGa_{1-x}As$ layer, and that the aluminum concentration be constant within this layer, so ρ(z) is a constant proportional to x, the alloy composition. Therefore,

$$Y_\gamma \propto \rho_{Al} \int_{E_0}^{0} e^{-\frac{(E(z)-E_R)^2}{2\Omega^2(z)}} dE \left[-\frac{dE}{dz}\right]^{-1} \tag{1.2}$$

where E_0 is the incident beam energy. Further, the stopping power dE/dz is a

slowing varying function of energy (and, therefore, depth as well), so, to a very good approximation,

$$Y_{\gamma} \propto \rho_{Al} \left[\frac{dE}{dz} \right]^{-1}_{E=E_R} \qquad (1.3)$$

For the RBS yield within a backscattered energy window (region of interest, or ROI) of E_1' and E_2', we have[21],

$$\begin{aligned} Y_{RBS} &\propto \int_{E_1(z)}^{E_2(z)} \left[\rho_{Ga} Z_{Ga}^2 + \rho_{As} Z_{As}^2 \right] \frac{1}{E^2} \left[\frac{dE}{dz} \right]^{-1} dE \\ &\propto \left[\rho_{Ga} Z_{Ga}^2 + \rho_{As} Z_{As}^2 \right] I(E_1,E_2) \end{aligned} \qquad (1.4)$$

where Z is the atomic number. In Eqn. (1.4) the Rutherford cross section is separated into two parts, the Z^2 dependence and the $1/E^2$ dependence, and

$$I(E_1,E_2) = \int_{E_1(z)}^{E_2(z)} \frac{1}{E^2} \left[\frac{dE}{dz} \right]^{-1} dE \qquad (1.5)$$

represents the integral of the reciprocal stopping power and includes the $1/E^2$ dependence over an energy range of E_1 to E_2 (energy before scattering) corresponding to the end-point energies of the ROI. As mentioned earlier, RBS cannot separate the signals from Ga and As, so both are included in the integral.

Both the reciprocal stopping power $(dE/dz)^{-1}$ and integration limits E_1, E_2 will depend slightly on alloy concentration.

We define a double ratio, R, to be the ratio of γ-ray yield to RBS yield of a sample with composition x to that of a standard with known composition x_0 (normally AlAs, $x_0=1$),

$$R = \frac{\left[Y_\gamma / Y_{RBS}\right]_x}{\left[Y_\gamma / Y_{RBS}\right]_{x_0}} \tag{1.6}$$

Because $\rho_{Al} \propto x$, $\rho_{Ga} \propto 1-x$, $\rho_{As} \propto 1$, and using Eqn. (1.3), we have

$$R = \frac{x\left[\frac{dE}{dz}\right]^{-1}_{E=E_R,x}}{\left[Z^2_{As} + (1-x)\,Z^2_{Ga}\right] I_x} \Bigg/ \frac{x_0\left[\frac{dE}{dz}\right]^{-1}_{E=E_R,x_0}}{\left[Z^2_{As} + (1-x_0)\,Z^2_{Ga}\right] I_{x_0}} \tag{1.7}$$

or

$$x = \frac{(1+B)R}{A[1+B(1-x_0)]/x_0 + BR} \tag{1.8}$$

where

$$A = \left(I_{x_0}\left[\frac{dE}{dz}\right]_{x_0}\right) \Big/ \left(I_x\left[\frac{dE}{dz}\right]_x\right) \tag{1.9}$$

$$B = \left(Z_{Ga} / Z_{As} \right)^2 = 0.88246 \tag{1.10}$$

and I_x, I_{x_0} are the integrals of Eqn. (1.5) for sample (x) and standard (x_0), respectively.

When x_0=1,

$$x = \frac{(1+B)\ R}{A\ +\ B\ R} \tag{1.11}$$

The only correction term here is A, which itself is a ratio of integrations of stopping powers and Rutherford cross sections. The stopping powers for all elements have extensive tabulations in the literature, such as that of Ziegler.[22] The accuracy of these tables is about 5%. The stopping power of a compound such as $Al_xGa_{1-x}As$ is related to its compositional elements by Bragg's additivity law:[20,22]

$$\left[\frac{dE}{dz}\right]_{Al_xGa_{1-x}As} = x\left[\frac{dE}{dz}\right]_{Al} + (1-x)\left[\frac{dE}{dz}\right]_{Ga} + \left[\frac{dE}{dz}\right]_{As} \tag{1.12}$$

Figure 1.2 shows the stopping power of $Al_xGa_{1-x}As$ for various alloy

compositions, x, based on ref. 22. Since A is a ratio of stopping power over a narrow range of energy, most of the uncertainties associated with the tabulation will cancel, resulting in A being very close to unity. This normalization scheme works well in this particular case because the sample and the standard are very closely matched in terms of atomic density and stopping power.

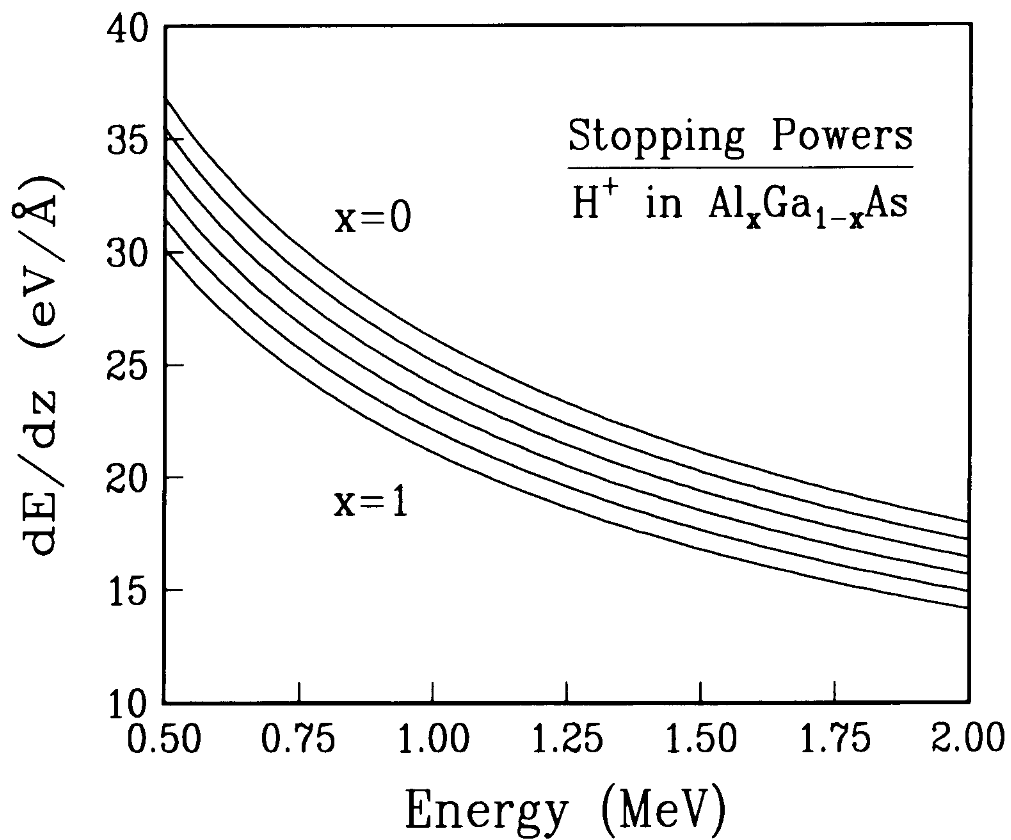

Figure 1.2 Stopping power of H^+ in $Al_xGa_{1-x}As$ as a function of energy (x=0, 0.2, 0.4, 0.6, 0.8 and 1). From Ref. 22.

Details of Sample Preparation

All samples for the absolute x measurement were grown by metal-organic vapor phase epitaxy (MOVPE). They consisted of high quality $Al_xGa_{1-x}As$ films grown on GaAs substrates oriented [100] → 2° [110]. Some samples grown by liquid phase epitaxy (LPE) (most of them with high x) were also used. The alloy compositions covered most of the region from 0 to 1, except for very low (<0.1) and very high (>0.85) values of x. Thicknesses of these samples ranged from 0.8 μm to about 3 μm. The AlAs crystals (standards) were either 2 or 3 μm thick. All samples underwent low temperature (2K) PL measurements and had their alloy concentrations determined by EM prior to ion beam analysis. They then were treated by ion implantation to destroy their perfect crystallinity. This was necessary in order to eliminate strong channeling behavior which would greatly affect the ion beam measurements. The ion implantation was done at room temperature in two steps: 1) 80-keV Ar^+ ions at a dose of 1×10^{15} cm^{-2}, followed by 2) 150-keV Ar^+ ions at a dose of 3×10^{15} cm^{-2}. The AlAs crystals were given a GaAs cap layer, ranging from 100 to 250 Å thick, to prevent them from deteriorating from oxidation before and during study. Some of the AlAs samples were also coated with a layer of SiN_2 (~ 1000Å).

Details of Experimental Setup

The ion beam determination of absolute x concentration was done using the Brooklyn College Dynamitron accelerator (Fig. 1.3). It is a single-ended, 3.75-MV electrostatic accelerator with a beam energy resolution of about 2 keV and is capable of producing up to 2mA of beam current. For the present analysis, an H^+ (proton) beam of ~ 1 MeV energy and a current of ~ 100 nA was used. In the beam transport system, after leaving the accelerator, the beam passes through electrostatic quadrupole (focusing) and electrostatic steering plates before entering the energy selecting magnet. The magnet has a pair of slits at its two focal points which restricts the passage of beam. The image slits are also connected to the slit feedback system which regulates the energy of the accelerator. A second magnet switches the beam to one of the three beam lines. The beam then passes through a magnetic quadrupole focusing unit and a pair of slits (6 mm and 1 mm) before finally getting into the target chamber. The resulting beam on the target sample was about 1 mm in diameter. The whole beam path, including samples and particle detectors, was maintained at high vacuum (10^{-6} to 10^{-7} Torr) by turbo-molecular and cryogenic pumps. A liquid nitrogen cold sleeve was near the target chamber to help reduce carbon build-up

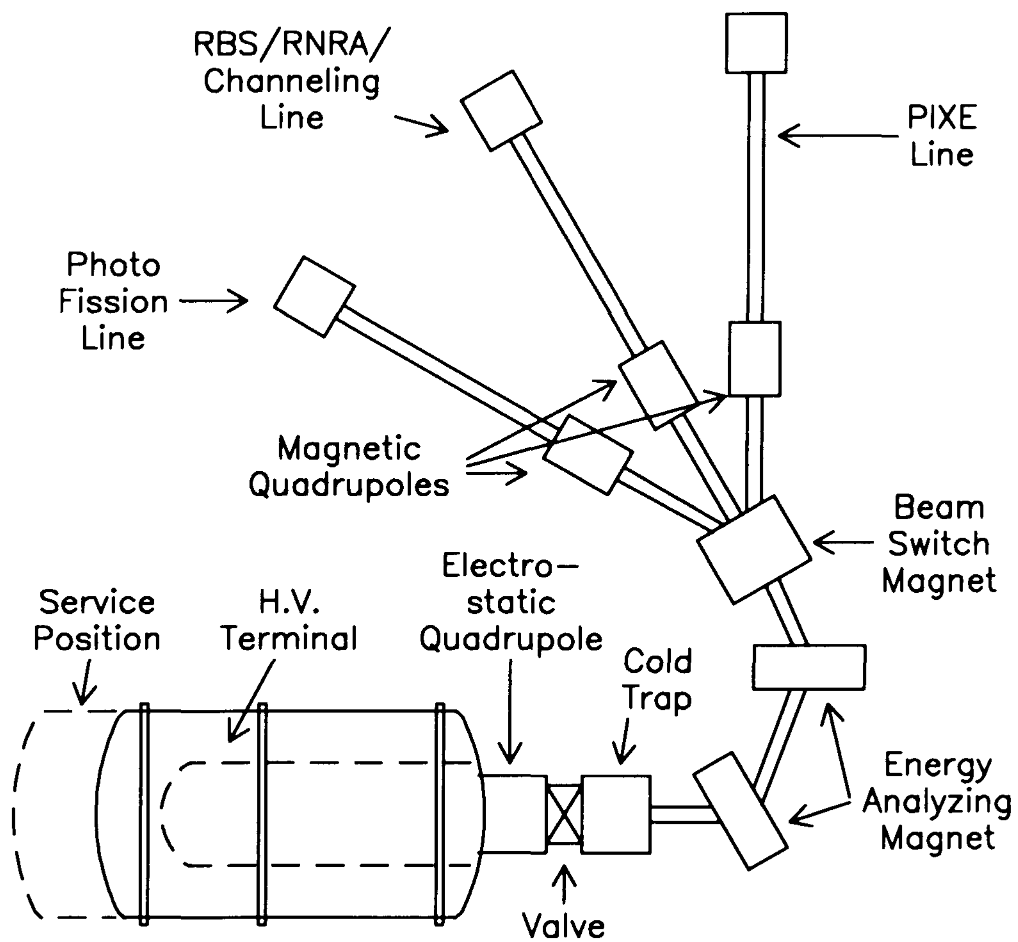

Figure 1.3 Schematic diagram of the Brooklyn College 3.75-MV Dynamitron accelerator (top view).

on the target.

Up to 4 pieces of $Al_xGa_{1-x}As$ and/or AlAs could be mounted at one time on the target holder, a ~ 1/2 inch square copper block, which was at the center of a 17-inch scattering chamber and connected to the shaft of a rotational vacuum feed-through, allowing different samples or different orientations of the same sample to face the incident beam (Fig. 1.4). The smallest step size achievable on the feed-through was about 0.5°. To avoid the possibility of the beam partially missing the target, for samples smaller than about 4×4 mm^2, it was necessary to cover the sample with a piece of high purity (99.99%) tantalum sheet, exposing sample only through a small circular hole at the center of the tantalum. The heavy mass and high Rutherford cross section of tantalum allowed quick identification even if only a small amount of beam was hitting the tantalum outside the sample. The sample block also served as the target current collecting device (Faraday Cup). No attempt was made to suppress the secondary electron emission to get a more accurate current reading, since it was not used as the normalization for data analysis.

Two silicon surface barrier detectors were used to collect backscattered particles (protons). These were placed at $\pm172.5^{\circ}$ with respect to the incident

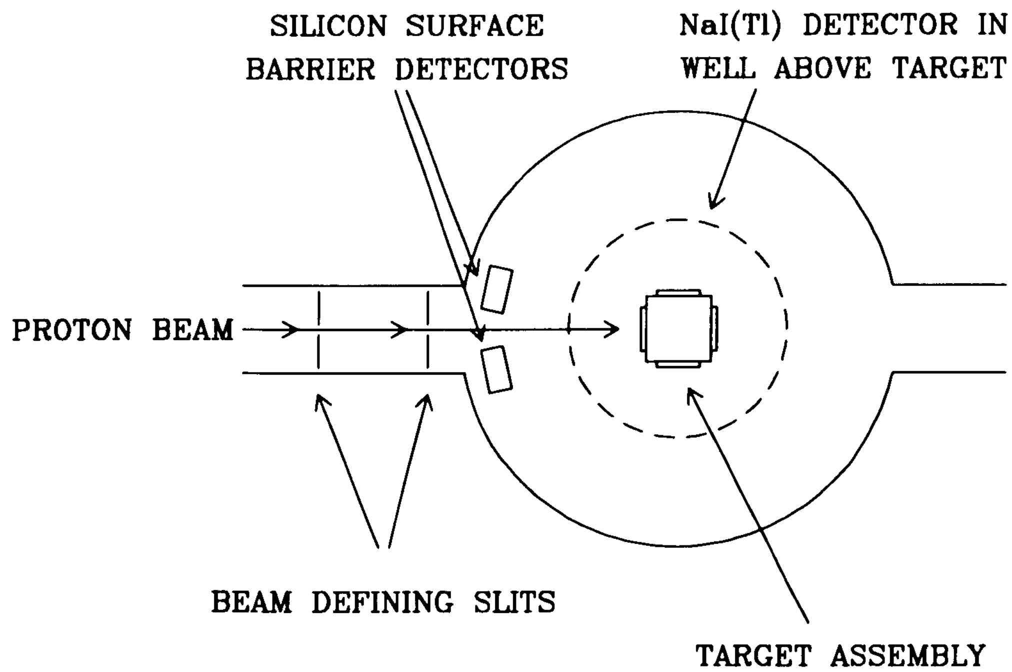

Figure 1.4 Schematic representation of the target chamber (top view).

beam direction. The combination of detector aperture and distance gave a solid angle of about 0.3 msr each, with a counting rate of about 6000 counts/second. The γ-ray detector was a standard 3×3 in. NaI(Tl) crystal positioned outside the scattering chamber on top of the target assembly. It was placed as close to the beam spot as possible (~ 1/2 inch), giving a solid angle of almost 2π steradians. The counting rate of the γ-ray detector for an AlAs sample was about 100 counts/second, within an ROI of 5 to 12 MeV. Background was virtually absent.

Figure 1.5 shows the electronics block diagram. Each of the detectors was accompanied by a bias supply, a pre-amplifier and a main amplifier. The pre-amplifier was adjacent to the detector to perform preliminary amplification and shaping before signals underwent a lengthy co-axial cable transmission (~ 300 feet) from the accelerator vault to the control room. The main amplifier was responsible for further shaping, filtering and amplification. The pulses were finally collected in multi-channel analyzers (MCA's), where each pulse was accumulated according to its pulse height, which is proportional to the energy of the particle striking the detector. For each $Al_xGa_{1-x}As$ sample analyzed as well as each AlAs standard, both RBS and γ-ray spectra were taken simultaneously. An IBM PC was linked to the MCA to facilitate data storage

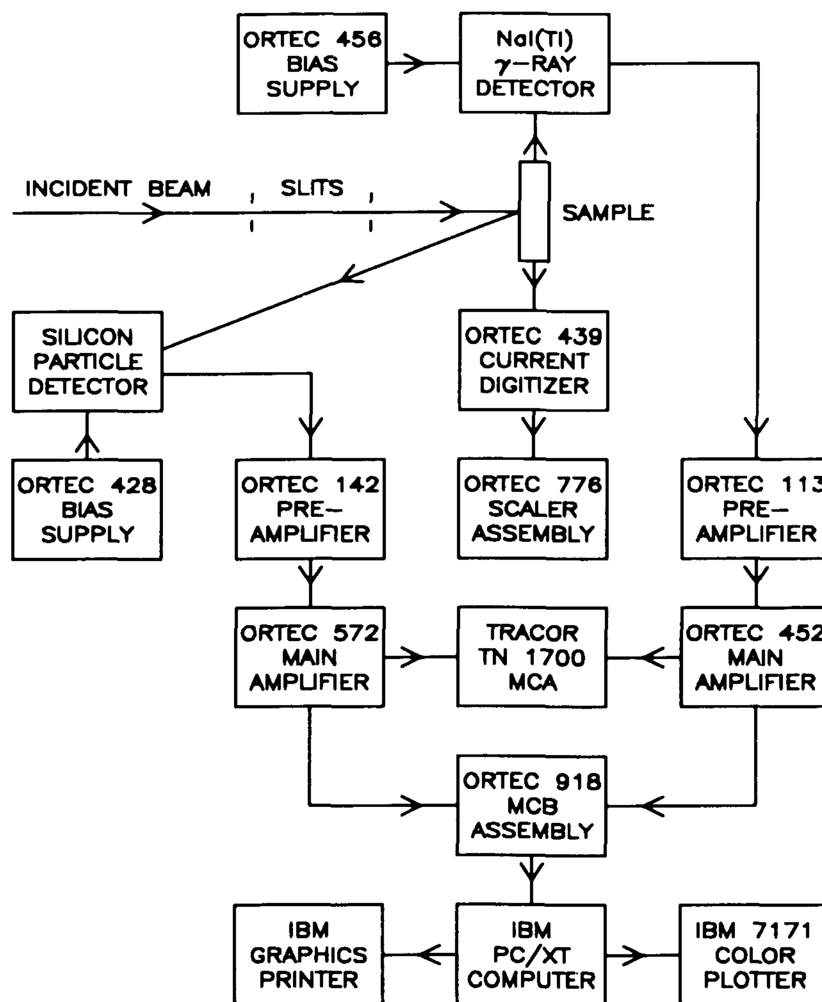

Figure 1.5 Schematic representation of the electronics block diagram.

and retrieval. The data acquisition system included software (modified by the author) for both on-line and off-line analyses of data.

Details of Experiment

For each sample analyzed, the $Al_xGa_{1-x}As$ epilayer thickness was first determined by ion beam methods. This was more reliable than relying on the (nominal) thicknesses given by the sample grower(s). Knowledge of the thickness was required in order to select the best beam energy to use and to determine whether corrections from other resonances of the $^{27}Al(p,\gamma)^{28}Si$ reaction were necessary. For higher values of x (>45%), RBS gave an adequate estimate of the aluminum layer thickness. For lower values of x it was necessary to use the 0.992-MeV $^{27}Al(p,\gamma)$ resonance for depth profiling.[15]. An effort was made to match the AlAs standard layer thickness as closely as possible to the sample being measured, so that corrections from other $^{27}Al(p,\gamma)$ resonances were reduced to a minimum. Two energies were chosen for samples of various thickness such that the 0.992-MeV resonance would be well within the $Al_xGa_{1-x}As$ layer. These two energies probed somewhat different regions of the same piece of material and often required different corrections for smaller resonances, if any. This served as a reliable consistency check as well as a check on the uniformity of the alloy composition throughout the layer.

The actual runs consisted of taking data alternately on the 4 samples mounted on the target holder by remotely rotating the vacuum feed-through. Each sample required 1 to 10 minutes of running time, depending on the amount of aluminum in it. Each time a slightly different target orientation relative to the incident beam was chosen, up to $\pm 10^{\circ}$, to watch for possible remnants of partial channeling effects. A typical RBS spectrum is shown in Fig. 1.6 and a γ-ray spectrum in Fig. 1.7.

For the data analysis, all runs on the target were averaged, and then the corrections from other small $^{27}Al(p,\gamma)$ resonances were applied to the γ-ray yield, if applicable. A double ratio was then formed as discussed earlier. These data, together with incident beam energy, etc., were fed into a BASIC program to calculate the alloy composition. Because of the dependence of stopping power on composition, and then to the slightly different scattering energies E_1 and E_2 (for a fixed window E_1' and E_2' on RBS), the program had to calculate values of E_1 and E_2, and then the projected value of alloy composition, x. The procedure was then repeated (iterated) until a self-consistent solution was obtained. In all cases the correction factor, A, in Eqns. (1.8) and (1.11) was found to be between 0.9976 and 1.0001, indicating that the correction was indeed very small.

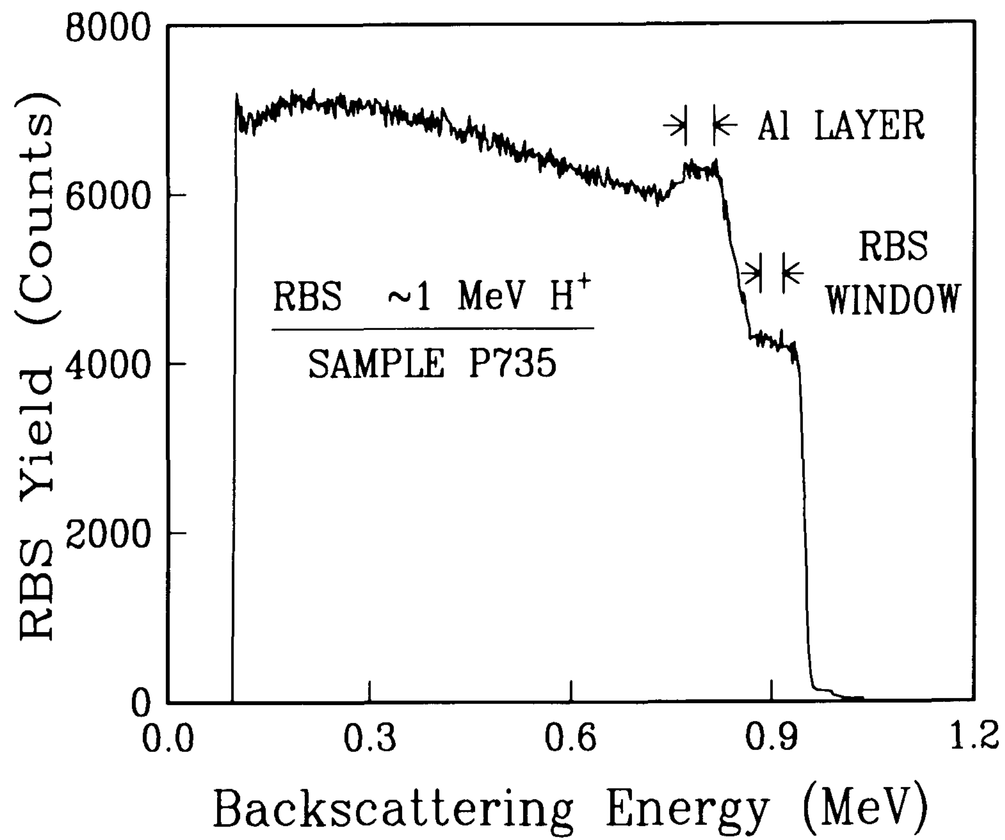

Figure 1.6 RBS spectrum of sample P735 (1.1 μm, x=0.825). The incident beam was ~ 1 MeV H^+. The window for data analysis is shown.

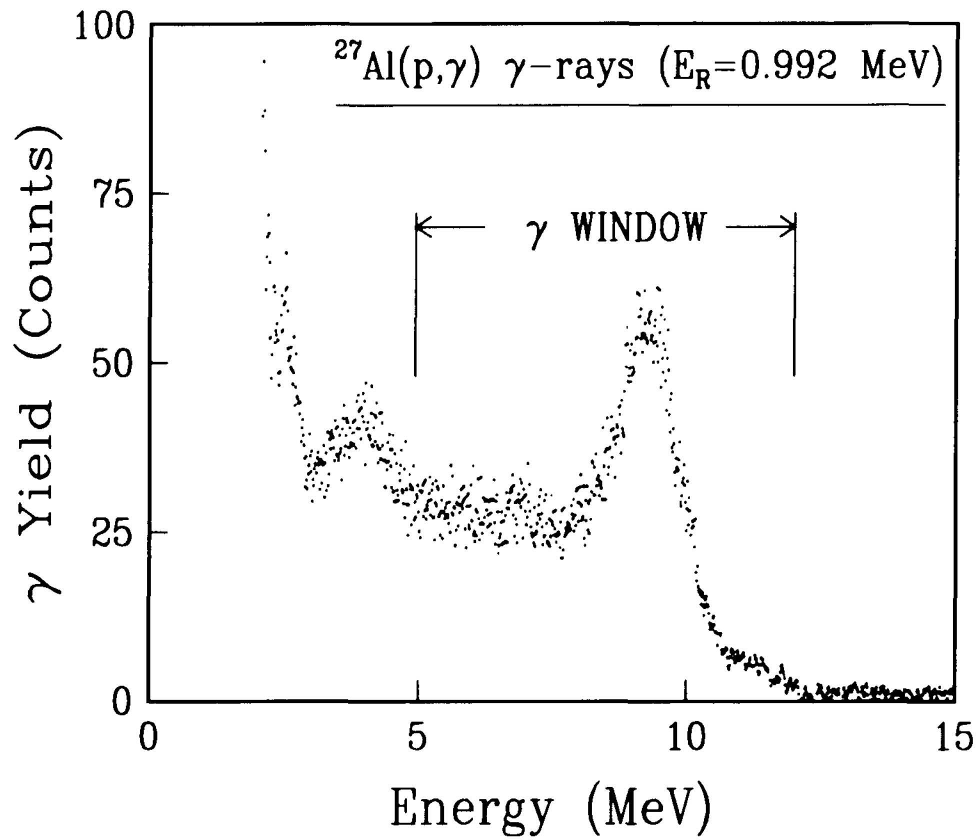

Figure 1.7 Gamma-ray spectrum of the $^{27}Al(p,\gamma)^{28}Si$ reaction at 0.992 MeV on a 2-μm AlAs sample. Incident proton energy is 1.009 MeV. The window for data analysis is shown.

Discussion of Errors and Corrections

Because we were aiming to achieve a 1% determination in the absolute aluminum composition, it was important to consider various factors that might have affected the results of our measurements in a systematic way.

1) Other resonances in the $^{27}Al(p,\gamma)^{28}Si$ reaction

In order to be able to account for other resonances in the $^{27}Al(p,\gamma)^{28}Si$ reaction near 1 MeV, the relative yields of these resonances, namely those at 0.923, 0.937, and 1.025 MeV, were measured on a GaAs sample with a thin layer (about 2000 Å) of aluminum deposited on top of it, under exactly the same geometry. These resonances correspond to different excited states in the final state nucleus ^{28}Si, with different spin-parity assignments. They are likely to follow different decay schemes (branching ratios), leading to different γ-ray spectra. Therefore not only the geometry, but also the γ-ray ROI must be matched in order for the corrections to be meaningful. The relative yields listed in Table 1.1 are for our geometry and γ-ray window for data analysis. Figure 1.8 shows the excitation curve.

Table 1.1 Relative yields of $^{27}Al(p,\gamma)^{28}Si$ resonances near 1 MeV for our geometry.

Resonant energy (MeV)	Relative yield (arbitrary Units)
0.923	7.98 ± 0.13
0.937	11.74 ± 0.16
0.992	100.00 ± 0.53
1.025	12.94 ± 0.12

The correction for other resonances was based on the measured epilayer thickness (as determined by ion beam methods) and the incident beam energy. A very conservative approach was chosen so that, if there was any possibility that a resonance (with enlarged width due to straggling) might fall close to either the front surface or the interface of the $Al_xGa_{1-x}As$ epilayer for a particular data point, that data point was discarded. The estimate on energy straggling of the incident beam at various depths was also very conservative, guaranteeing that remaining data would be free of effects from other resonances.

2) Channeling

Data obtained at the beginning of this study were from high quality single

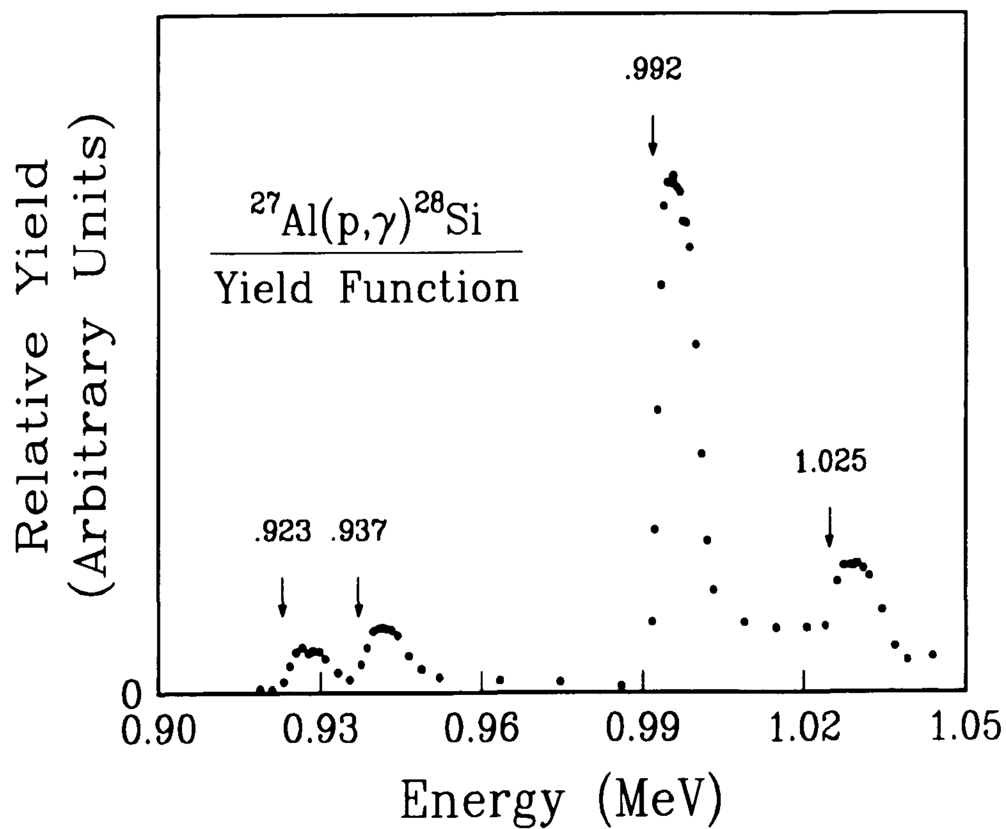

Figure 1.8 Relative yields of the resonances of $^{27}Al(p,\gamma)^{28}Si$ reaction near 1 MeV for our experimental geometry and γ-window.

crystal materials. Channeling of 1-MeV protons on these samples, as seen in the RBS spectra, was very easy to obtain. In fact, it was difficult, if not impossible, to avoid at least partial channeling. The channeling behavior made it difficult to get reliable results from both the RBS and the γ-ray yields. While the biggest channeling dip around the [100] direction could be avoided, partial channeling from other minor axes and planes would introduce errors that would far exceed our desired precision in the absolute x measurement, no matter what the angle of the incident beam happened to be. In fact, 1-MeV protons are so "soft" that they can be easily "steered" into (partial) channeling. We decided to use ion implantation as a means of destroying the sample crystallinity sufficiently so that channeling effects would be reduced to a minimum and a truly "random" RBS could be obtained on these samples. There were two reasons behind this approach. First, a goniometer with precise angular control of the target orientation was not available, so it was not possible to "average" over the minor channeling structures to get a random spectrum, as it is customarily done in many channeling experiments. Second, it was not clear, either theoretically or experimentally, how a resonant nuclear reaction yield would change relative to RBS, under channeling conditions. Channeling is normally interpreted as the effect of rows and columns of a crystal lattice forcing the particles incident near one of the major axes or planes to stay away from them. The channeled

particles see a less crowded electron distribution and consequently experience a smaller energy loss. The change in stopping power implies that the γ-ray and RBS yields will come from different regions of the sample under different channeling conditions. For well-channeled ions, both γ-ray and RBS yields will be reduced because of the smaller probability of close encounters with target nuclei. The current theory of channeling can predict the decrease in RBS yield at a channeling minimum by calculating the fraction of the incident particles that undergo close enough encounters (around 0.1 to 0.2 Å) to result in large-angle scattering. Resonant nuclear reactions on light nuclei normally exhibit a similar impact parameter dependence though it is not identical to that for Rutherford scattering. More importantly, the energy dependence of resonant reactions is very different. Consequently, one cannot safely assume that the γ-ray yield drops by the same percentage as the RBS yield. In fact, it was observed that the ratio of γ-ray to RBS yields fluctuated as a function of incident angle, up to about 10% (Fig. 1.9). It was concluded that the safest way to deal with this problem was to eliminate the channeling altogether, by amorphizing the sample using ion implantation. The implantation dosage was high enough to introduce damage to the sample's crystalline structure, but not enough to cause compositional change or alloy re-distribution that would affect the reliability of ion beam measurements. It was estimated that the maximum temperature

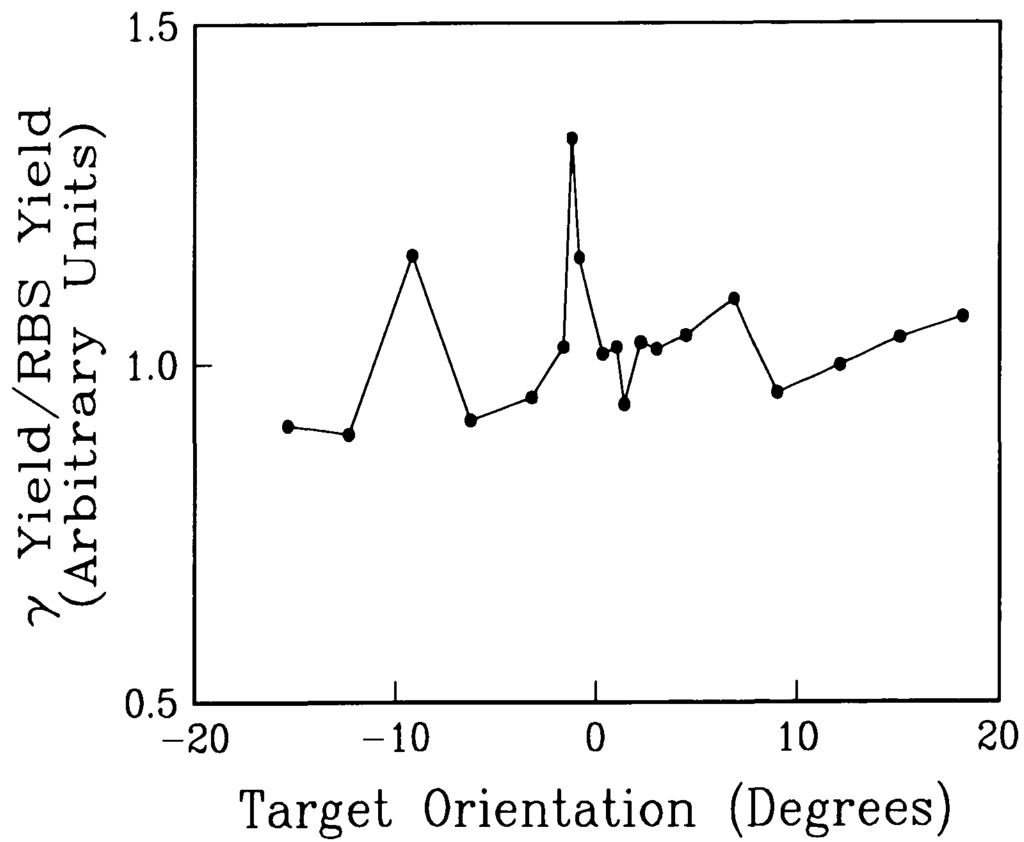

Figure 1.9 Ratio of γ-ray yield to RBS yield as a function of the incident angle (relative to target crystal axis).

increase of the sample during ion implantation (see Appendix) was about 100 °C. This temperature is well below the temperature (~ 800 °C) at which significant atomic mobility occurs in $Al_xGa_{1-x}As$. Depth profiles of the samples subsequent to ion implantation also showed that the $Al_xGa_{1-x}As$ layer were in excellent agreement with what was expected from growth conditions.
Samples after ion implantation showed very little or no channeling behavior. However, the remnant fluctuation of the single ratio (about 5% in the worst case) still constitute the major contribution to the final error bars.

3) Straggling

As mentioned earlier, the incident beam energies chosen for composition measurement were selected so as to avoid any possibility of the resonances extending beyond the sample epilayer, after taking into account the straggling-induced broadening effects. Straggling is therefore not an important factor.

4) Contribution to γ-ray yield from $^{15}N(p,\gamma)$ and $^{19}F(p,\alpha\gamma)$ resonances

The two isotopes, ^{15}N and ^{19}F, are well known to have large cross sections for (p,γ) and (p,αγ) resonances. The $^{15}N(p,\gamma)$ resonances are all far

away from ~ 1 MeV and the corresponding γ-ray energies are also too low (about 4 MeV, outside our γ-ray energy window) to have any significant effects on our measurements. However, we did observe the γ-rays of $^{15}N(p,\gamma)$ from the SiN_2 layer of AlAs samples by tuning the accelerator to the appropriate energies. The $^{19}F(p,\alpha\gamma)$ reaction has many strong resonances with dominant γ rays at about 6 to 7 MeV. It was for this reason that 2 ROIs on the γ-ray detector were used. The second ROI, used mainly for cross checking purposes, covered only the ~ 10 MeV peak where no F(p,αγ) γ-ray is present. Normally, when no other reactions are also producing γ-rays of comparable or higher energies, the γ ROI can be made very wide to improve counting statistics, for a large number of high energy γ rays do not deposit their full energy into the detector, resulting in lower energies in the spectrum (the Compton tails). With a multi-line spectrum, when statistics are not good enough to facilitate peak deconvolution, the safest procedure is to restrict the ROI to the full energy peak only, at the expense of lower counting efficiency. In our case, all data analyses were done on both windows. After corrections for other Al(p,γ) resonances, which were also window-dependent, the results from the two windows agreed extremely well for all samples, indicating that there was no contribution from ^{19}F.

Results and Summary

The $Al_xGa_{1-x}As/GaAs$ samples analyzed using a combination of RNRA and RBS are listed in Table 1.2 in ascending order of the measured alloy composition, x. Reference numbers are those used by the sample growers and the thicknesses are those from ion beam analysis. The EM results were obtained at IBM's Thomas J. Watson Research Center prior to nuclear determination and are also listed for comparison.

Except for one or two samples, the ion beam results agreed very well with the EM results within the experimental errors. Since the low temperature PL measurements had already been performed on these same samples, their fundamental band gaps were also known to within a few meV (after correction for exciton binding energy). From these data the relation between $Al_xGa_{1-x}As$ band gap, E_g, and the alloy composition, x, can be determined absolutely. The relation obtained this way is:

$$E_g(Al_xGa_{1-x}As) = 1.512 + 1.455x \ (eV), \quad T=2K, \ 0<x<0.4 \tag{1.13}$$

Figure 1.10 shows the least-square fit of the above equation to data points.

Table 1.2 Summary of absolute x measurements.

Sample Ref. #	Al layer Thickness (μm)	Alloy composition at 1.009 MeV		Alloy composition at 1.053 MeV		E.M. results[+]	
0529	3.2	0.111	±0.005	0.111	±0.056	0.111	±0.056
P934	2.6	0.203	±0.009	0.209	±0.006*	0.192	±0.010
120485	1.8	0.242	±0.014	0.235	±0.009	0.252	±0.013
0531	2.8	0.271	±0.012	0.265	±0.008	0.279	±0.014
011685-1	0.9	0.336	±0.013	-		0.327	±0.016
0604	3.1	0.421	±0.015	-		0.428	±0.021
012385-2	1.9	0.446	±0.014	0.461	±0.015	0.403	±0.020
P726	2.4	0.460	±0.024	0.459	±0.013*	0.437	±0.022
P860	2.3	0.580	±0.019	0.571	±0.010*	0.56	±0.028
P856	2.1	0.696	±0.014	0.692	±0.034*	-	
P731	1.3	0.758	±0.017	-		0.69	±0.034
P735	1.1	0.825	±0.019	-		0.79	±0.039

+ Electron microprobe measurements performed at analytical services laboratory, IBM Thomas J. Watson research center.

* At 1.040 MeV.

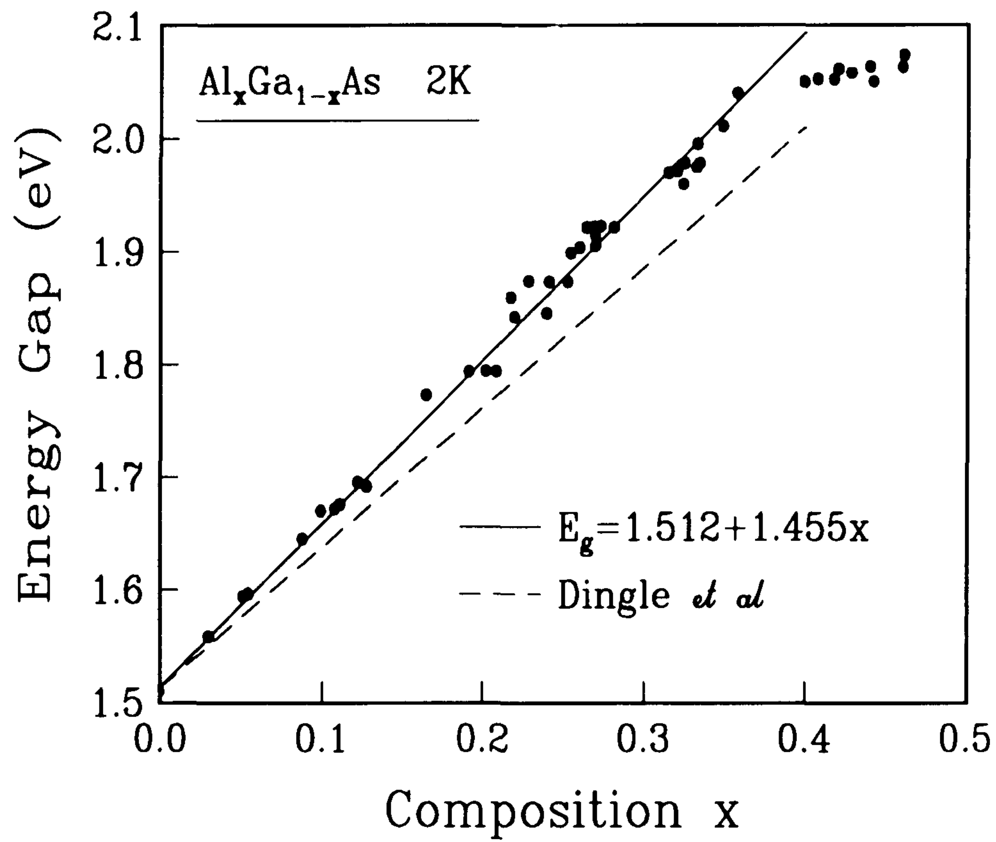

Figure 1.10 Band-gap of $Al_xGa_{1-x}As$ as a function of alloy composition, x. The solid line is a fit to Eqn. (1.13). The dashed line is from Ref. 13.

The slope, $\Delta E_g/\Delta x$, in Eqn. (1.13) should be very close to the value at room temperature, so,

$$E_g(Al_xGa_{1-x}As) = 1.424 + 1.455x \ (eV), \quad T=300K, 0<x<0.4 \qquad (1.14)$$

Other groups have reported values of $\Delta E_g/\Delta x$ ranging from 1.25[14] to 1.61.[10]

The direct (Γ) to indirect (X) band gap transition was also studied by low temperature PL. Based on the ion beam determination of x, the composition at which this transition occurs is,

$$x_{\Gamma-X} = 0.37\pm0.015, \quad T=2K \qquad (1.15)$$

This value is somewhat lower than previously reported for liquid helium temperatures.

Equations (1.14) and (1.15) have become the most widely accepted relations, following publication of our results.[17,18]

Huang *et al*[23] used resonant nuclear reaction analysis in conjunction with room temperature photoreflectance (PR) to obtain the band gap - alloy

composition relation of the $Al_xGa_{1-x}As$ material system. Their results, in the form of a second-degree polynomial for $0<x<0.45$, agreed very well with Eqn. (1.13) (to within 4 meV, or less than 1% in the slope $\Delta E_g/\Delta x$).

Further study in this direction may include the employment of this technique to calibrate the band gap versus alloy composition relations of other important semiconductor materials, such as $Al_xGa_{1-x}Sb$, and $Al_xIn_{1-x}As$.

Chapter Two

Ion Beam Analysis of Lithium in amorphous MoS_3

Introduction

Secondary lithium cells can be used as high energy power sources for applications ranging from automobile propulsion to semiconductor memory maintenance. Among the emerging materials for secondary lithium cell applications, amorphous molybdenum trisulfide (a-MoS_3) is one candidate which offers perhaps the best possibilities. Amorphous MoS_3 is an unusual material which, along with $MoSe_3$, WS_3, and WSe_3, can be prepared only in the amorphous form. Amorphous MoS_3 powder prepared by thermal decomposition (TD) of ammonium tetrathiomolybdate (ATTM) has shown charge-discharge cycling lifetimes of up to 52 cycles for large 20 A-h cells, utilizing 2 to 2.5 Li per molecule of MoS_3 for each cycle.[24] Amorphous MoS_3 prepared by a precipitation technique was found to charge-discharge 3 Li per MoS_3 reversibly.[25] In all of these charge-discharge cycling measurements, a-MoS_3 powder along with binder has been used as the active cathode. No information about the discharging behavior of pure a-MoS_3 is available in the literature.

Recently, the electro-deposition (ED) method was used for depositing thin films of a-MoS_3 from both non-aqueous (NA) and aqueous (A) solutions of ATTM.[26,27] Using these ED a-MoS_3 thin films it was possible to charge-discharge pure a-MoS_3. The major advantage of charging-discharging a thin film lies in the time scale: several hours as apposed to several weeks for a-MoS_3 pellets.

Several techniques are available for the characterization of lithium-intercalated MoS_3 samples. Neutron diffraction and infrared absorption (reflection) are among the most widely used ones.[28] Raman scattering and electrolyte electroreflectance have also been used.[29] These techniques do not provide a direct measure of the absolute amount of lithium and its depth distribution inside the MoS_3 sample. Instead, the "standard" method is to calculate the amount of lithium from the total charge during a charge-discharge cycle, assuming, of course, that all lithium ions go into the sample and are uniformly distributed. This assumption is much too simplified. One does not have an independent verification of its validity, nor does one have any measure of the accuracy of lithium concentration obtained in this way. Other secondary techniques, such as Raman scattering, can be used for composition measurements. Depth profiling using Raman scattering can be accomplished by

using various lines of the pumping laser. However, the compositional dependence of Raman peaks, or phonon frequencies, needs to be first established beforehand by some primary means. It is, therefore, important to look for a primary technique for the lithium concentration measurement independently to verify as well as calibrate the secondary techniques.

Nuclear techniques, such as Rutherford backscattering and nuclear reaction analysis, are quantitative and primary in their nature. As discussed in chapter one, NRA, together with RBS, can be used to depth-profile the alloy composition in semiconductor materials, for example the aluminum concentration in epitaxially-grown $Al_xGa_{1-x}As$[15,16], and to determine the composition, x, absolutely.[17,18] In this chapter, a similar technique is applied to the determination of lithium concentration in a-MoS_3Li_x.[27] Comparisons will then be made of cells prepared by different means (ED and TD) and under different charging conditions.

The $^{7}Li(p,\gamma)^{8}Be$ reaction at 0.441 MeV

Among the resonances of the $^{7}Li(p,\gamma)^{8}Be$ reaction within the accessible range of the Dynamitron accelerator (0.2 to 3.7 MeV), the 0.441-MeV resonance is the best for depth profiling purposes. It has a natural width of about 12 keV, the narrowest of all (although not as narrow as the $^{27}Al(p,\gamma)^{28}Si$ resonances). The γ-rays emitted from this reaction have characteristic energies around 13 MeV, well above any significant background region. These features are very similar to the $^{27}Al(p,\gamma)^{28}Si$ resonance used in the alloy composition determination of $Al_xGa_{1-x}As$. This incident proton energy, however, is somewhat too low for the accelerator's beam transport system to function efficiently. For this reason a molecular beam of H_2^+ at twice the energy was used instead. The molecular H_2^+ beam, upon entering the target, will be stripped of its only electron within a few monolayers; the remaining two protons are then separated by the repulsive Coulomb force between them, a process termed Coulomb Explosion. Thus, for our purposes, the molecular H_2^+ beam is equivalent to a proton beam with half the energy.

The separation energy between two protons in an H_2^+ molecule, e^2/r, where

r is the average distance between two protons, is of order 10 eV in the rest frame of the beam. It is magnified when transformed to the laboratory reference frame by a factor of about 10^3. This energy spread then becomes part of the total energy broadening. It has to be considered together with the resonance width and accelerator energy resolution (about 2 keV). It was estimated that the resonance width was much larger than the other terms and the total resolution was dominated by the resonance width.

RBS Cross Section

The Rutherford cross section is given by[21]

$$d\sigma_{cm,Rutherford} = \left[\frac{e^2 Z_1 Z_2}{E}\right]^2 \sin^{-4}\frac{\theta}{2} \tag{2.1}$$

where Z_1 and Z_2 are the atomic numbers of projectile and target, respectively, E is the incident projectile energy, and θ is the scattering angle relative to incident beam direction. In the laboratory frame it can be re-written in practical units as[30],

$$d\sigma_{lab,Rutherford} = 1.236\left[\frac{Z_1 Z_2}{E}\right]^2 \left(\sin^{-4}\frac{\theta}{2} - \frac{1}{2}\left(\frac{M_1}{M_2}\right)^2 \ldots\right), \ msb \tag{2.2}$$

where E is in units of keV. The expansion converges quickly for $M_1 < M_2$, i.e., for a light projectile incident on a heavy target.

The energy of the scattered projectile, E_0' is related to the energy before scattering, E_0, and the kinematic factor, K, by[21],

$$E_0' = KE_0 \tag{2.3}$$

where

$$K = \left[\frac{\cos\theta + \left(\rho^2 - \sin^2\theta\right)^{1/2}}{1 + \rho^2} \right]^2 \tag{2.4}$$

and $\rho = M_1/M_2$ is the mass ratio.

The energy of a backscattered proton from a depth z inside the target also depends on the stopping power of the target material, namely,

$$E' = K\left[E_0 - \Delta E_{in}(z)\right] - \Delta E_{out}(z) \tag{2.5}$$

where $\Delta E_{in}(z)$ and $\Delta E_{out}(z)$ represent energy losses of the particle as it goes in and out of the target.

Assuming that the stopping power changes slowly with energy, which is usually the case, the RBS spectrum of a single thin layer of target consisting of only one element will be in the form of a "bump." The highest energy of the bump corresponds to surface scattering, whose position in the spectrum is determined by the kinematic factor for that element times the incident beam

energy.[21] For an infinitely thick sample (from the point of view of the ion beam), the bump extends to zero energy. If the target consists of more than one element, there will be multiple bumps, or edges, that are characteristic of the masses of individual elements. The relative height of each edge is determined by their Rutherford cross sections and sample composition. Figure 2.1 shows some simulated RBS spectra of thin, thick single elemental layers and composite targets. The simulation was performed using RUMP, an RBS analysis program developed by L. Doolittle of Cornell University[31].

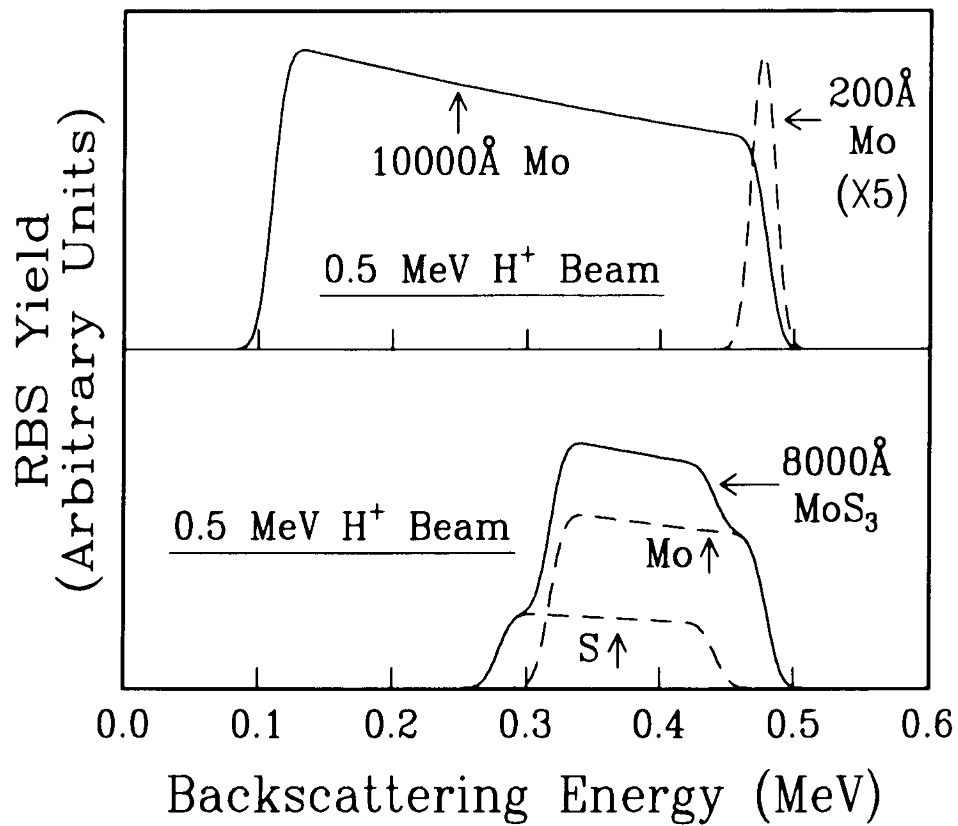

Figure 2.1 Simulation of RBS spectra of 0.5 MeV H^+ on thin (200Å Mo), thick (1μm Mo) single elemental (top) and compound (8000Å MoS_3) (bottom) targets.

Lithium Determination

The amount of lithium can be determined by normalizing the γ-ray yield of the $^7Li(p,\gamma)^8Be$ reaction from an a-MoS_3 sample to a suitable standard (some known compound containing lithium), analogous to the procedure used in chapter one.

To measure the lithium concentration at a depth z, the beam energy, E_0, is selected such that the mean energy of the beam is at the resonance energy, E_R (0.441 MeV), at depth z. In other words, E_0 is obtained by solving the equation,

$$E_R = E_0 - \int_0^z \left[\frac{dE}{dz}\right] dz \tag{2.6}$$

Because the stopping power is really a function of energy, rather than depth, the above expression cannot be readily evaluated. Instead, one has to integrate the reciprocal stopping power to find the depth z,

$$z = \int_{E_0}^{E_R} \left[-\frac{dE}{dz}\right]^{-1} dE \tag{2.7}$$

If the stopping power (to be precise, the stopping power per atom or molecule,

or the stopping cross sections) at the neighborhood of the resonant energy is denoted by ε, then the γ-ray yield is, according to chapter one, Eqn. (1.3), and making use of the additivity law,

$$Y_\gamma\ (MoS_3Li_x) \propto \frac{x}{\varepsilon(MoS_3)\ +\ x\varepsilon(Li)} \tag{2.8}$$

where x is the lithium concentration per MoS_3 at depth z, averaged over the combined width of the incident beam and energy straggling.

For a standard such as LiF or LiCl,

$$Y_\gamma(LiF\, or\, LiCl) \propto \frac{1}{\varepsilon(F\, or\, Cl)\ +\ \varepsilon(Li)} \tag{2.9}$$

The ratio, R, of the γ-ray yields from the sample relative to a standard is then,

$$R \equiv \frac{Y_\gamma(MoS_3Li_x)}{Y_\gamma(LiF\, or\, LiCl)} = x\ \frac{\varepsilon(F\, or\, Cl)\ +\ \varepsilon(Li)}{\varepsilon(MoS_3)\ +\ x\varepsilon(Li)} \tag{2.10}$$

or,

$$x = \frac{R\varepsilon(MoS_3)}{\varepsilon(F\, or\, Cl)\ +\ (1-R)\varepsilon(Li)} \tag{2.11}$$

A similar but more detailed derivation is given in chapter one for the case

of aluminum in $Al_xGa_{1-x}As$ and will not be repeated here.

The result, Eqn. (2.11), is independent of the density of the MoS_3 or any standard, a direct consequence of the "per atom" feature of the stopping power and the fact that we calculate lithium "per MoS_3." It should also be noted that, because of the lack of a standard sample of closely matched chemical composition (such as in the case of AlAs to $Al_xGa_{1-x}As$), the stopping powers themselves enter in the expression. Here there is no near-perfect cancellation of almost all corrections, even when a double ratio is formed. In addition, for most of the lithium compounds it is not safe to assume that the scattering cross sections are pure Rutherford. Nevertheless, the formation of the ratio R still eliminates a number of factors, such as geometry, that would otherwise significantly affect the measured quantity.

Depth Profiling

To obtain a depth profile of the lithium in an a-MoS_3 cell, one needs to measure the γ-ray intensity as a function of beam energy, starting at or slightly below the resonance energy and going up in energy. When the beam energy is at the resonance, γ-rays from the $^7Li(p,\gamma)^8Be$ reaction are coming from the surface of the target, where the resonance occurs. At higher energies, there will be no γ-rays from the surface, but rather from a layer deeper into the sample where the mean energy of the beam has been brought back down to the resonance energy by the stopping power of the target. Thus, a scan of γ-ray yield versus incident energy is really a scan of lithium concentration versus depth. The energy scale is related to the depth scale by an integration of the reciprocal of the stopping power of a-MoS_3Li_x,

$$z = \int_{E_0}^{E_R} \left[-\frac{dE}{dz} \right]_{MoS_3Li_x}^{-1} dE \tag{2.12}$$

The natural unit of depth in the above equation is atoms/cm^2, or "depth*density." To convert to conventional depth units, such as μm, one needs

to assume that the density of MoS_3Li_x does not depend on x or has some known dependence. Figure 2.2 is a plot of the stopping power of MoS_3Li_x, for various values of x[22], assuming a constant density of MoS_3 independent of x. Figure 2.3 shows the depth versus energy relation for protons in MoS_3Li_x as obtained from Eqn. (2.12).

The depth resolution at the surface is simply that of the incident beam width, including the natural width of the resonance and instrumental width. At a depth z, energy straggling also contributes to the final depth resolution. Straggling results from statistical fluctuations in the process of collisions between beam particles and the target electron cloud as the beam penetrates into the sample. It is generally considered that the beam energy distribution is a Gaussian with a straggling width proportional to the square root of the depth[21], or,

$$\Omega^2_{straggling} = kz \tag{2.13}$$

where k, an energy dependent parameter, varies from theory to theory.

Tabulated values of straggling parameters are not as reliable as those of stopping powers, so one often has to measure it oneself. The theory of

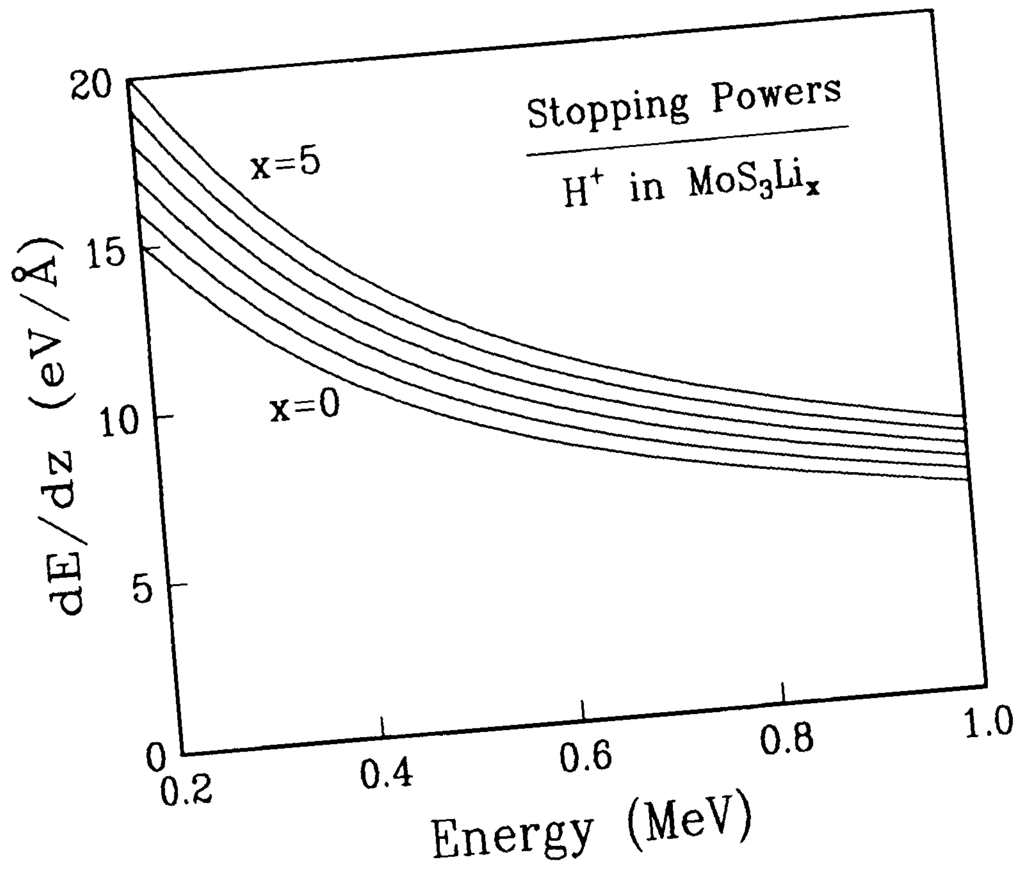

Figure 2.2 Stopping power of H^+ in MoS_3Li_x (x=0,1,2,3,4, and 5), assuming a constant density of MoS_3. From Ref. 22.

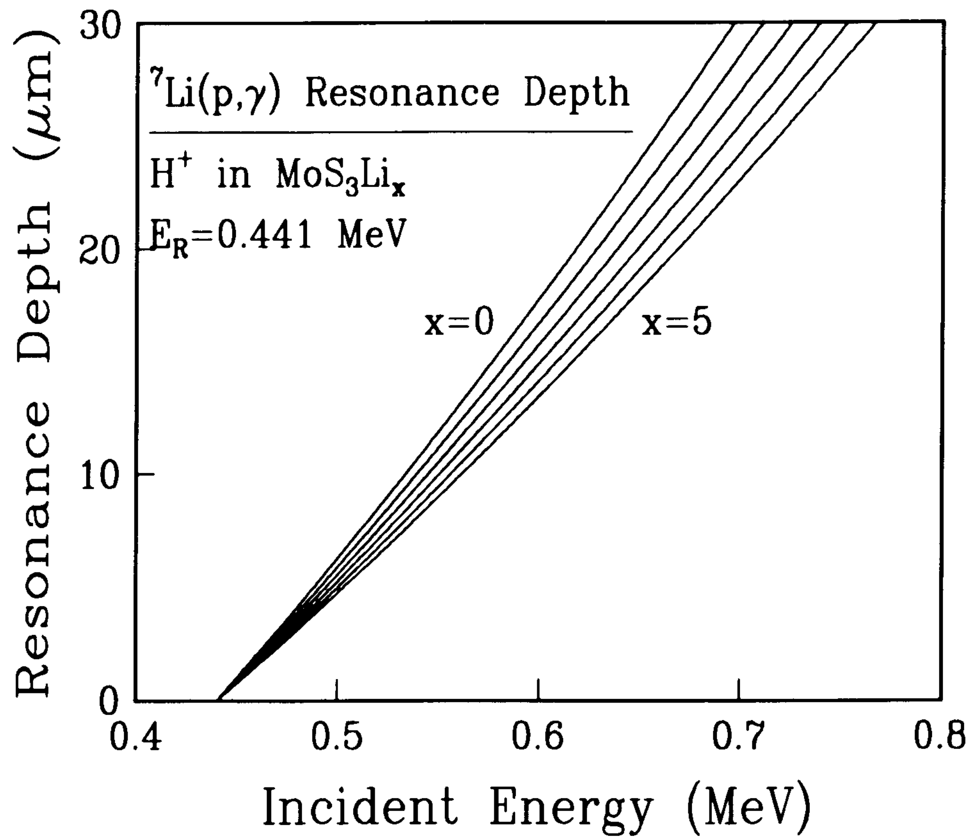

Figure 2.3 Reaction depth of the 0.441-MeV resonance of $^{7}Li(p,\gamma)^{8}Be$ in MoS_3Li_x as a function of incident beam energy (x=0,1,2,3,4, and 5).

straggling for a compound and the relation to its compositional elements is not very well established.[20,21]

Experiment Details

1) Details of Electrochemical Analysis

Samples for this study were ED a-MoS_3 films from both non-aqueous and aqueous solutions of ATTM on nickel and indium-tin-oxide (ITO) substrates (hereby referred to as ED-MoS_3(NA)/ITO, etc.) and under different charging conditions. Typical film thickness was of the order of a few microns. For comparison purposes, conventional TD powder-pellets of a-MoS_3 samples were also prepared. The TD samples were typically 100 μm thick.

The secondary lithium cells consisted of an a-MoS_3 working electrode (active cathode), lithium metal as the reference electrode and also lithium metal as the counter electrode (anode) in an electrolyte solution of 2 M lithium perchlorate dissolved in propylene carbonate solvent. The electrolyte was purged by argon gas continuously during the lithium insertion process. The samples of a-MoS_3 after discharging (insertion of lithium) were rinsed with propylene carbonate solvent to remove any absorbed lithium perchlorate from the surface and were stored in an argon environment before mounting onto the

target holder in the accelerator scattering chamber. A typical lithium insertion curve of an ED-MoS_3 thin film at 100 $\mu A/cm^2$ constant current density in shown in Fig. 2.4. The lithium concentration in the a-MoS_3 sample was calculated from the total accumulation of charge generated by the lithium insertion reaction.

2) Details of Ion Beam Analysis

Every effort was made to shorten the sample transfer process from the electrolyte solution to the ion beam analysis chamber (normally 10 to 15 minutes or less) to avoid any excess exposure of the sample to air. The ion beam measurement apparatus was very much the same as the one described in chapter one. Briefly, the sample holder typically held two a-MoS_3 samples and two standards, LiF and LiCl pellets made from high purity powders. Two silicon surface barrier detectors at 172.5° each detected the RBS particles, and a 3×3 in. NaI(Tl) detector was used for the γ-ray detection. The γ-ray energy window (ROI) covered a region from 9 to 21 MeV. A narrower ROI was not used because there are no other reactions capable of producing γ-rays of this energy. A representative γ-ray spectrum from the $^7Li(p,\gamma)$ reaction is shown in Fig. 2.5. A standard reference[20] lists three $^7Li(p,\gamma)^8Be$ resonances at energies of 0.441,

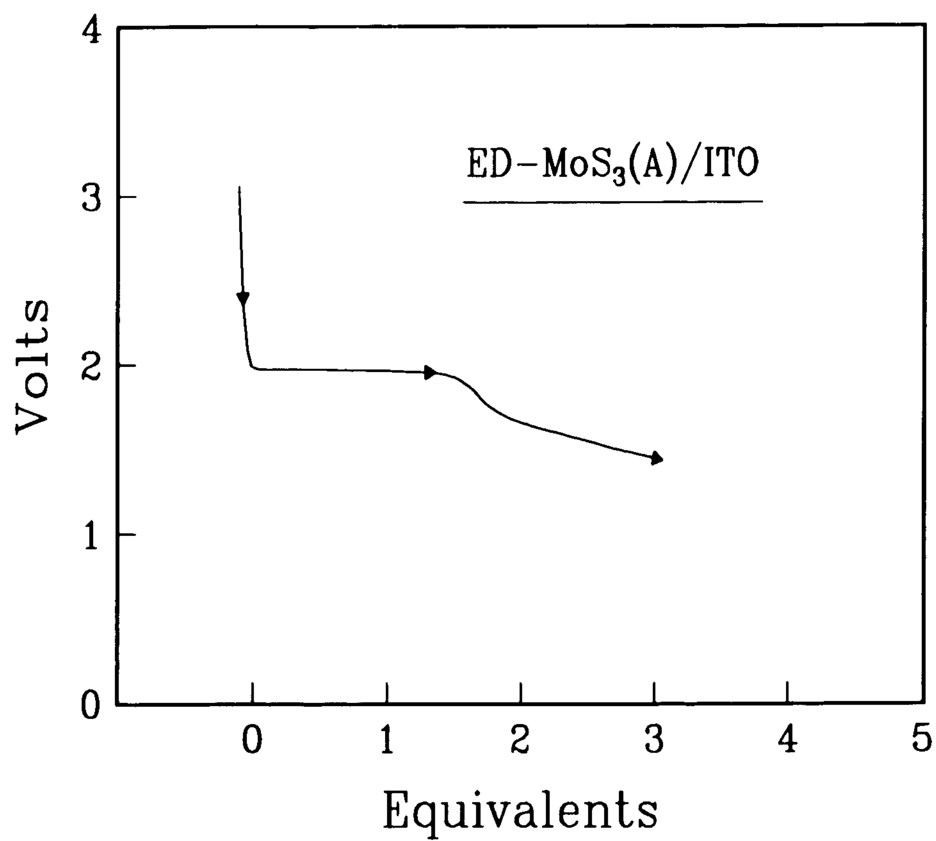

Figure 2.4 A typical lithium insertion (discharge) curve of an electro-deposited a-MoS_3 thin film at 100 μA/cm^2 constant current density.

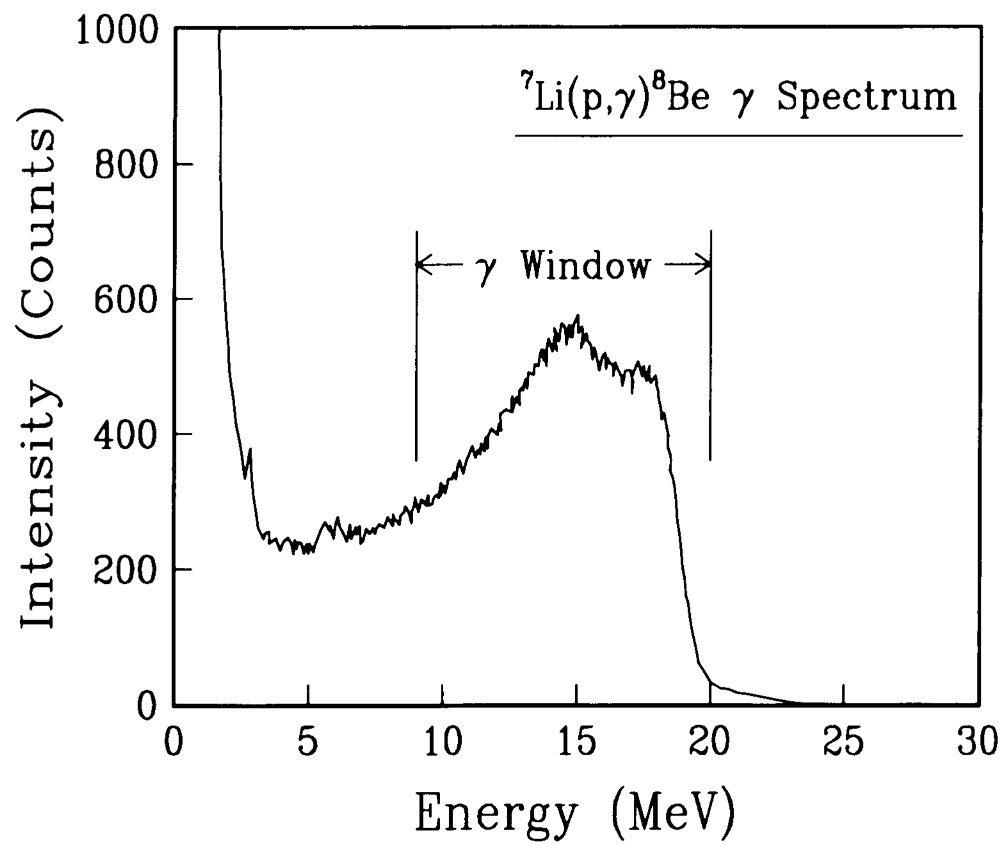

Figure 2.5 A typical γ-ray spectrum from the $^{7}Li(p,\gamma)^{8}Be$ reaction at the 0.441-MeV resonance.

1.030 and 2.100 MeV. No attempt was made to measure the yield function, but it was verified that the width of the 0.441-MeV resonance was in reasonable agreement with the width quoted in reference 20, and that no resonances were found between 0.44 and 1.0 MeV which could affect our measurements.

For depth profiling, the energy of the accelerator was tuned by adjusting the field of the energy-analyzing magnet, controlled and monitored by a nuclear magnetic resonance (NMR) Gaussmeter. Every point on the depth scan was accumulated for a fixed amount of charge (integrated beam current). The depth scale on these points was calculated from beam energy by Eqn. (2.12) and Fig. 2.3. The relation between NMR Gaussmeter and the accelerator energy is:

$$NMR(Gauss) = \frac{C}{Q}\left[E*(E+D*M)\right]^{1/2} \qquad (2.14)$$

where C=80.408647, D=1863.0032, E is the energy in MeV, Q is the charge of the ion in units of free electron charge, and M is the mass of the ion in atomic units. Figure 2.6 is the plot of Eqn. (2.14) for H_2^+.

For the absolute lithium determination, the energy of the H^+ beam was set at the peak of the depth profile, and γ-ray spectra were taken alternately on the sample and LiF/LiCl standards until reasonable counting statistics were

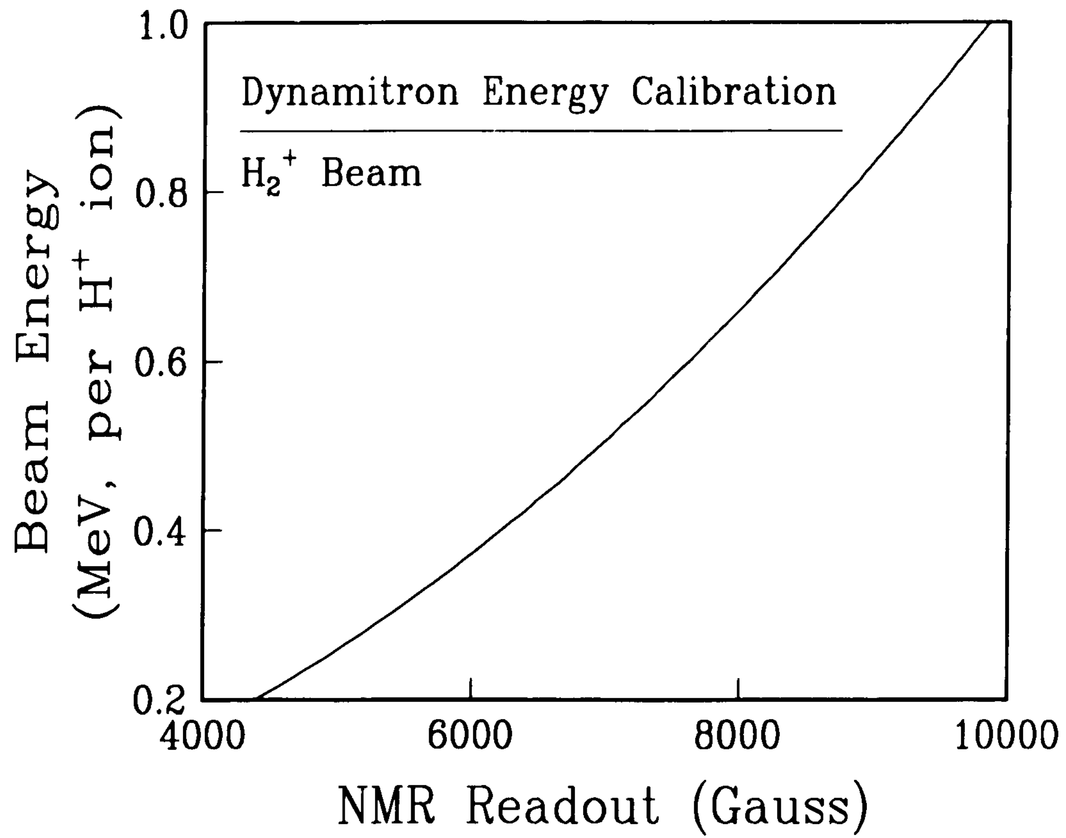

Figure 2.6 The Dynamitron accelerator energy calibration curve for H_2^+.

achieved. The lithium concentration was then calculated by Eqn. (2.11) against both LiF and LiCl standards. Results obtained from LiF and LiCl standards were in excellent agreement.

3) Identification of Features in the RBS Spectra

The RBS spectra of ED-MoS_3(NA)/Ni, ED-MoS_3(A)/ITO and TD-MoS_3 are shown in Figs. 2.7, 2.8, and 2.9 as examples. Other RBS spectra were very similar. The spectra for LiF and LiCl standards are shown in Figs. 2.10 and 2.11.

In the ED-MoS_3(NA)/Ni RBS spectrum, 3 edges were clearly visible. They correspond to the backscattering from Mo, S and substrate Ni, respectively. The RBS spectrum from an ITO sample looks a little more complicated because the glass backing also shows up. On the other hand, the infinitely-thick TD-MoS_3 sample shows nothing more than two edges that correspond to the backscattering from Mo and S, as expected. The RBS spectra of LiF and LiCl standards show signals from F and Cl only. In all cases, because the cross section is so small, RBS was not sensitive enough to detect the light element lithium in the presence of other heavier elements, even when the amount of

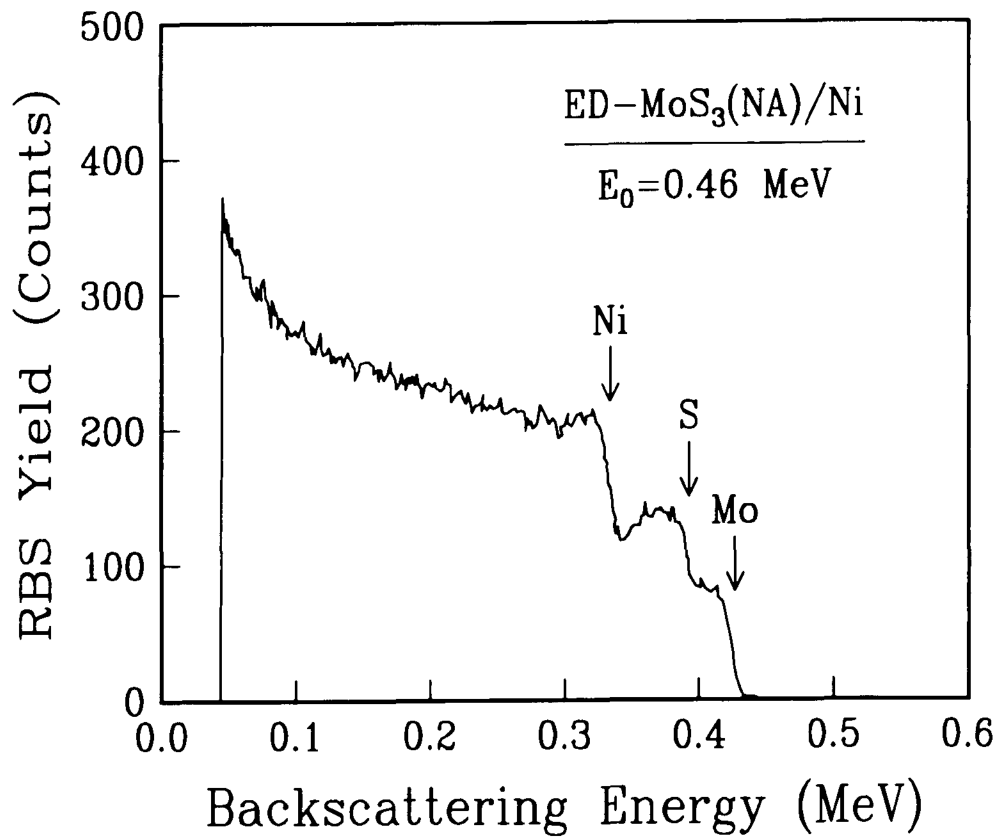

Figure 2.7 RBS spectrum of an electro-deposited a-MoS_3Li_x(NA) thin film sample on nickel substrate.

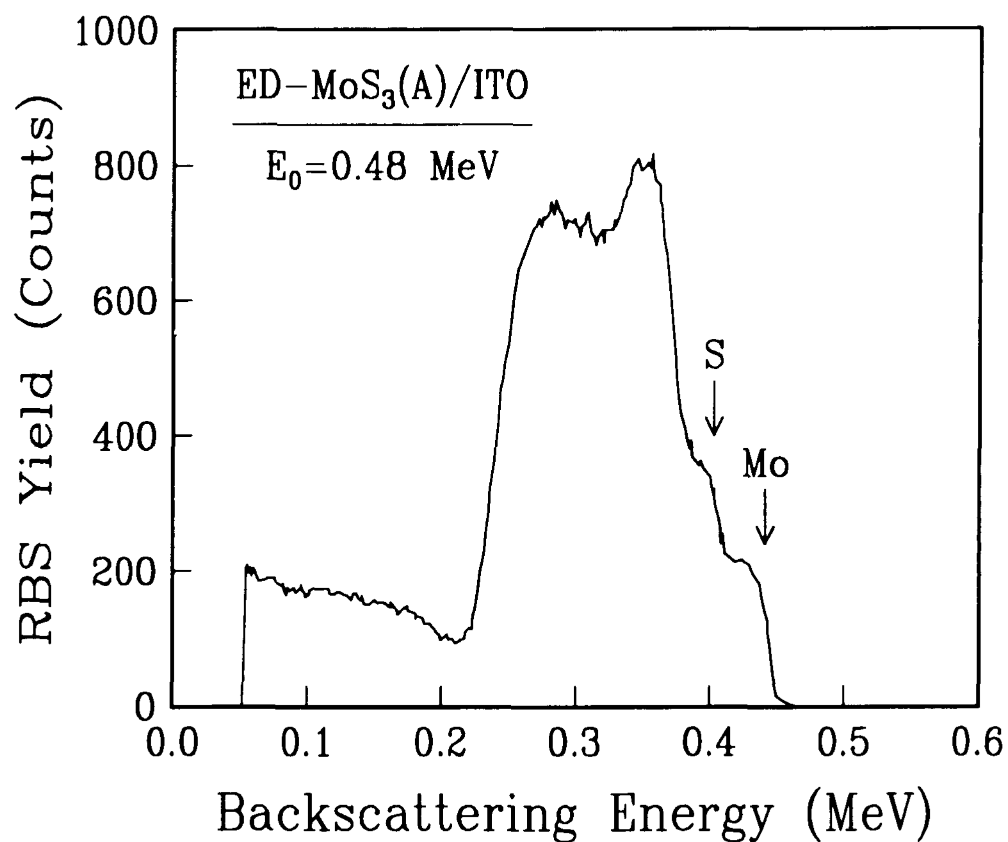

Figure 2.8 RBS spectrum of an electro-deposited a-MoS_3Li_x(A) thin film sample on thin ITO film on glass substrate.

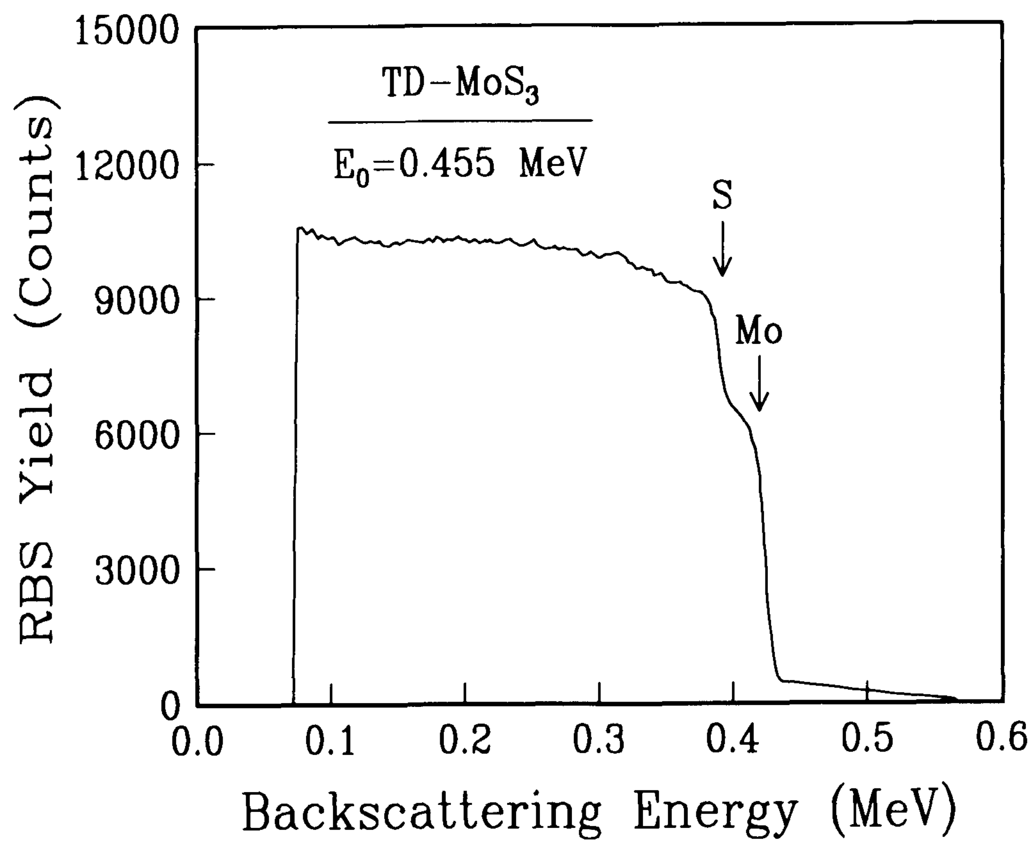

Figure 2.9 RBS spectrum of a thick TD-MoS_3 pellet sample.

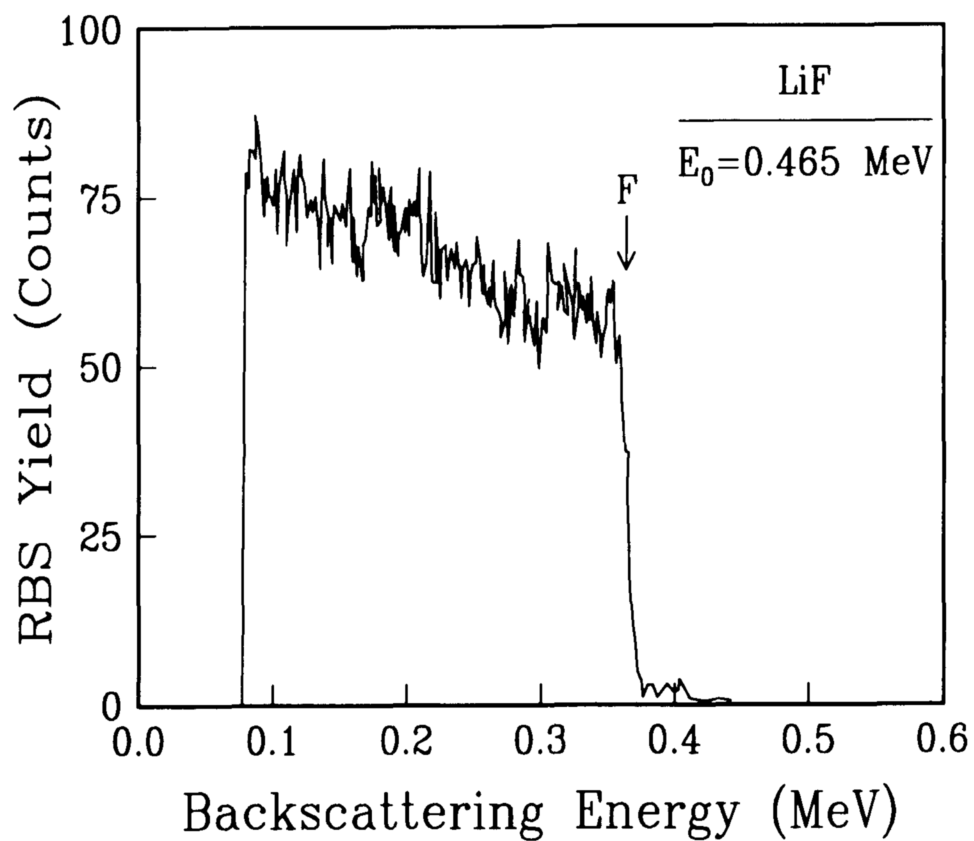

Figure 2.10 RBS spectrum of a thick LiF pellet sample. No lithium is detected by RBS.

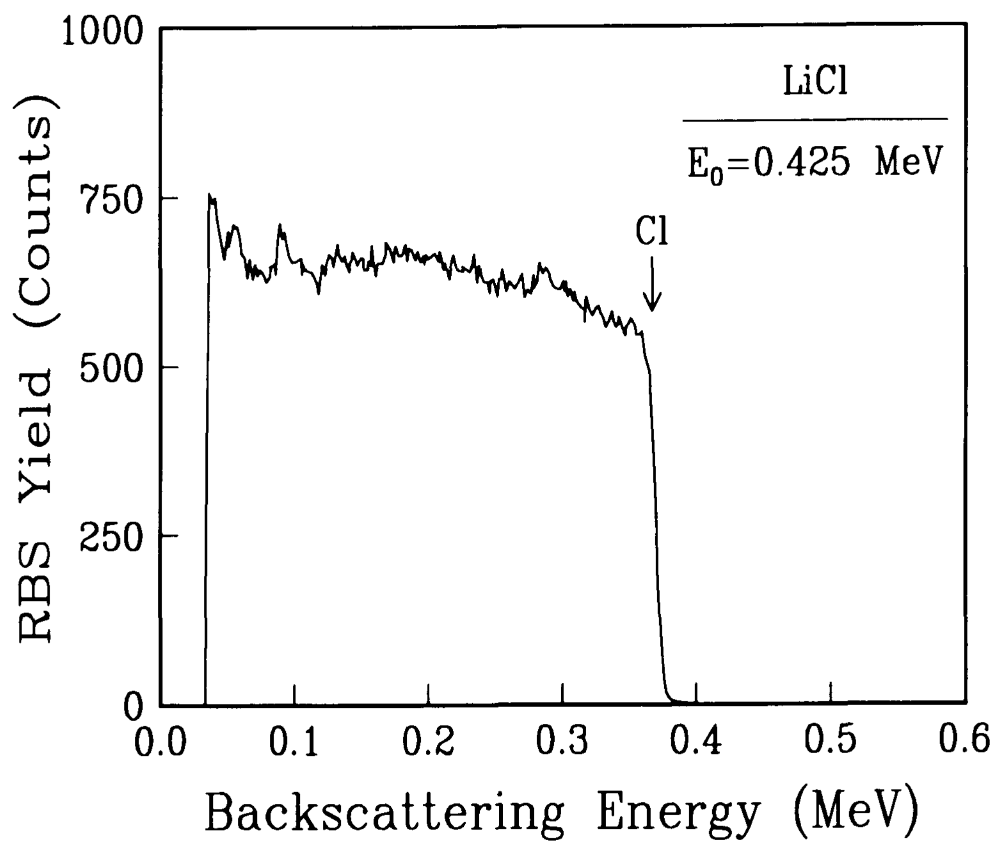

Figure 2.11 RBS spectrum of a thick LiCl pellet sample. No lithium is detected by RBS.

lithium in these samples was very large.

Discussion and Summary

The analyzed data, plotted as number of lithium atoms per a-MoS_3 molecule, as a function of depth, are shown in Figs. 2.12 to 2.14 for ED-MoS_3(NA)/Ni, ED-MoS_3(NA)/ITO and TD-MoS_3, respectively.

There is basically no difference in the (A) and (NA) sample, and no difference for nickel and ITO backings except, perhaps, that Ni-backed samples were about a factor of 2 thicker than ITO-backed samples, even though they were charged with roughly the same amount of lithium per a-MoS_3. The lithium concentration determined by ion beam analysis is in agreement with total charge calculations when the correct thickness of the sample is taken into account. The slope at the interface between a-MoS_3Li_x and the substrate is the result of convolution between beam energy spread (including straggling) and the true lithium depth profile. While the roll-off of sample ED-MoS_3(A)/ITO was in rough agreement (within a factor of 2) with the straggling effects, we believe that the sample thickness variations across the beam spot played a major role in the roll-off behavior of sample ED-MoS_3(NA)/Ni. The TD-MoS_3 sample showed a very uniform lithium distribution up to the limit of the depth profile.

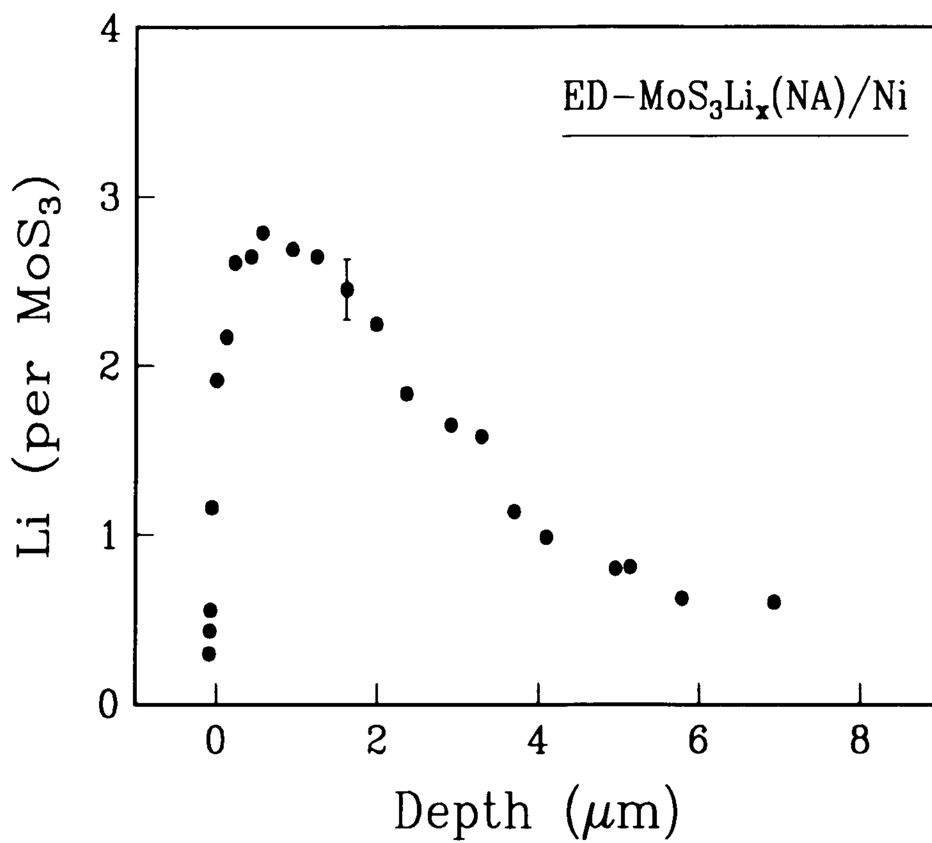

Figure 2.12 The absolute lithium concentration as a function of depth of an electro-deposited a-MoS_3(NA) thin film sample on nickel substrate.

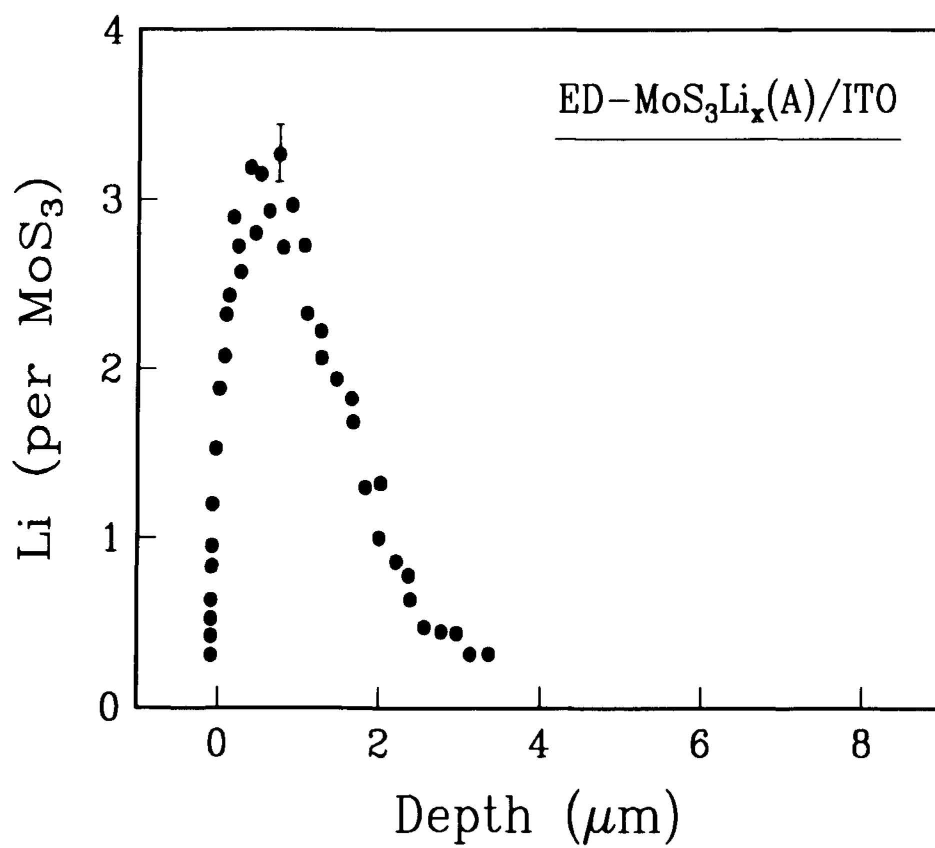

Figure 2.13 The absolute lithium concentration as a function of depth of an electro-deposited a-MoS_3(A) thin film sample on ITO thin film on glass substrate.

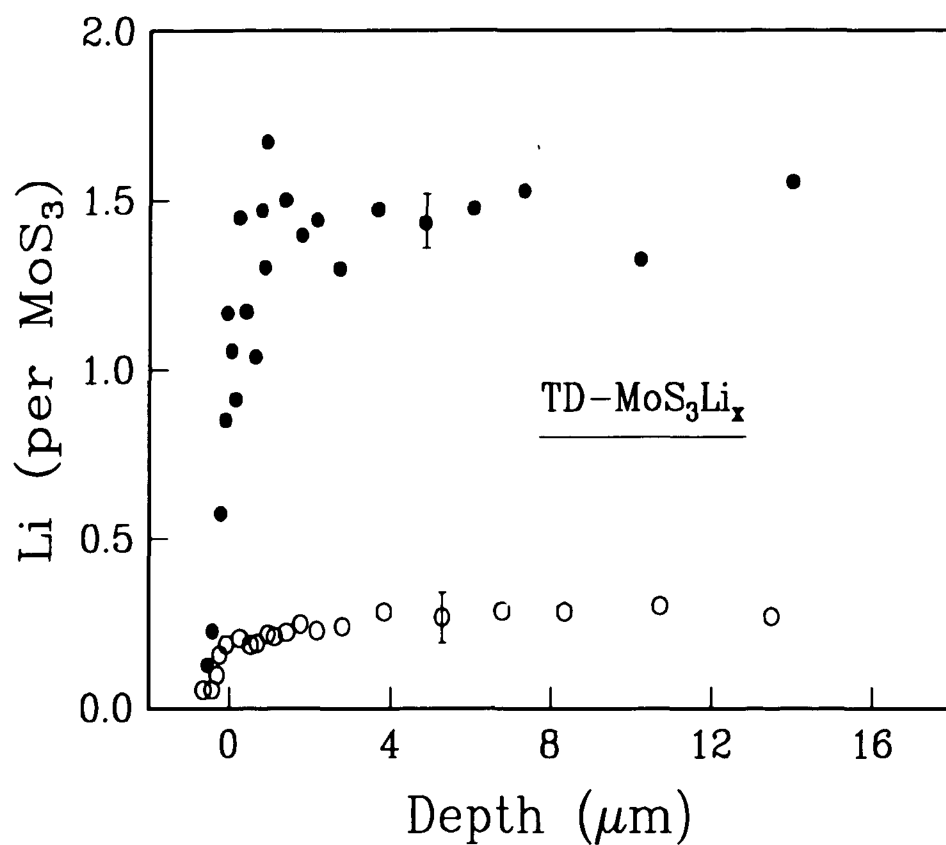

Figure 2.14 The absolute lithium concentration as a function of depth of two TD-MoS_3 pellet samples: 1.5 Li/MoS_3 (solid); 0.4 Li/MoS_3 (open).

The back side of TD-MoS_3 was also analyzed. The two sides of the sample were identical within the precision of the measurements.

The agreement between RNRA and electro-chemical analysis means that all of the lithium intercalated into the a-MoS_3 sample. If a layer of lithium had been formed on the surface of the a-MoS_3 sample, it would have been detected (in the form of a peak) if its thickness exceeded approximately 1500Å.

We believe that the resonant nuclear reaction analysis technique provides the best method for measuring depth profiles and absolute lithium concentration in a-MoS_3

Chapter Three

Oxygen Measurements in TiC and WC Superlattices

Introduction

Metal carbides are best known for their excellent high temperature properties. For example, titanium carbide is a very useful refractory material. Its light weight makes it particularly attractive in aerospace applications. Tungsten carbide is characterized by its extreme hardness and high melting point. Cemented tungsten carbides are widely used in drill tips and as metal-cutting tools.

Recent advances in ultra-thin film deposition techniques have made possible the creation of artificially ordered multilayer structures down to single atomic- layer dimensions. Metal carbide superlattices represent one group of such materials currently under investigation. The motivation is to look for structures with unique properties not found in nature. Metal carbide superlattices can also be used as uv and soft x-ray mirrors. The multilayer structure can enhance the reflectivity over a wide range of angles while still providing spectral

selectivity.

One of the problems in metal carbide superlattices is the possibility of metal oxide formation at interfaces. If enough oxide exists at the interface, it could compete with carbide formation and greatly affect the structural stability of the material. Auger electron spectroscopy and electron energy loss spectroscopy (EELS) have been the primary tools of metal carbide multilayer characterization. Other techniques, such as x-ray diffraction, have also been used. The AES and EELS are surface-sensitive techniques (< 100**Å**) and generally do not provide enough information deeper inside the sample. Ion beam analysis, with a depth scale of 10^2 to 10^4 **Å**, thus provides an important alternative tool.

It is well known that RBS is a quantitative analytical method. By simply measuring the energy distribution of backscattered ions, information can be obtained about the elemental composition and depth distribution of target materials.[21] A relative measurement can further improve the quantitative aspect of RBS by comparing the unknown to a suitable standard and eliminating, as much as possible, any uncertainties having to do with geometry, incident energy, etc. However, the detection limit and resolution of RBS is not uniform. For

example, all information is contained in the energy of the backscattered ion, and factors such as mass of the target and depth both contribute to an energy shift in the scattered ion. Because of the kinematic factor, RBS has poor mass resolution with heavy target elements, and the low Rutherford cross section of light elements means a poor sensitivity (or detection limit) for those elements. The latter case is especially serious when the signal from heavier elements extends into the region where signals from light elements are expected, as often occurs with thick targets.

Fortunately, the deficiency of RBS for light element detection is complimented by the existence of sharp and strong nuclear resonant reactions exclusively for light elements.[20] In certain favorable cases, the sensitivity, depth resolution, and quantitative determination of RBS can be improved dramatically. Chapters one and two provide two excellent examples of what the nuclear reaction technique can do that is beyond the capabilities of conventional RBS. Even a simple enhancement in cross section relative to the Rutherford scattering translates proportionally to an enhancement in sensitivity in otherwise similar circumstances. A resonant nuclear reaction will further improve the depth resolution. In this chapter the resonant nuclear reaction technique will again be used, this time for the detection of small amounts of oxygen and its

depth distribution in titanium-carbon and tungsten-carbon superlattices on silicon substrates. These samples have substantial amounts of carbon, yet the RBS signal from carbon is tiny and sits on top of the RBS spectrum from substrate silicon. Small amounts of oxygen do not show up at all in the RBS spectra. The resonant reaction used here to detect oxygen, $^{16}O(\alpha,\alpha)^{16}O$, differs from those resonant reactions discussed in previous chapters in that it is an elastic scattering process.[20] It does not produce any γ-rays, and it follows the same kinematic relations as RBS. Only the cross section is different. The lack of γ-ray detection has the an advantage in that a conventional RBS setup can be used without modification; only the data must be interpreted differently. On the other hand, it also has the disadvantage that not all of the weak points of RBS can be eliminated. For example, the signal from oxygen still rides on top of a strong background from substrate silicon, which is an important factor in determining the overall detection limit of this technique.

Rutherford Scattering versus Resonant Scattering

The low-energy $^{16}O(\alpha,\alpha)^{16}O$ reaction is one of the earliest reactions studied.[33] Figure 3.1 shows its excitation curve. For the sake of simplicity only data for a backward angle is displayed. A strong and isolated resonance occurs at a helium incident energy of 3.05 MeV, with a width of about 12 keV. This resonance happens to be strongest at backward angles, much stronger than the Rutherford cross section (indicated by the dashed line), and thus is the ideal candidate for oxygen measurements. However, its width is not very narrow, which limits the depth resolution that can be achieved using this technique.

Because of the nature of a resonance, one cannot judge the enhancement of signal by simply comparing the Rutherford cross section with the height of the resonant curve. A more meaningful way is to consider the area under the resonant peak, i.e., to integrate over the resonance width, and compare that to the same integration of the (slowly-varying) Rutherford cross section over the "same" width. (In theory, the first integration is from minus infinity to plus infinity, but the limits of the second integration can be defined in a practical sense.) Ignoring the contribution from the asymmetric term, the excitation

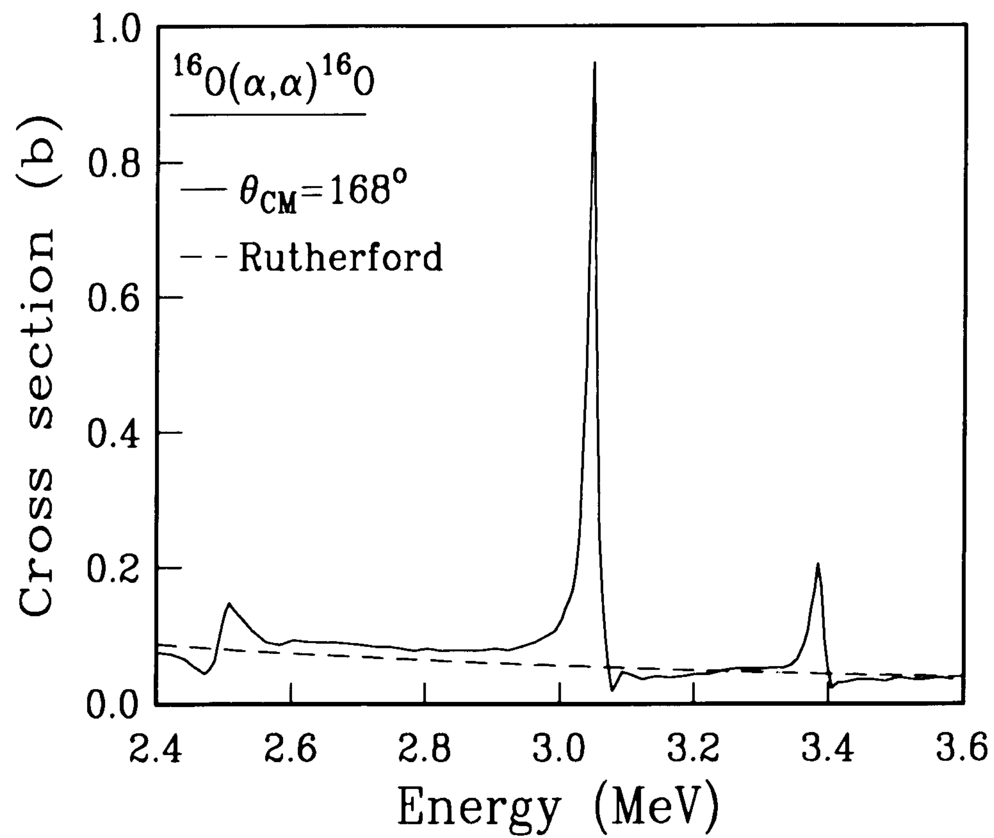

Figure 3.1 Excitation function of the $^{16}O(\alpha,\alpha)^{16}O$ reaction. For simplicity only data for a backward angle is shown. From ref. 33.

function near a resonance can be approximated by the Breit-Wigner relation,[30] so

$$Y_R \propto \int_{-\infty}^{\infty} \sigma_0 \rho(z) \frac{\Gamma^2/4}{(E(z)-E_R)^2 + \Gamma^2/4} dz \qquad (3.1)$$

where σ_0 is the strength of the resonance, ρ is the density of target nucleus, E_R is the resonant energy, and Γ is the width (FWHM). The normalization is such that the height of the excitation curve is σ_0. The Gaussian form used in Eqn. (1.1) is not appropriate here because the resonant width dominates in the present case. To carry out the integration one makes use of the fact that the stopping power is a slowly-varying function of energy (or depth), and, assuming that ρ is a constant,

$$Y_R \propto \sigma_0 \rho \left[\frac{dE}{dz}\right]^{-1} \int_0^{\infty} \frac{\Gamma^2/4}{(E-E_R)^2 + \Gamma^2/4} dE = \sigma_0 \rho \left[\frac{dE}{dz}\right]^{-1} \frac{\pi\Gamma}{2} \qquad (3.2)$$

In practice, the integration limits never need to exceed a few times the FWHM. For example, it could be restricted to a range of 2Γ. A fair comparison can then be made with the Rutherford cross section if the latter is also integrated over the same range:

$$Y_{Rutherford} \propto \sigma_{Rutherford}\, \rho \left[\frac{dE}{dz}\right]^{-1} (2\Gamma) \qquad (3.3)$$

The enhancement factor over which the resonant reaction out-performs conventional RBS can then be defined as:

$$R = \frac{Y_R}{Y_{Rutherford}} = \frac{\pi}{4}\frac{\sigma_0}{\sigma_{Rutherford}} \qquad (3.4)$$

A crude estimate can be made by reading off from Fig. 3.1. R ≈ 25.

Sample Structures

The TiC and WC samples studied had alternating titanium (or tungsten) and carbon layers repeated many times and grown (deposited) on silicon substrates.[34,35] The sample configurations are summarized in Table 3.1. In the following sections we will concentrate on one TiC sample and one WC sample. Results for other samples are very similar. The characteristics of these two samples are shown in Figs. 3.2 (TiC) and 3.3 (WC), respectively. The TiC sample had a unit structure of 8.8 Å of carbon and 20.6 Å of titanium, repeated 50 times to give a total thickness of 1470 Å (440 Å of carbon and 1030 Å of titanium). The WC sample had a unit structure of 7 Å of carbon and 7 Å of tungsten, repeated 150 times to give a total thickness of 2100 Å (1050 Å of carbon and 1050 Å of tungsten). In all cases the top layer was terminated by carbon. The thickness information is necessary to judge the depth resolution of the $^{16}O(\alpha,\alpha)^{16}O$ reaction in relation to the superlattice layer.

Table 3.1 Configurations of titanium-carbon and tungsten-carbon superlattice samples.

Configurations of titanium-carbon superlattice samples

Sample #	Ti (Å)	C (Å)	Periods
1	37.6	32.0	50
2(*)	20.6	8.8	50
3	25.6	10.2	50
4	27.0	41.0	65
5	20.2	4.7	50

Configurations of tungsten-carbon superlattice samples

Sample #	W (Å)	C (Å)	Periods
1	6	5	200
2(*)	7	7	150
3	10	20	150
4	10	13	65

Note (*) Detailed results given in text.

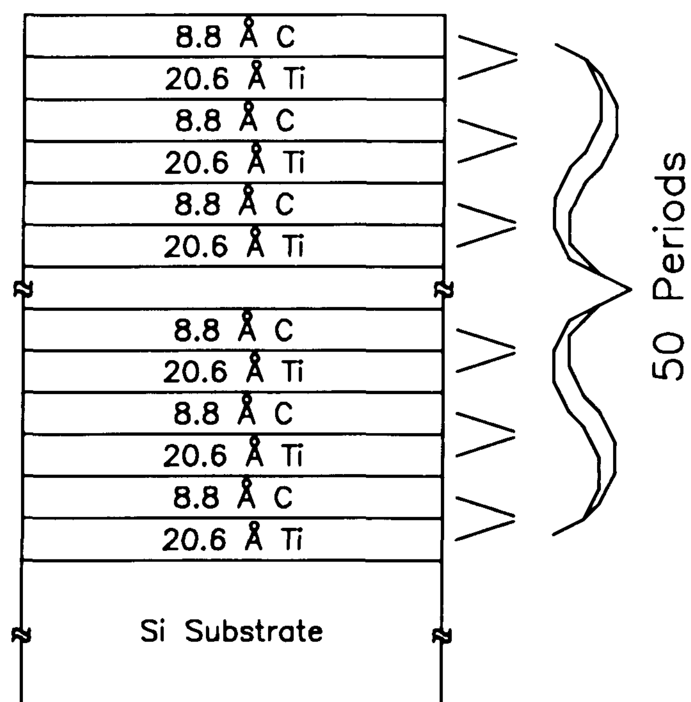

Figure 3.2 Structure of a titanium carbon superlattice sample grown on silicon substrate.

Figure 3.3 Structure of a tungsten carbon superlattice sample grown on silicon substrate.

Stopping Power of ^{4}He in TiC and WC Superlattices

A simple calculation of the stopping power of ^{4}He (based on standard references) shows that, at 3 MeV, it is about 25 eV/Å for carbon, 32 eV/Å for titanium, and 58 eV/Å for tungsten.[22] The width of the resonance (12 keV) would therefore cover a depth of at least several hundred angstroms. This is much larger than the superlattice repetition period for all of the samples (20 Å or less, about 50 Å for some samples). Therefore, the resonance is unable to resolve structures of individual superlattice layers. However, this width is considerably less than the total width of the superlattice, and a scan of the backscattering spectra over the $^{16}O(\alpha,\alpha)^{16}O$ resonant energy will be able to give the oxygen content in the near surface, inside, and rear interface (with substrate silicon) regions of the superlattice layer.

Based on the stopping powers for individual elements, an energy versus depth relation can be established by integrating the reciprocal stopping power, starting from the resonant energy (see chapter two, Eqn. (2.12)). Figure 3.4 shows the result of integration, for the TiC and WC sample structures of Figs. 3.2 and 3.3. The total energy loss over the superlattice layer can be obtained

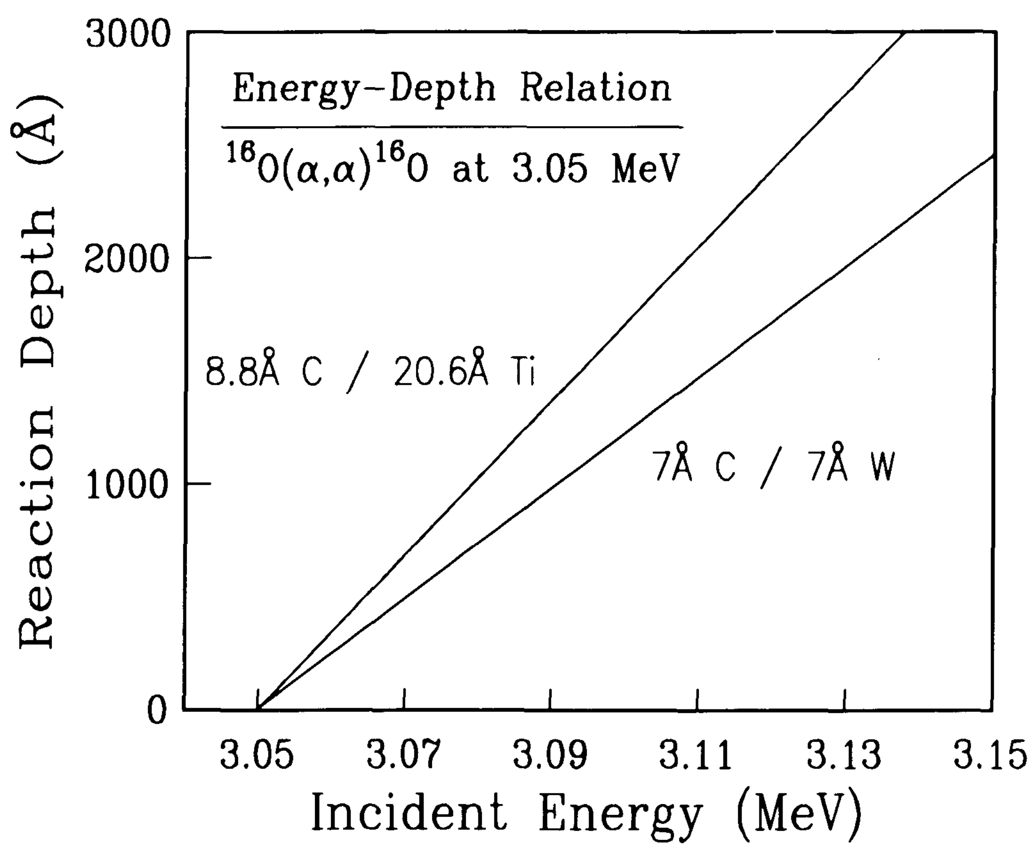

Figure 3.4 Reaction depth of the 3.05-MeV resonance of $^{16}O(\alpha,\alpha)^{16}O$ in Tic and WC superlattices as a function of incident beam energy.

from Fig. 3.4, giving about 43 keV for the TiC sample and 85 keV for the WC sample. The thickness of the TiC sample is just about at the lower limit for which a reasonable depth profile of oxygen can be made using this technique; reducing the superlattice layer by a factor of 2 would make the measurement rather unreliable.

The insensitivity of the reaction to details of the superlattice means that the superlattice can be treated as an alloy with appropriate compositions, in both the stopping power calculation and the backscattering simulation. The alloy has the same total thickness as the original superlattice layer. RUMP simulations of the RBS spectra of a superlattice and alloy show very little difference.[31]

Details of Experiment

1) Sample preparation

The samples were prepared using a Perkin-Elmer argon plasma rf-sputter deposition system.[34,35] The substrates were placed on a rotating water cooled platform below the sources (reactor-grade ATJ graphite and high-purity (99.95%) Ti or W). A shutter with a circular opening allowed the preparation of several samples under almost identical conditions. Typical base pressure was 5×10^{-5} Pa and the argon pressure during deposition was controlled using a capacitance manometer at an argon flow rate of 0.4 cc/sec. The silicon crystals were micropolished and heat treated at 400°C for 2 hours prior to depositions. The samples were characterized by transmission electron microscopy (TEM) and X-ray diffraction. Auger electron spectroscopy (AES) and electron energy loss spectroscopy (EELS) were also used to study the samples' structures, chemical compositions, and interface stabilities.

2) Backscattering measurement

The experimental setup was very similar to that described in chapter one. To make best use of the strong peaking of the $^{16}O(\alpha,\alpha)^{16}O$ cross section at backward angles, an annular detector placed at 180° was used to collect the backscattered particles. The detector had a hole in the center to allow the incident beam to pass through. The average scattering angle for this detector was about 175°. The beam current was between 10 and 20 nA. The integrated beam current (charge) was not measured, since it was not needed. All normalizations were made relative to the backscattering yields from titanium or tungsten, for which the cross sections are known to be purely Rutherford.

Results and Discussion

Figure 3.5 shows the backscattering spectrum from the TiC sample at 2.2 MeV. At this energy the cross sections of ^{4}He on both carbon and oxygen are close to Rutherford.[20] A small amount of argon can be seen in the spectrum, characteristic of the argon plasma deposition system. The substantial amount of carbon present in the superlattice layer produces only a small bump on top of the signal from substrate silicon. No evidence of any oxygen can be found. This confirms the fact that conventional RBS is not sensitive enough for the detection of oxygen in small amounts. The whole spectrum (except the argon peak) can be fitted very well by a RUMP simulation, another indication that the cross sections are indeed close to Rutherford.

As the energy of the incident beam was raised to 3.06 MeV, just above the 3.05-MeV resonance of $^{16}O(\alpha,\alpha)^{16}O$, a clear oxygen signal appeared in the backscattering spectrum of the TiC sample (Fig. 3.6). This energy was just enough to place the whole $^{16}O(\alpha,\alpha)^{16}O$ resonance inside the superlattice layer. We therefore had a measure of the oxygen content near the surface region.

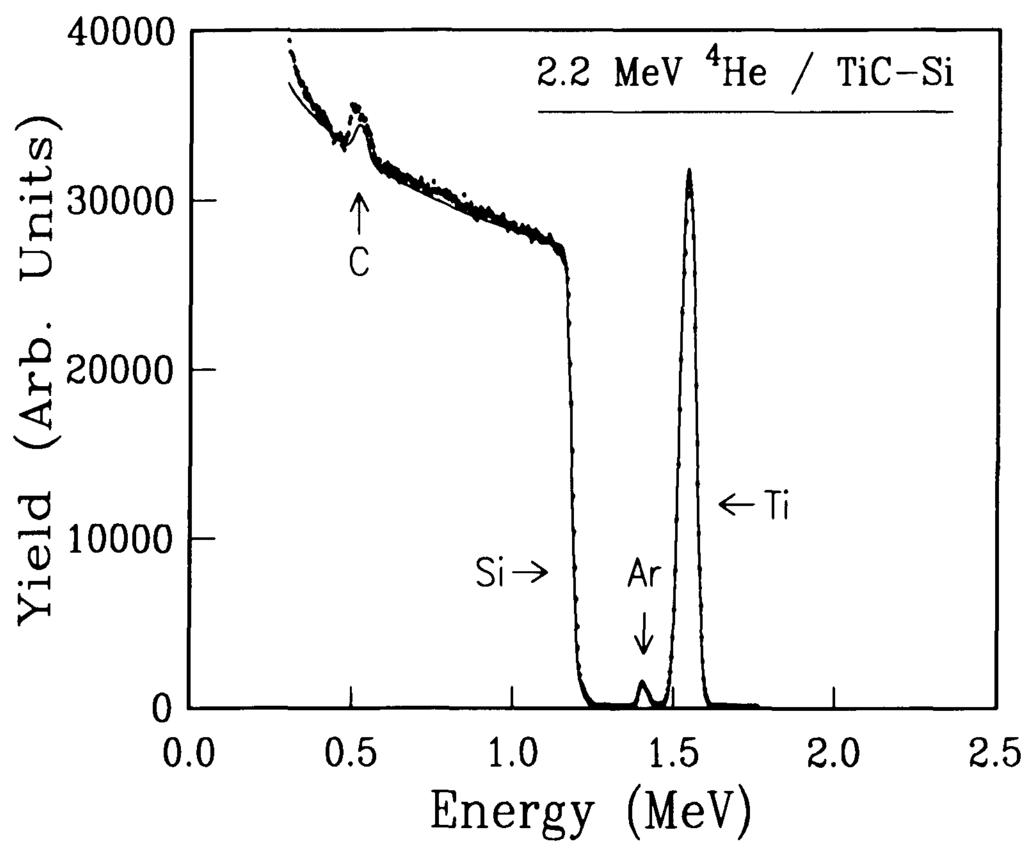

Figure 3.5 Backscattering spectrum of 2.2 MeV ^{4}He beam on the TiC superlattice sample. The solid line is a RUMP simulation. A small amount of argon can also be seen.

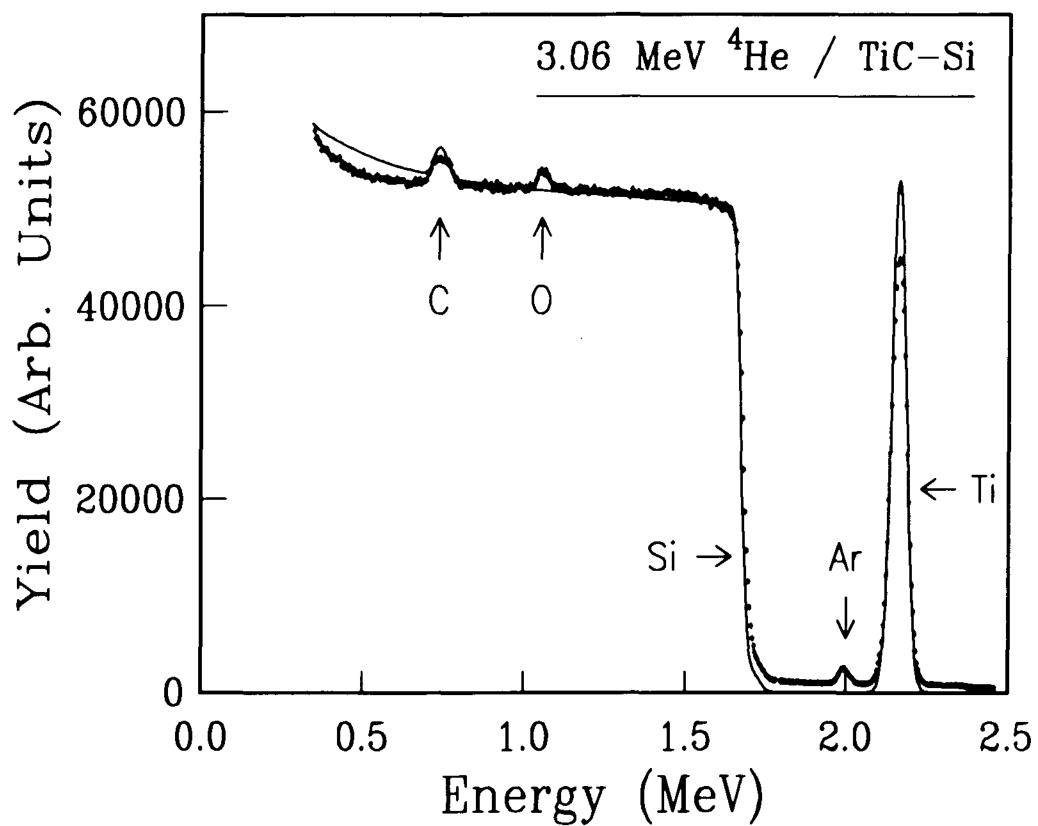

Figure 3.6 Backscattering spectrum of 3.06 MeV ^{4}He on the TiC sample. Width of oxygen peak is smaller than that of carbon, indicating that it is from only portion of the superlattice layer.

When the incident beam was at an energy of 3.08 MeV, we were in the situation where the resonance was still wholly within the superlattice layer but near the rear edge. As shown in Fig. 3.7, the amount of oxygen was approximately the same. We interpret this as evidence that oxygen is present more or less uniformly throughout the superlattice layer, possibly at every Ti/C interface (a likely place for oxygen). The amount of oxygen can be estimated from the area under the oxygen peak and the enhancement factor, Eqn. (3.4). The result we obtain is about 0.5%. This number has a fairly large relative error bar, partly because of the lack of precise cross section data for the $^{16}O(\alpha,\alpha)^{16}O$ reaction. In all TiC samples measured, approximately the same amount of oxygen was detected throughout the superlattice layer.

The different behavior of resonant reactions and Rutherford backscattering under a slight change of incident energy provides another clear indication that oxygen from various regions of the superlattices has been sampled. To the first approximation, the backscattering energy E′ is

$$E' = K(E_0 - \varepsilon d) - \varepsilon d \approx E_0 - 2\varepsilon d \qquad (3.5)$$

where E_0 is the incident energy, K is the kinematic factor, ε is the stopping power and d is the depth. In the last step K is taken to be unity and ε is assumed to be a constant. The result is that a fixed feature of the spectrum, for

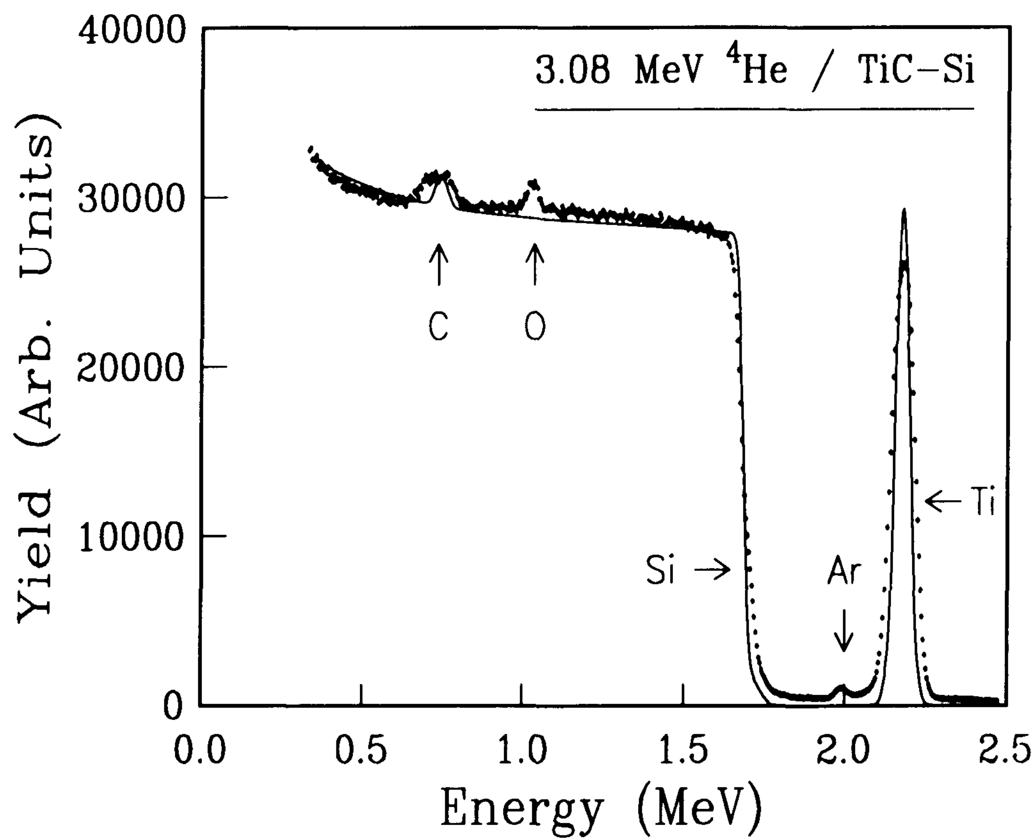

Figure 3.7 Backscattering spectrum of 3.08 MeV ^{4}He on the TiC superlattice sample. Oxygen in this case is from the rear edge of the superlattice. The solid line is a RUMP simulation.

example, the front edge, d=0, will move along with the incident energy in the same direction. For a resonant reaction, however, there is an additional constraint that the energy before scattering must be equal to the resonant energy,

$$E_0 - \varepsilon d = E_R \tag{3.6}$$

so that

$$E' = K(E_0 - \varepsilon d) - \varepsilon d \approx 2E_R - E_0 \tag{3.7}$$

and the feature in the spectrum actually moves in the opposite direction by approximately the same amount. The carbon and oxygen peaks in Figs. 3.6 and 3.7 are all in good agreement with Eqns. (3.5) and (3.7), respectively, another indication of the different reaction mechanisms for these two elements.

Shown in Fig. 3.8 is the backscattering spectrum of the WC sample with ^{4}He incident at of 3.06 MeV. Again some amount of argon was present. The oxygen peak was also strong and clear. This indicates that oxygen is at the surface or near surface region of the superlattice. Similar spectra with 3.10 and 3.18 MeV incident beams showed no trace of oxygen (Figs. 3.9 and 3.10). Thus, in contrast to the TiC samples, the WC sample had oxygen only in the near surface region. This behavior was observed for all WC samples measured.

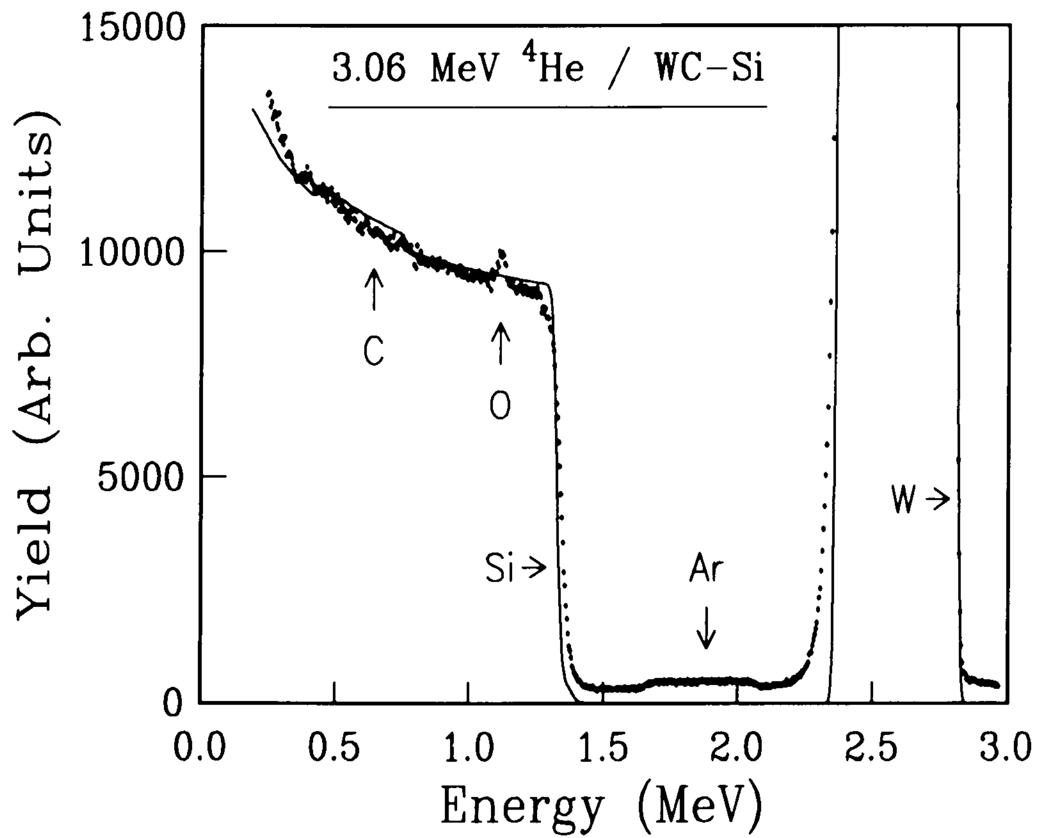

Figure 3.8 Backscattering spectrum of 3.06 MeV ^{4}He beam on the WC sample. Oxygen can be found in this region of sample (near surface). The solid line is a RUMP simulation.

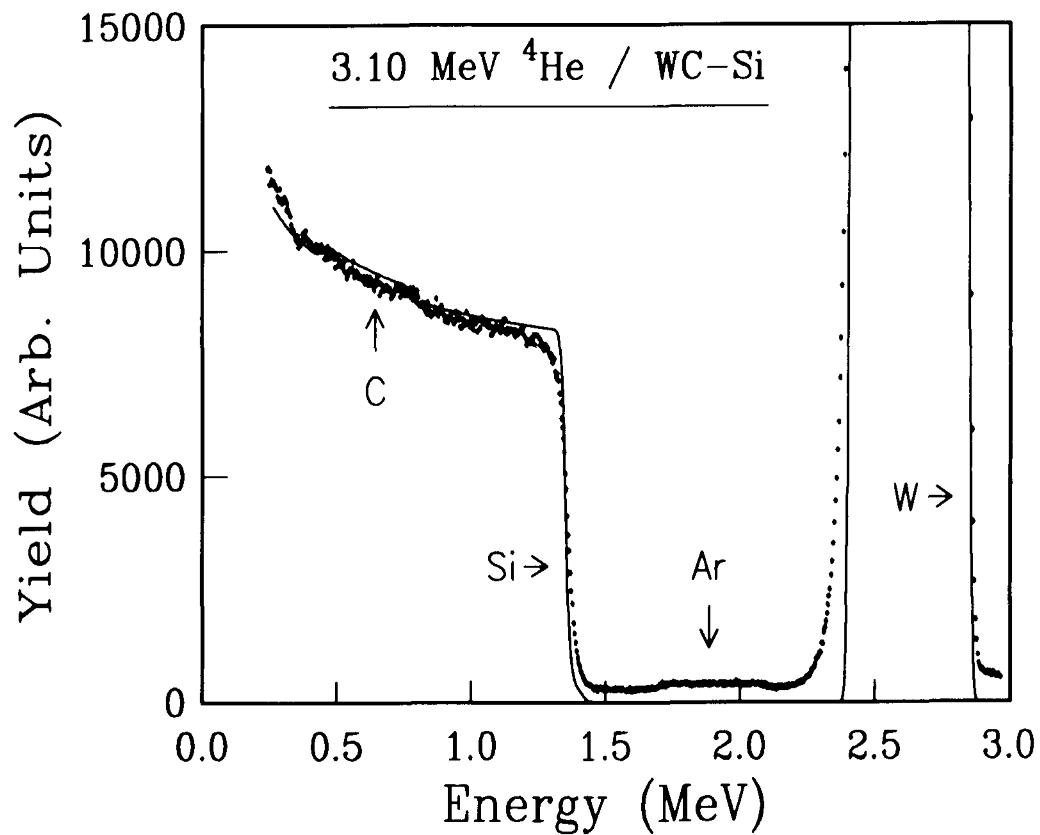

Figure 3.9 Backscattering spectrum of 3.10 MeV ^4He on WC sample. At this energy the resonance occurs inside the superlattice. No oxygen is detected. The solid line is a RUMP simulation.

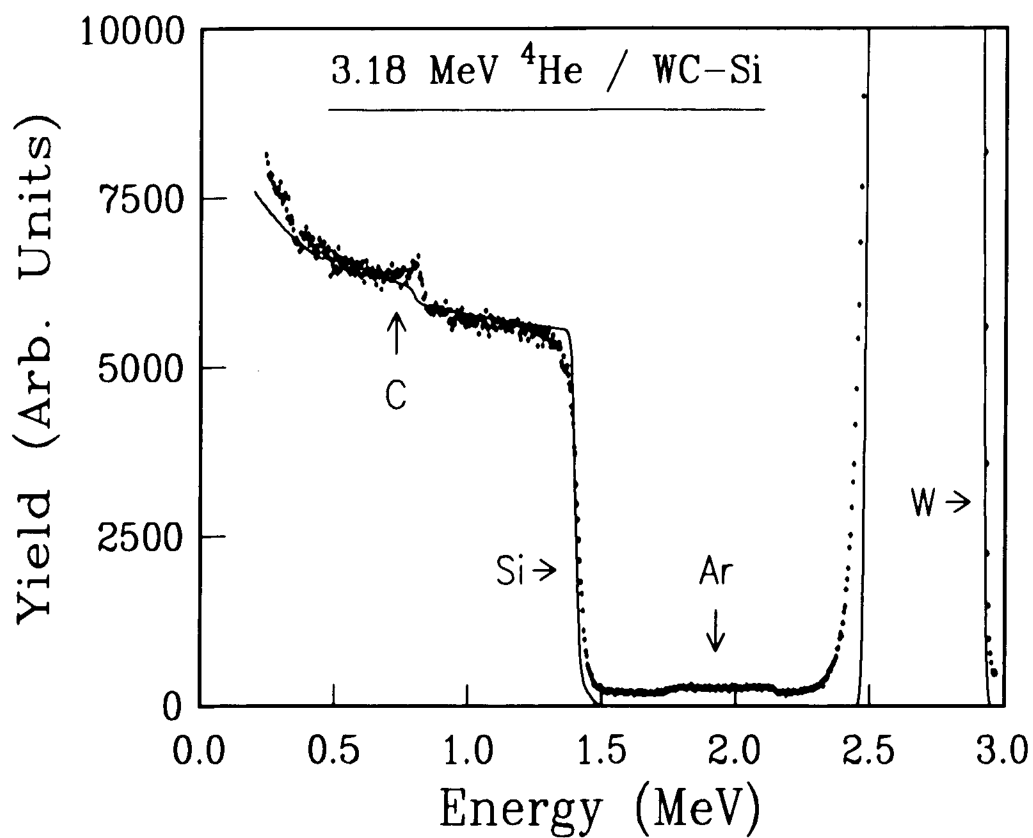

Figure 3.10 Backscattering spectrum of 3.18 MeV ^{4}He beam on the WC sample. No oxygen is detected. The distorted carbon peak is due to the non-Rutherford nature of the carbon cross section.

The distorted carbon peak at 3.18 MeV incident ^{4}He energy is due to the non-Rutherford nature of the $^{12}C(\alpha,\alpha)^{12}C$ cross section above 3 MeV.[36] In fact, the shape of the carbon peak is in good agreement with the excitation function (Fig. 3.11). It would be quite erroneous to do quantitative analysis using the carbon peak without taking into account the deviation of the $^{12}C(\alpha,\alpha)^{12}C$ cross section from that of Rutherford scattering.

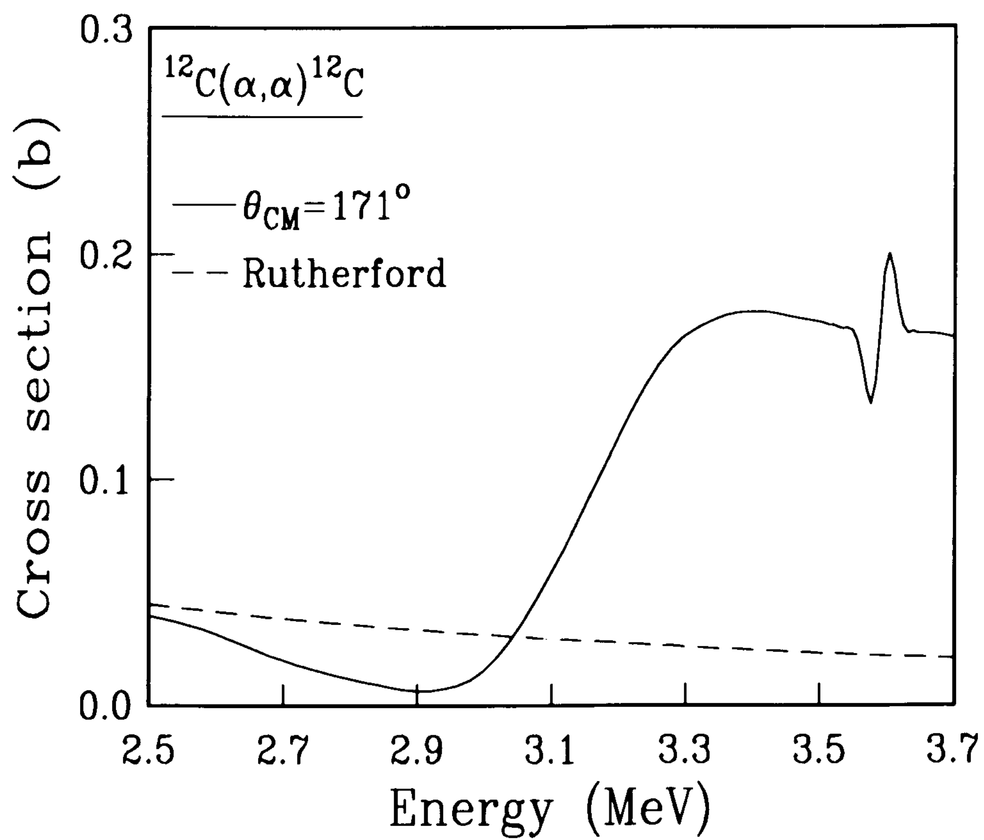

Figure 3.11 Excitation function of the $^{12}C(\alpha,\alpha)^{12}$ reaction. For simplicity only data for a backward angle is shown. From Ref. 36.

Summary

We have performed a resonant nuclear reaction analysis of the oxygen distributions in TiC and WC superlattices samples with different unit structures and repetition periods. In all cases the oxygen contents were very much independent of the details of superlattices. About 1 to 2 percent of oxygen was found to be present uniformly throughout the superlattice layers for all TiC samples. Because of the great affinity of titanium towards oxygen, we believe that oxygen exists in the form of titanium-oxide at the titanium-carbon interfaces. This conclusion is consistent with the observations of AES and EELS measurements.[34] For WC superlattices, oxygen was restricted to the surface or near surface regions of the samples (< 100Å). The bulk WC superlattice had less than 0.1% of oxygen. The resolution of this technique did not allow us to measure oxygen at each interface, which would have required that the individual superlattice layers be at least 200 Å thick. The absence of observed oxide layers in the bulk WC superlattices suggests that these materials will have greater stability for optical devices and structural components in high temperature environments.[35]

Chapter Four

Energy Loss and Straggling of Channeled 1-MeV H^+ Ions

Introduction

The passage of a charged particle through a solid is governed by its energy loss function, or the stopping power of the target material. For incident particles with velocities much greater than the target Fermi velocity, the primary cause of energy loss is via collisions with target electrons. The statistical nature of the collision process leads to another important phenomenon, the spreading of the energy distribution around its mean value, called the straggling effect. The energy loss and straggling can be viewed as the first and second moments of the energy distribution function.

Energy loss and straggling are a basic form of charged particle interaction with matter. Its study can be traced back to the beginning of this century. Some of the basic theories will be reviewed. Besides their obvious importance in fundamental research, they also play a key role in almost any technique utilizing ion beam analysis or ion beam modification of materials. In RBS and

RNRA, the depth scale and signal height both depend on energy loss, and straggling limits the depth resolution deeper inside the sample. With regard to ion beam modification, ion implantation is today a routine procedure in semiconductor device processing. Device dimensions are getting smaller and smaller in the present very large scale integration technology, so that accurate control of the implanted ions, such as their depth profile, is extremely important and requires the knowledge of energy loss and straggling for both random and channeled ions.

Energy loss and straggling in amorphous materials

As can be seen later in this section, "amorphous" material means that the impact parameter distribution of the incident ion with respect to the electrons is uniform. Thus, the target material need not be truly "amorphous." For example, poly-crystalline samples can generally be considered amorphous for this purpose. A single-crystalline target can behave as if it were "amorphous" if it is oriented "randomly" with respect to the incident ion beam, i.e., not along any major crystal axes or planes.

Bohr, basing his calculations on a simple classical model, was the first to derive expressions for the stopping power due to electrons,[37]

$$\frac{dE}{dz} = 4\pi N Z_1^2 Z_2 e^4 \frac{1}{m_e v^2} \ln(\frac{b_{max}}{b_{min}}) \qquad (4.1)$$

and the standard deviation of the distribution (straggling) at a depth x,

$$\Omega_B^2 = 4\pi N Z_1^2 Z_2 e^4 z \qquad (4.2)$$

where N is the number of target atoms per unit volume, Z_1 and Z_2 are the atomic numbers of incident ion and target atoms, respectively, m_e is the electron

mass, v is the ion velocity, and b_{max} and b_{min} are the maximum and minimum impact parameters.

One notes that in Bohr's calculation both the stopping power and the straggling are proportional to the total number of electrons per unit volume, Z_2N and the (average) energy transfer per collision, which is proportional to $(Z_1e^2)^2$. The impact parameter has been averaged out (no channeling present).

Bohr's theory is based on the assumptions that: i) the energy transfer per collision is small compared to the energy of the ion, and ii) the electrons are free and at rest. The first assumption is generally true for MeV ions, the second may not be. The electron binding energy could easily be comparable to the averaged energy transfer per collision. The most successful model to take that into account is based on the Thomas-Fermi treatment of the electron gas, leading to the Bethe-Bloch stopping power formula[38,39] which usually gives a very good fit to the experimental data:

$$\frac{dE}{dz} = 4\pi N Z_1^2 Z_2 e^4 \frac{1}{m_e v^2} \ln\left(\frac{2m_e v^2}{I}\right) \tag{4.3}$$

where I is the mean excitation energy. A similar modification for the straggling, due to Lindhard and Scharff,[40] gives the result:

$$\Omega^2 = \begin{cases} \Omega_B^2 & \chi > 3 \\ \Omega_B^2 L(\chi) & \chi \leq 3 \end{cases}, \quad \chi = \frac{1}{Z^2}\left(\frac{V}{V_B}\right)^2 \tag{4.4}$$

where V_B is the Bohr velocity ($V_B = \alpha c$, where α is the fine structure constant and c is the velocity of light).

Chu has calculated energy loss[41] and straggling[42] using Hartree-Fork atomic wave functions. His calculations show a pronounced oscillation in both the energy loss and straggling with respect to the target atomic number, Z_2, arising from shell effects (tails of the atomic wavefunctions).

The energy loss of a compound target of the form A_mC_n is presumed to be related to the individual elemental contributions by Bragg's rule:[43]

$$\frac{1}{N_{A_mC_n}}\frac{dE}{dz_{(A_mC_n)}} = \frac{m}{N_A}\frac{dE}{dz_{(A)}} + \frac{n}{N_C}\frac{dE}{dz_{(C)}} \tag{4.5}$$

This rule has been verified experimentally within 1%, except for some polymers and sometimes for compounds consisting of gaseous elements when in elemental form[20] (i.e., NaCl). A similar rule for straggling has been proposed:[20]

$$\frac{1}{N_{A_mC_n}z}\Omega^2_{(A_mC_n)} = \frac{m}{N_A z}\Omega_A^2 + \frac{n}{N_C z}\Omega_C^2 \tag{4.6}$$

Because of the lack of experimental measurements of straggling for compound materials, this straggling additivity law cannot be verified at the present time.

Energy Loss and Straggling of Channeled Ions

Under channeling conditions[44], incident particles are steered into the channel (inter atomic space) along a major crystal axis (or plane) of the single-crystalline target. An obvious consequence of channeling is that the incident particle flux distribution becomes non-uniform. The backscattering yield, which depends on close encounters, or small impact parameter collisions, is drastically reduced. The interaction between target electrons and the channeled ions depends on the details of the flux distribution and the local electron density.

The transverse energy (or momentum) of the incident ion can be used to describe the behavior of the particle. It is basically determined by the angle of incidence relative to the channeling axis (or plane). A crude picture of the channeling process is that ions undergo "oscillations" perpendicular to the channel, the amplitude (and period) of which is a measure of the angle of incidence.

The impact parameter, b, which was assumed to be uniformly distributed and averaged out in the expressions for energy loss and straggling in amorphous

targets, now plays an important role. The energy loss and straggling have a strong dependence on the transverse energy (or equivalently, the incident angle). Anything that alters the trajectory or electron density distribution will affect the energy loss and straggling parameters.

Because of these complications, the theory of energy loss and straggling for channeled ions is difficult to develop. As a first approximation, a decrease of the energy loss is expected for well-channeled ions, because they encounter fewer electrons. And the law of angular and spatial average[44] states that those ions which do come close to the target nuclei (not-so-well-channeled ions) should experience a larger energy loss so that the "averaged" value comes out to be the same as for amorphous materials. One can generalize the above argument for the case of straggling. If, as Bohr's theory of straggling states, the straggling arises from the statistical uncertainties associated with collisions between the incident ion and target electrons, then a decrease in the energy loss, which corresponds to a decrease in the number of collisions, should also imply a decrease in the value of the straggling parameter. Again, because ions with different trajectories (or incident angles) experience different energy loss, one should expect to see a deviation of the shape of the particle energy distribution from an ideal Gaussian. The high end of the energy distribution corresponds to

well-channeled ions and the low energy side corresponds to the less well-channeled ions.

The first treatment of channeling energy loss is Lindhard's two-component theory.[45] Later, Appleton and co-workers recognized the importance of separating the contributions due to the core electrons from those due to the valence band.[46] A formal theory of the problem is the quantum mechanical calculation of Esbensen and Golovchenko, based on an impact parameter treatment.[47] Using quantum mechanical perturbation theory and some generalized sum rules, Esbensen and Golovchenko found that at high energies the only required quantities are Bethe's I-value (the mean excitation energy) and the ground state electron charge density, whereas at low energies the energy loss can be expressed in terms of generalized dipole oscillator strengths. The Monte Carlo simulation is another widely used tool. In a Monte Carlo simulation, a computer program uses a simplified, periodic (in depth) potential to replace the real potential imposed on an incident projectile by the rows or planes of target nuclei. The program then calculates the trajectory of individual ions as they pass through the target and interact with the periodic potential. An energy loss profile (or any other quantity) can be established by following the paths of enough randomly selected projectiles. For straggling the

theories are very much under-developed and Monte Carlo may be the only calculational method available.

In conclusion, the theory of energy loss and straggling for channeled particles is far from complete. Quantitative behavior of the energy loss needs to be established. The straggling theory has hardly been developed at all. Experimental data of straggling of channeled ions is rare.

Experimental Methods

The basic way to measure energy loss and straggling is to place a target of appropriate known thickness in the path of a beam with the desired energy and collimation, and to measure the beam energy distribution before and after the beam passed through the target layer. Depending on the channeling condition of the ions in target, one measures the energy loss and straggling for channeled (or non-channeled, random) ions. Two geometries are available to achieve the above goal, the transmission geometry and the backscattering geometry.

In the transmission geometry, the target is a very thin and self-supporting foil. The beam energy spectrum of the incident ion is recorded with and without the target in position (Fig. 4.1). The amount of shift (toward lower energies) of the averaged beam energy is the energy loss, and the additional broadening of the beam energy distribution gives the straggling parameter. The difficulties of this type of measurement are: 1) the self-supporting target foil, usually in the thickness range of 10^3 to 10^4 Å, is extremely fragile and very hard to handle; 2) the detector used to measure the beam energy spectrum itself has an intrinsic

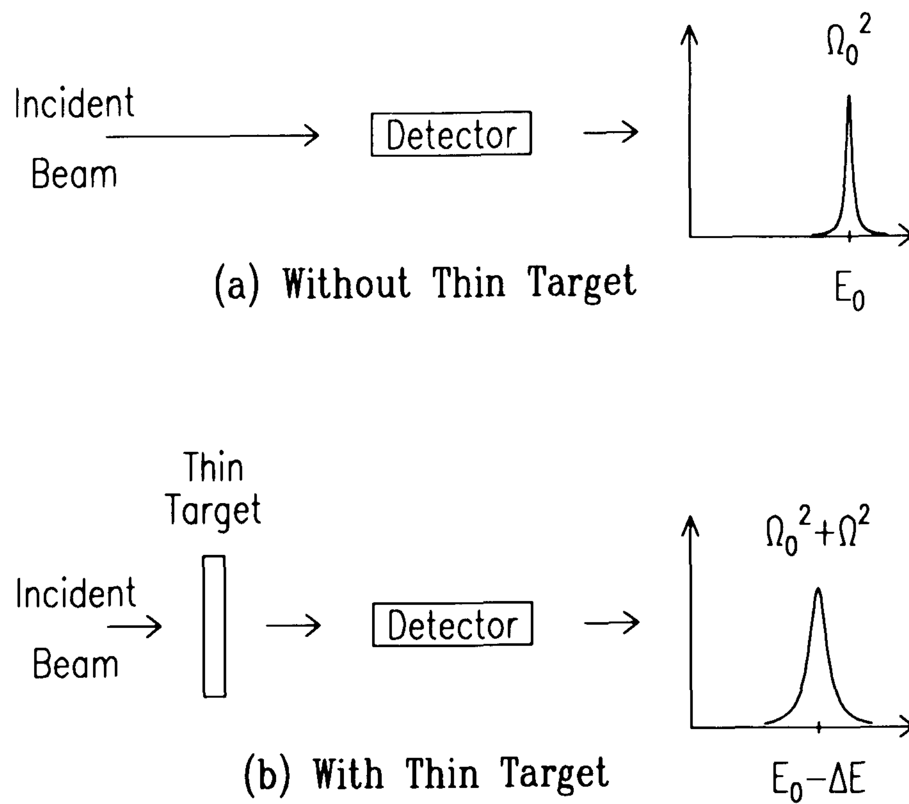

Figure 4.1. Energy loss and straggling measurement -- transmission geometry. Energy distribution of the incident beam (peak and width) is recorded with and without the target.

energy resolution that can easily exceed that of the straggling produced by a target of sub-micron thickness; 3) the roughness, or small scale variations in target thickness produces effects which are indistinguishable from straggling.

In the backscattering geometry, the spectrum of backscattered particles is observed (Fig. 4.2). The target in this case can be a thin layer evaporated (or somehow grown) on a suitable substrate. The substrate material should be light in atomic weight, if possible, so that the backscattering from the top layer is easily separable from substrate backscattering. The backscattering spectrum of a layer of finite thickness is in the form of a "bump." The width of the bump is related to the energy loss in the thin layer target, and the sharpness of both the higher and lower energy edges of the bump give information on the width of the beam energy distribution before and after passing through the top layer.[21] These widths can be de-convoluted to yield the straggling parameter. The backscattering geometry eliminates the need to deal with thin target, but at the same time introduces some complications as well. The incident particle goes through the top layer twice, and the mean energies of the particle in these two passes differ by the kinematic factor, K. Therefore both the energy loss and straggling measured this way are some kind of average of essentially two separate incident energies. Of course, for light particle incident on a heavy

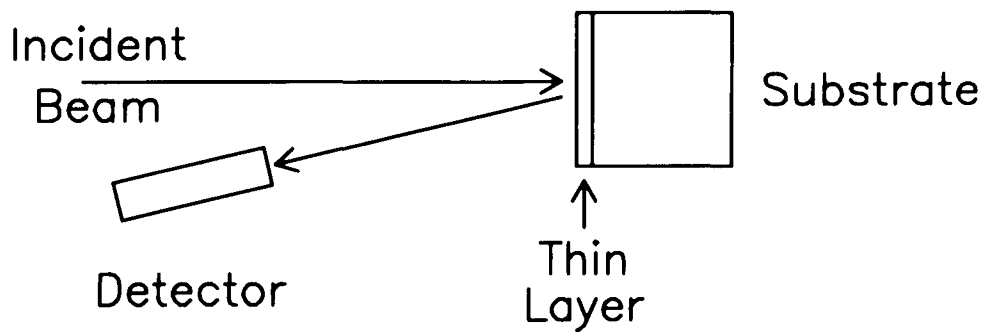

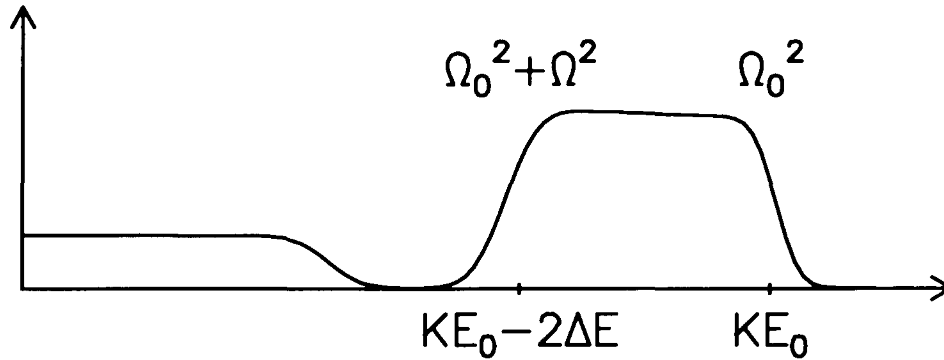

Figure 4.2 Energy loss and straggling measurement -- backscattering geometry. The target does not have to be a self-supporting thin film. This figure assumes that the substrate is lighter than the top layer.

target the kinematic factor approaches unity and the averaging effect does not play an important role. As in the case of transmission geometry, detector energy resolution and target roughness impose limitations on the results obtained from backscattering measurements.

A relatively new method to measure the energy loss and straggling is to use sharp resonances in nuclear reactions, such as (p,γ) and (α,γ) reactions on light nuclei.[48,49] There are many resonances whose natural widths are extremely narrow, and which therefore are especially promising for the straggling parameter measurements. The method can be applied to self-supporting thin films as well as evaporated targets. The only requirement is that the layer to be measured (the first layer) is followed by a second layer (thin or thick) which contains the isotope producing the desired nuclear reaction (Fig. 4.3). One proceeds with a measurement of the yield function on the second layer with and without the first layer in place. The yield curve without the first layer gives the convolution of intrinsic beam energy distribution with the width of the resonance. For example, if the second layer is thinner than the combined width of the resonance and the beam energy distribution, the yield curve essentially reproduces the combined width. A thick second layer, on the other hand, produces a step-like yield function whose sharpness is determined by the

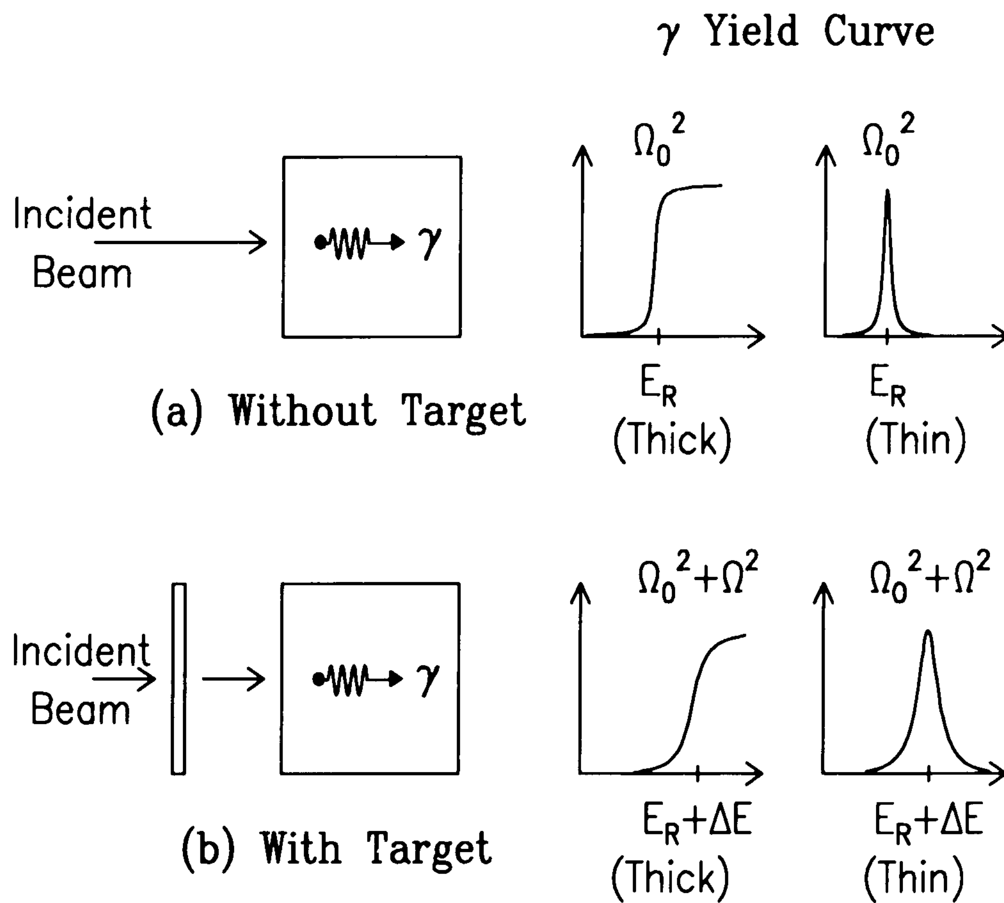

Figure 4.3 Energy loss and straggling measurement -- transmission geometry utilizing a resonant nuclear reaction to obtain the beam energy profile.

combined width. In either case the center of the yield function gives the resonant energy.

The yield function with the first layer in place will be shifted as well as smeared out due to the contribution of the energy loss and straggling from the first layer. Specifically, the resonant energy will appear higher and the resonant width will be broadened. As in the case of transmission geometry, the shift in the peak (thin second layer) or center of step (thick second layer) of the yield function is a measure of the energy loss in the first layer, and any additional broadening is directly related to the straggling effects. In this sense, the resonant reaction technique is basically a transmission type experiment, but the transmitted particle energy spectra are measured by a resonant reaction, rather than by a charged particle detector. This has the obvious advantage that the resolution obtainable is limited by the width of the beam/resonance, which in many cases is much smaller than the resolution of the detector. On the other hand, one should note that measurements can only be made at discrete energies (the available resonant energies). Of course, problems such as target roughness still remain, plus the fact that much more time is generally needed to obtain a reasonably good yield function than to obtain a spectrum directly from a detector.

This technique was first mentioned in 1977, and was later used by Bond *et al*[48] in their measurement of the proton straggling in GaAs. The most comprehensive study was done by Kido,[49] who demonstrated that the resonant reaction technique could be used to obtain reliable straggling parameters systematically. Kido measured the energy straggling of (non-channeled) protons in many elements at several energies (the choice of energy is not continuous in this technique). He found that the straggling parameters for amorphous solids basically followed the predictions of the theory of Lindhard and Scharff (Fermi gas model)[40] and were also consistent with the predictions of Chu's Hartree Fork calculations.[41] Kido's experimental results were not sufficiently precise to discriminate between the two theoretical calculations.

A universal problem associated with any straggling measurement is the fact that a variation in target thickness over the beam spot is indistinguishable from straggling effects. This problem is sometimes difficult to avoid because the beam spot size (~ 1 mm) is 3 to 4 orders of magnitude larger than the depth (~ 10^3**Å**).

Our Study

We have performed a preliminary study of the energy loss and straggling of 1 MeV protons near the silicon (001) channeling minimum, using the resonant nuclear reaction technique and transmission geometry. The measurements were similar to those of Jin and Gibson,[50] and some earlier work by Appleton and Gibson.[46] Instead of observing the backscattering (from Au) of the transmitted particles, the nuclear reaction technique was used so that both the energy loss and straggling parameters could be obtained at the same time. By changing the angle of incidence of the channeled ion, we also studied the channeling behavior as a function of transverse momentum to correlate channeling to energy loss and straggling. This is the first attempt to measure the angular dependence of straggling in channeled ions using the resonant nuclear reaction technique.

The nuclear reaction used for this measurement was the familiar 0.922-MeV resonance in $^{27}Al(p,\gamma)^{28}Si$. The same reaction was used in chapter one for the determination of the alloy composition in $Al_xGa_{1-x}As$. The width of the resonance is very narrow (~ 100 eV) so that the system resolution is

determined by beam energy resolution (~ 2 keV). A piece of aluminum foil was used as the second layer in which the resonance takes place. A 3x3 in NaI(Tl) detector was placed right behind the aluminum to collect the high energy γ rays.

The crystal used for this study was an 8000-Å silicon thin film, about 6 mm in diameter. A self-supporting target was needed to achieve the high crystal quality necessary for channeling. Note that channeling must be avoided in the layer that produces the nuclear reaction (i.e., the aluminum must be amorphous), and it is not possible to grow single crystal on an amorphous substrate. The sample was prepared by Dr. H. S. Jin using boron diffusion and selective chemical etching to remove the back side from an (001) silicon wafer. Details of the diffusion and etching process can be found in Ref. 51. The sample was mounted on a 2-axis goniometer in front of the aluminum target. Two surface barrier particle detectors at 135° each recorded the backscattering spectra from silicon to monitor the channeling conditions and to align the sample relative to the incident beam direction.

The accelerator and beam line setup was the same as previously described, except that additional slits were installed to collimate the beam to the necessary angular divergence. The slits were 3 mm and 1 mm in diameter and

were separated by a distance of 1.5 m. The goniometer, two particle detectors, thin silicon target, aluminum foil, and NaI detector housing were mounted in two 8-in Dependex crosses at the end of the beam line as shown in Fig. 4.4. The aluminum target also served as the charge-collecting device. A 300-V bias was applied to stop secondary electron emission which leads to a false reading of the beam current.

The goniometer was designed by and purchased from Appleton. Each axis was 360° rotatable with an angular resolution of better than 0.1°, plus a vertical translational stage with about 2 inches of travel. A Maxwell Electronics intelligent stepping motor controller drove the goniometer remotely. The stepping motors had shaft encoder feedback circuit to ensure error-free motion. Both the stepping motor controller and four multichannel analyzers were under the control of an IBM PC for fully automated data acquisition.

The silicon thin target was checked for thickness uniformity across its surface via the vertical translational stage and found out to be very uniform (5%) (Fig. 4.5). The (001) axial channeling dip was then located. The backscattering yield at the channeling minimum was about 4% of a random spectrum from the near surface region. After 3 days of continuous running, the channeling

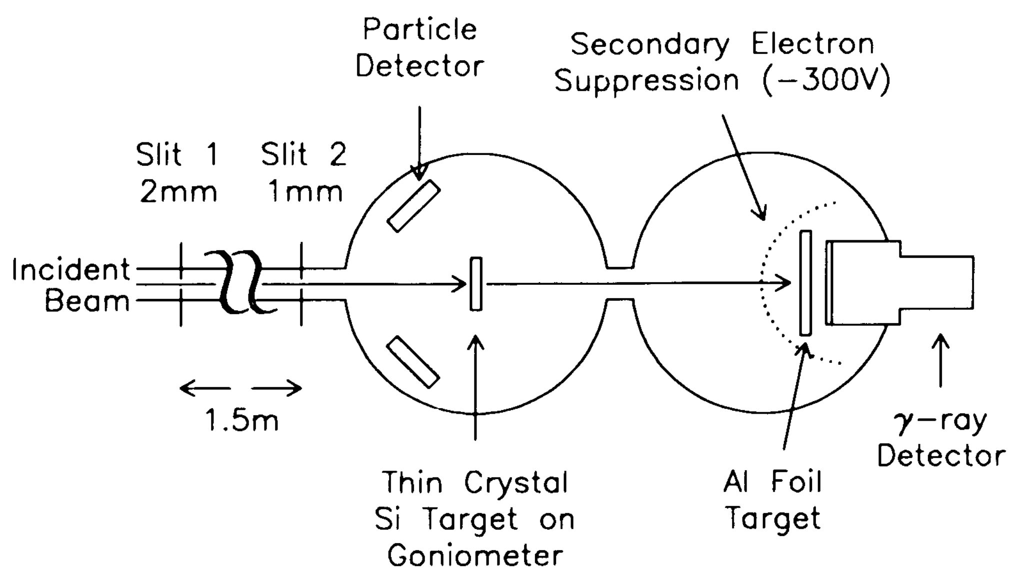

Figure 4.4 Target chamber for the energy loss and straggling measurement.

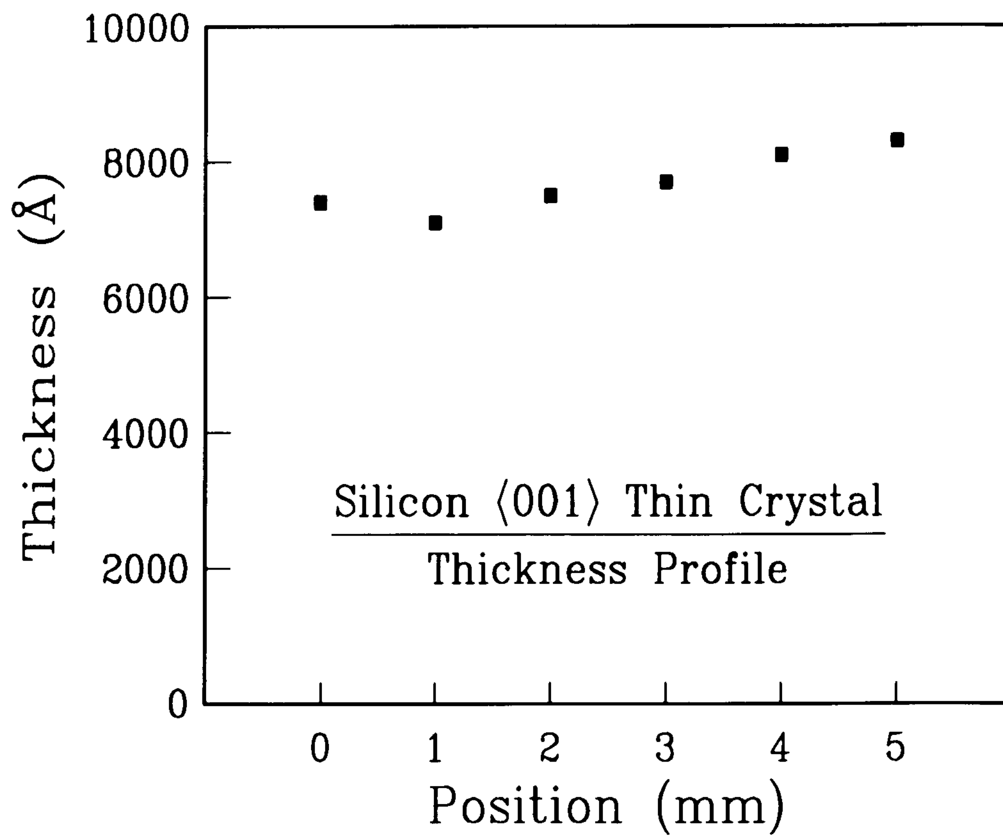

Figure 4.5 Thin film silicon (001) single crystal sample used for the energy loss and straggling measurements. Shown here is the plot of the thickness across its surface.

minimum by the end of the experiment had increased to 6%. Thus, the sample had suffered some radiation damage during many hours of proton bombardment, but not severe enough to affect the experimental results.

Data Analysis

Shown in Fig. 4.6 are the channeled and random spectra of the thin silicon sample. The "bump" in the middle is from silicon. The highest energy peak is from a 50-Å gold layer evaporated onto the sample surface, and the lowest peaks are from carbon contamination on the surface of the sample. The γ-ray spectrum of the $^{27}Al(p,\gamma)^{28}Si$ reaction can be found in chapter one (Fig. 1.7) and will not be repeated here. The characteristic γ-ray energy for the 0.992-MeV resonance is 10.8 MeV.

In order to obtain the energy loss and straggling profile across the channeling dip, two possible procedures presented themselves. One was to scan through the yield curve many times, i.e., for each different incident angle relative to the channeling minimum. The other was to stay at a given point on the yield curve and scan the angle over the complete channeling dip, and then advancing to the next point on the yield curve. Of course, this latter procedure requires considerable re-grouping of data points at the time of data analysis.

In practice, the second approach was preferable. In order to measure the

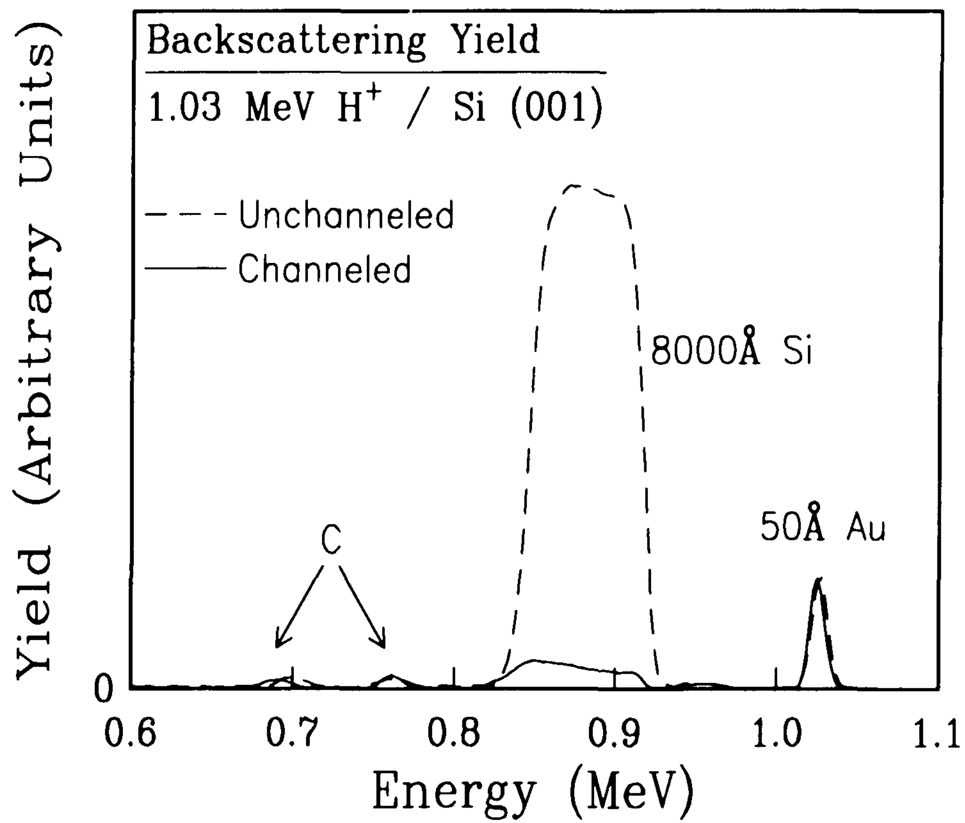

Figure 4.6 Backscattering spectrum of 1 MeV H^+ ion on (001) silicon thin film, random and channeled. The channeling dip from the near front surface region is about 4%.

yield function, it was necessary to change the energy of the incident proton beam, which was a slow procedure, and more importantly, could not be made automatic (at least at the present time). The angle scan, on the other hand, could be automated. Therefore the second method was adopted which allowed at least a few hours of continuous running without human intervention. The total time for the whole experiment was about 72 hours.

During the data acquisition process, the computer recorded the integrated counts from several regions of interest in both the backscattering and γ-ray spectra. Beam current, energy total orientation and total accumulated charge were also recorded for each run. The data were saved on disk for later analysis. Among the regions of interest saved were the backscattering yields from both the front and back side of the silicon sample, the gold layer, and the carbon peak. No channeling was discovered in the gold layer. Two regions of interest were recorded in the γ-ray spectra, similar to those used in chapter one (one region from 5 to 14 MeV, the other one from 9 to 14 MeV). The sample was moved to a fresh spot every a few hours to minimize the amount of radiation damage and carbon build-up.

The backscattering yield of the single crystal silicon (001) thin film

sample is plotted as a function of the incident beam angle relative to the crystal axis in Fig. 4.7. The half angle $2\Psi_{1/2}$ is $0.92^{\circ} \pm 0.03^{\circ}$. This is in close agreement with the published values. The near surface channeling dip is about 4%.

A close examination of the backscattering yield from the gold layer found no evidence of channeling in that layer. Since the backscattering cross section for gold is purely Rutherford, it can be used as a convenient normalization standard for other quantities, such as the backscattering yield from silicon and the γ-ray yield. This is generally considered to be better than relying on accumulated beam current (charge) normalization.

The γ-yield function of a thick target is the integration of the beam energy profile over the resonant width. If the beam energy distribution is a Gaussian, the thick target yield as a function of incident energy E_0 is given by Eqn. (1.1). In our case ρ and Ω(z) can be treated as constants and the result of the integration can be expressed in terms of the error function:

$$Y = A + B \operatorname{erf}\left(\frac{E - E_R'}{\sqrt{2}\,\Omega'}\right) \qquad (4.7)$$

where A is the background, B is the resonant strength, E_R' is the apparent

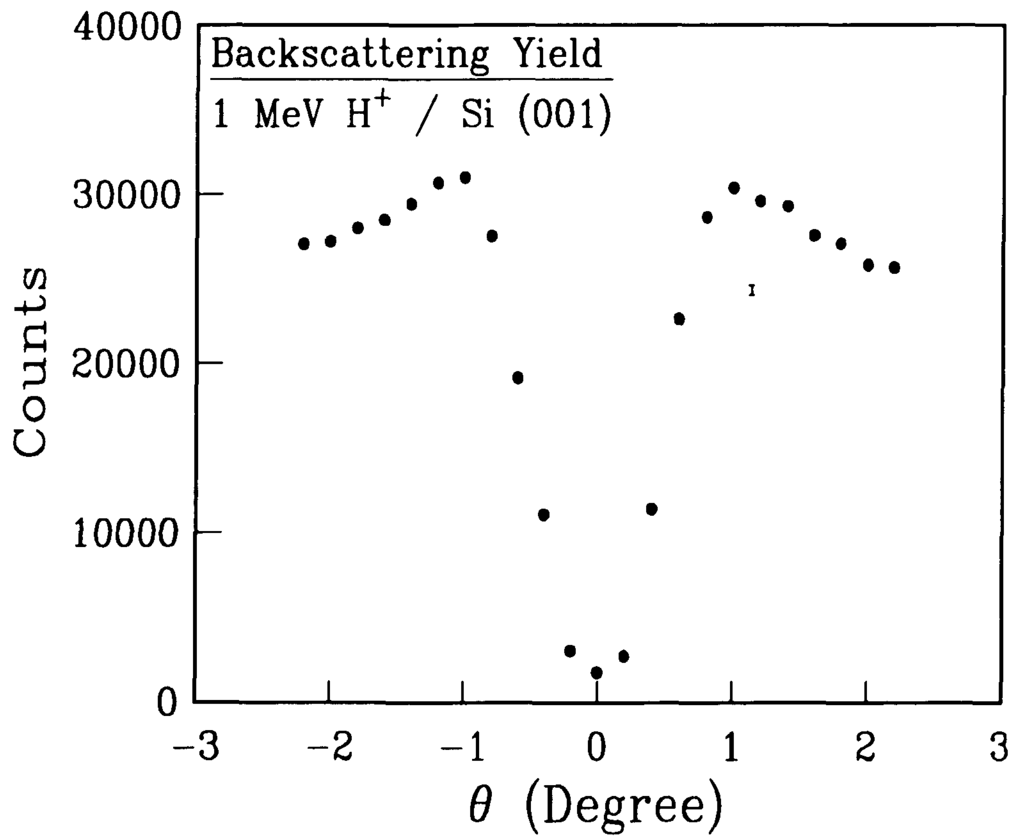

Figure 4.7 Backscattering yield of channeled 1 MeV H^+ near silicon (001). Representative error bar is shown. The half angle $2\Phi_{1/2}$ is 0.92°.

(shifted) resonant energy, and Ω' is the width of the beam energy distribution. The error function is defined as[52]

$$erf(x) = \frac{2}{\sqrt{\pi}} \int_0^x e^{-t^2} dt \tag{4.8}$$

The energy loss in the silicon layer can be obtained by subtracting from E_R' the true resonant energy,

$$E_R' = E_R + \left[\frac{dE}{dz}\right]_{Si} z_{Si} \tag{4.9}$$

and the straggling parameter is

$$\Omega^2 = \Omega'^2 - \Omega_0^2 \tag{4.10}$$

where Ω_0 is the beam energy width without silicon target.

A total of 23 sets of data were taken, one for each incident angle. Each set was fitted to the functional form of Eqn. (4.7) with A, B, E_R' and Ω' as fitting parameters. To further improve the overall fit, the background (A) and resonant strength (B) terms are were with all sets of data together. For subsequent fits to individual sets, these two parameters were fixed and only the energy and broadening parameters were allowed to vary. This substantially reduced the correlation coefficients between final fitting parameters. The error

bars of the fitted parameters were derived from the fitting matrix.[53] The normalized χ^2 value of the fits typically ranged from 1 to 2. Figure 4.8 shows some representative fits. Energy loss and straggling parameters were calculated from Eqns. (4.9) and (4.10). The results are summarized in Table 4.1.

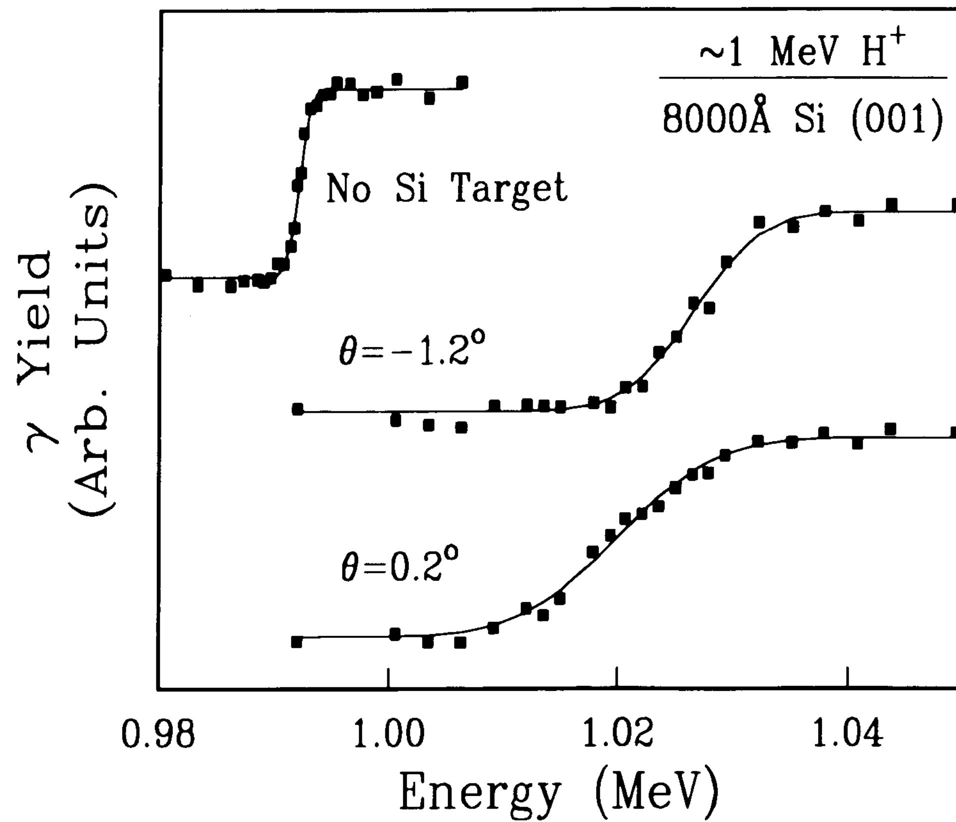

Figure 4.8 Representative least-squares fit of the γ-yield function to Eqn. (4.7).

Table 4.1 Results of energy loss and straggling measurements of 1 MeV H^+ on silicon near the (001) channeling minimum.

θ (Degree)	dE/dz (eV/Å)	Ω (keV)	θ (Degree)	dE/dz (eV/Å)	Ω (keV)
0.0	3.11	4.54		-	
0.2	3.51	6.49	-0.2	3.23	5.71
0.4	3.99	7.31	-0.4	3.92	6.88
0.6	4.19	6.43	-0.6	4.22	5.63
0.8	4.32	4.81	-0.8	4.40	5.64
1.0	4.33	4.11	-1.0	4.36	4.31
1.2	4.38	4.12	-1.2	4.32	4.24
1.4	4.38	4.26	-1.4	4.30	4.62
1.6	4.31	4.82	-1.6	4.30	4.46
1.8	4.29	3.94	-1.8	4.26	4.44
2.0	4.27	4.55	-2.0	4.23	4.11
2.2	4.27	3.55	-2.2	4.21	4.18

Discussion

Figure 4.9 shows the energy loss as a function of incident angle. The half angle $2\Psi'_{1/2}$ is $0.65° \pm 0.04°$, substantially smaller than the backscattering half angle, $2\Psi_{1/2}$. The solid line is a fit to the formula proposed by Jin *et al*[50], which is based on Lindhard's theory of the transverse energy distribution of channeled ions[45]

$$\frac{[dE/dz]_{Channeled}}{[dE/dz]_{Random}} = 1 - \alpha \kappa e^{-2\theta^2/\Psi_{1/2}^2} \qquad (4.11)$$

where $\Psi_{1/2}$ is simply taken from the half angle of the RBS dip. The dashed line is from the standard reference for the non-channeling case[22]. As can be seen from Fig. 4.9 there is excellent agreement between the data and Eqn. (4.11) for $|\theta| \leq 0.8°$, i.e., where the dip of energy loss occurs. It fails in the shoulder region because Eqn. (4.11) cannot produce the required overshoot. The overshoot is a direct consequence of the law of angular and spatial averaging, which states that the lower energy loss at the channeling minimum has to be compensated by other regions of higher than average energy loss.

The extracted straggling parameter is shown in Fig. 4.10 as a function of

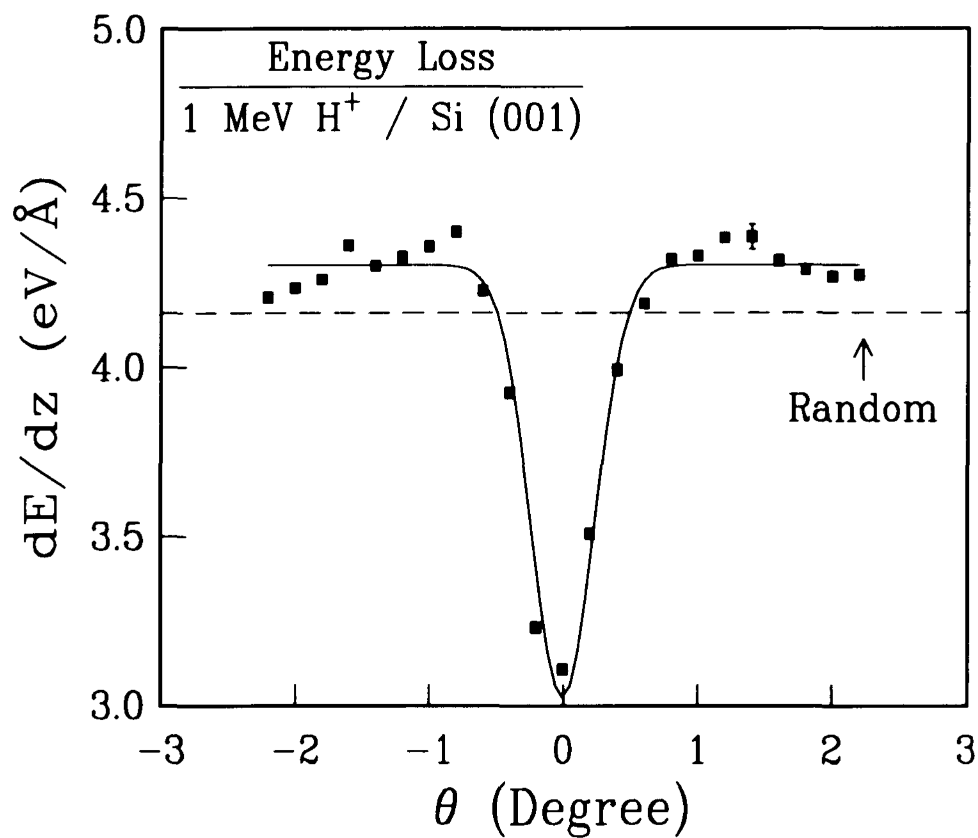

Figure 4.9 Energy loss of 1 MeV H^+ near silicon (001). Representative error bars are shown. Solid line is a fit to Eqn. (4.11). Dashed line is from ref. 22.

incident angle. The Bohr straggling (non-channeling) is indicated by the dashed line. At this energy most theories' predictions are actually not too far from the Bohr value.[37] The uncertainty in target thickness will add (in quadrature) about 2 keV to the straggling parameter, which was not corrected for in Fig. 4.10. (The correction will bring the experimental points closer to the Bohr straggling line, but not significantly.)

The behavior of the straggling parameter as a function of angle can be understood as follows. The two sides of the channeling dip represent the transition region from well channeled conditions to non-channeled. This is the region where projectiles with different transverse energy (or incident angle) are influenced differently by the target electron distribution. This is also the region where energy loss changes most rapidly with angle. Because of the way the straggling parameter is defined, a collection of projectiles with slightly different transverse energy will appear to have a much smeared-out distribution that is indistinguishable from straggling effects. For example, the angular dispersion of the incident beam was about 0.075°, more than adequate for a conventional channeling experiment. But this uncertainty in angle is estimated to contribute about 5 keV, in the worse case, to the apparent straggling parameter in the sloped region, more than enough to account for the scattering in data points.

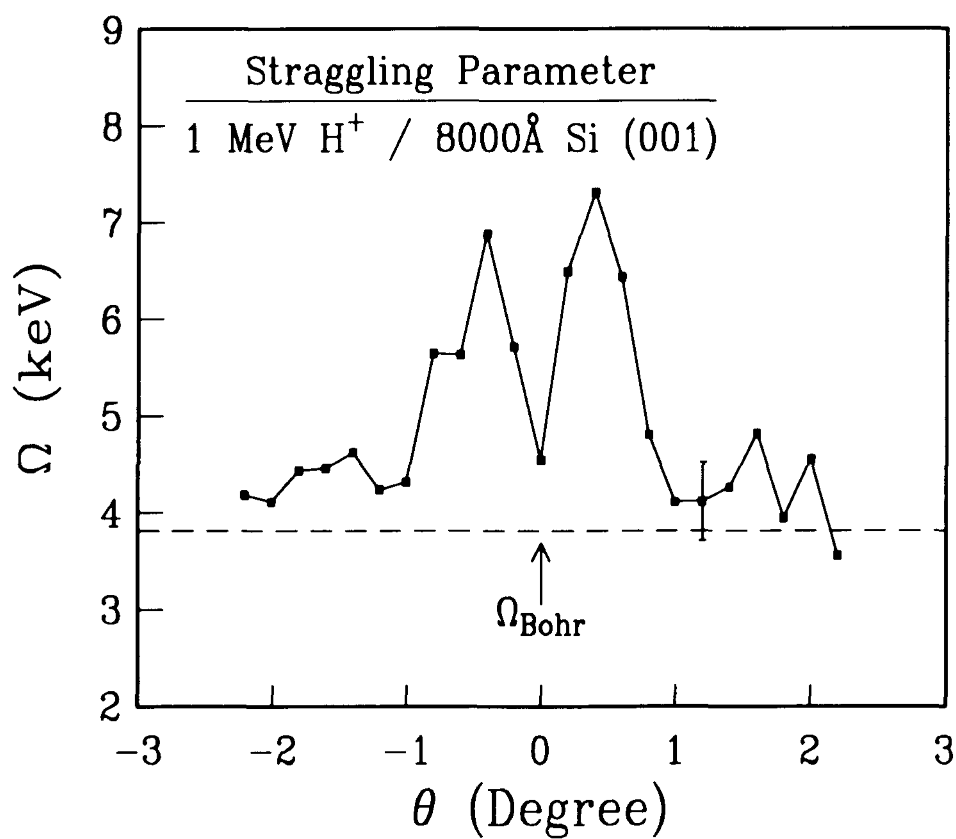

Figure 4.10 The straggling parameter of 1 MeV H^+ ions in silicon near the (001) channeling minimum as a function of incident angle. Representative error bars are shown.

In other words, the angular dependent straggling measurement is like taking a derivative of the angular dependent energy loss spectrum (and then the absolute value), sharpening the structures, thus requiring more stringent incident beam collimation. Reducing the divergence of the incident beam by a factor of 10 should render this artifact unimportant. This cannot be verified at the present time due to limitations of the accelerator and remains a challenge in future straggling measurements.

This averaging effect is also responsible for producing an outgoing beam energy distribution which deviates from a symmetric Gaussian. In their transmission channeling experiment, Jin and Gibson also observed an asymmetric energy profile with a long tail towards the low energy (i.e., higher energy loss) side.[50,51] This is consistent with the fact that a portion of the incident beam is not well channeled. They correctly picked the peak at higher-energies corresponding to well channeled ions. To judge the straggling from the width of their peak would lead to a plot similar to Fig. 4.10. In our case the fitting procedure for energy loss is, to a first approximation, not affected by any asymmetric features. The straggling, however, will contain contributions from well-channeled and not-so-well-channeled ions convoluted together.

Appendix

There are a few ways to estimate the change in sample temperature during the ion implantation procedure. The following numbers will be used in the calculations (the properties of GaAs are from Ref. 54):

energy of ion,	$E = 80\ \text{keV} = 1.5\times10^{-14}$ J
implantation dosage,	$D = 1\times10^{15}\ \text{cm}^{-2}$
total sample thickness,	$z_0 = 0.1$ cm
specific heat,	$C = 0.35$ J/g-°C
heat conductivity,	$k = 0.46$ J/cm-sec-°C
density,	$\rho = 5.3\ \text{g/cm}^3$

First consider the case of equilibrium heat flow, in which the energy deposited by the implanted ions is carried away by the sample to the sample holder,

$$D\ A\ E = \frac{k\ \Delta T\ A\ t}{z_0} \tag{A.1}$$

or

$$\Delta T\, t = \frac{D\, E\, z_0}{k} \approx 2\ {}^0C\cdot\text{sec} \tag{A.2}$$

where A is the area of the sample, ΔT is the temperature difference across the sample thickness z_0, and t is the implantation time. Since the implantation time is much greater than one second, ΔT can be at most a few degrees.

A more conservative approach is to consider the sudden impact (adiabatic) approximation. The solution to the heat conductivity equation,

$$\frac{\partial T}{\partial t} = \frac{k}{C\rho}\frac{\partial^2 T}{\partial z^2} \tag{A.3}$$

with the initial condition $T(z,t=0) = T_0\delta(z)$ is

$$T(z,t) = T_0\left[\frac{C\rho}{\pi k t}\right]^{1/2} \exp\left[-\frac{C\rho z^2}{4kt}\right] \tag{A.4}$$

The time required for the temperature to reach equilibrium over a depth scale of z_0 is

$$\frac{C\rho z_0^2}{4kt} \approx 1 \tag{A.5}$$

or

$$t \approx \frac{4kz_0^2}{C\rho} \approx 0.1 \text{ sec} \tag{A.6}$$

For an ion implantation procedure substantially slower than the above time scale, the sample as a whole absorbs the energy of the implanted ions. The maximum temperature rise of the sample due to ion implantation is

$$D\ A\ E = C\ \rho\ (Az_0)\ \Delta T \tag{A.7}$$

or

$$\Delta T = \frac{DE}{C\rho z_0} \approx 80\,^{o}C \tag{A.8}$$

This result represents an upper limit on the possible temperature change of the sample.

Bibliography

1. R. D. Dupuis and P. D. Dapkus, IEEE J. Quantum Electron. **QE-15**, 128 (1979).

2. N. Holonyak, Jr., R. M. Kolbas, W. Laidig, E. A. Vojak, R. D. Dupuis, and P. D. Dapkus, in *Gallium Arsenide and Related Compounds*, Inst. Phys. Conf. Ser. **45**, 387 (1979).

3. P. M. Solomon, Proc. IEEE **70**, 489 (1982).

4. H. J. Hovel and J. M. Woodall, J. Electrochem. Soc. **120**, 1246 (1973).

5. H. C. Hamaker, C. W. Ford, J. G. Werthen, G. F. Virshup, N. R. Kaminar, D. L. King, and J. M. Gee, Appl. Phys. Lett. **47**, 762 (1985).

6. S. M. Ku and J. F. Black, J. Appl. Phys. **37**, 3733 (1966).

7. H. C. Casey, Jr. and M. B. Panish, J. Appl. Phys. **40**, 4910 (1969).

8. M. B. Panish and S. Sumiski, J. Phys. Chem. Solids **30**, 129 (1969).

9. O. Berelo and J. C. Wooley, Can. J. Phys. **49**, 1335 (1971).

10. B. Monemar, K. K. Shih, and G. D. Pettit, J. Appl. Phys. **47**, 2604 (1976).

11. N. C. Miller, S. Zemon, G. P. Werben, and W. Powazinik, J. Appl. Phys. **57**, 512 (1985).

12. *Methods of Surface Analysis*, edited by A. W. Czandera, Elsevier publishing, New York, (1975).

13. R. Dingle, R. A. Logan, and J. R. Arthur, Inst. Phys. Conf. Ser. A **33**, 210 (1977).

14. D. E. Aspnes, S. M. Kelso, R. A. Logan, and R. Bhat, J. Appl. Phys. **60**, 754 (1986).

15. J. S. Rosner, P. M. S. Lesser, F. H. Pollak, and J. M. Woodall, J. Vac. Sci. Tech. **19**, 584 (1981).

16. S. C. Wu, A. Cheng, and C. H. Pao, J. Appl. Phys. **60**, 2175 (1986).

17. D. Yan, J. P. Farrell, P. M. S. Lesser, F. H. Pollak, T. F. Kuech, and D. J. Wolford, Nucl. Inst. Meth. Phys. Res. B **24/25**, 662 (1987).

18. T. F. Kuech, D. J. Wolford, R. Potemski, J. A. Bradley, K. H. Kellher, D. Yan, J. P. Farrell, P. M. S. Lesser, and F. H. Pollak, Appl. Phys. Lett. **51**, 505 (1987).

19. R. D. Evans, *The Atomic Nucleus*, McGraw-Hill publishing, New York, (1955).

20. *Ion Beam Handbook for Material Analysis*, edited by J. W. Mayer and E. Rimini, Academic Press, New York, (1977).

21. W. K. Chu, J. W. Mayer, and M. A. Nicolet, *Backscattering Spectrometry*, Academic Press, New York, (1978).

22. J. F. Ziegler, *Hydrogen Stopping Cross Sections in All Elements*, Pergmon Press, New York, 1977; The ZBL stopping cross section code for IBM/PC, (1985).

23. D. Huang, G. Ji, U. K. Reddy, H. Morkoc, F. Xiong, and T. A. Tombrello, J. Appl. Phys. **63**, 5447 (1988).

24. G. L. Holleck, K. M. Abraham, P. B. Harris, J. L. Goldman, J. Avery, M. W. Rupich, and S. B. Brummer, Proc. Electrochem. Soc. **82**, 68 (1982).

25. See, for example, J. J. Auborn, Y. L. Barberio, K. J.Hanson, D. M. Schleich, and M. J. Martin, J. Electrochem. Soc. **134**, 580 (1987) and references therein.

26. R. N. Bhattacharya, C. Y. Lee, F. H. Pollak, and D. M. Schleich, in *Disordered Semiconductors*, edited by M. A. Kastner, G. A. Thomas, and S. R. Ovshinsky, Plenum Publishing, New York, (1987); R. N. Bhattacharya, C. Y. Lee, F. H. Pollak, and D. M. Schleich, J. Non. Crystalline Solids, **91**, 235 (1987).

27. R. N. Bhattacharya, D. Yan, P. M. S. Lesser, F. H. Pollak, and D. M. Schleich, Proc. Electrochem. Soc. **88**, 443 (1988).

28. C. Sourisseau, O. Gorochov, D. M. Schleich, Mater. Sci. Eng. B **3**, 113 (1989).

29. R. N. Bhattacharya, C. Y. Lee, F. H. Pollak, and D. M. Schleich, J. Non-Cryst. Solids **91**, 235 (1987).

30. J. B. Marion and F. C. Young, *Nuclear Reaction Analysis, Graphs and Tables*, North Holland Publishing, Amsterdam, (1968).

31. L. Doolittle, the RUMP RBS simulation and analysis code for IBM/PC, (1986).

32. G. Laperrier, B. Marson, D. Gelanger, Synth. Met. **29**, F2011 (1988).

33. J. R. Cameron, Phys. Rev. **90**, 839 (1953).

34. N. Thangprasert, P. A. Montano, D. L. Price, B. R. Cooper, E. Ziegler, I. K. Shuller, Y. Chan, H. S. Jin, D. Yan, and P. M. S. Lesser, Mat. Res. Soc. Sym. Proc. **122**, 589 (1988).

35. Y. L. Chan, Ph. D. Thesis, The City University of New York, (1992).

36. R. W. Hill, Phys. Rev. **90**, 845 (1953).

37. N. Bohr, Philos. Mag. **30**, 581 (1915); Mat. Fys. Medd. Dan. Vid. Selsk. **18**, no. 8 (1948).

38. H. Bethe, Ann. Phys. **5**, 325 (1930).

39. F. Bloch, Ann. Phys. **16**, 285 (1933); Z. Phys. **81**, 363 (1933).

40. J. Lindhard, and M. Scharff, Mat. Fys. Medd. Dan. Vid. Selsk. **27**, no. 15 (1953).

41. W. K. Chu, and D. Powers, Phys. Lett. A **38**, 267 (1972).

42. W. K. Chu, Phys. Rev. A **13**, 2057 (1976).

43. W. H. Bragg, and R. Kleeman, Phil. Mag. **10**, S318 (1905).

44. D. S. Gemell, Rev. Mod. Phys. **46**, 129 (1974).

45. J. Lindhard, Mat. Pys. Medd. dan. Vid. Selsk, **34**, no. 14 (1965).

46. B. R. Appleton, C. Erginsoy, and W. M. Gibson, Phys. Rev. **161**, 330 (1967).

47. H. Esbensen, and J. A. Golovchenko, Nucl. Phys. A **298**, 382 (1978).

48. A. Bond, P. Parayanthal, F. H. Pollak, and J. M. Woodall, J. Appl. Phys. **55**, 3433 (1984).

49. Y. Kido, and T. Hioki, Phys. Rev. B **27**, 2667 (1983); Y. Kido, Phys. Rev. B **34**, 73 (1986).

50. H. S. Jin, and W. M. Gibson, Nucl. Instr. Meth. Phys. Res. B **13**, 76 (1986).

51. H. S. Jin, Ph. D. Thesis, SUNY at Albany, (1985).

52. M. Abramowitz, and I. A. Stegun, *Handbook of Mathematical Functions*, Dover publishing, New York, (1965).

53. The non-linear fit routines were adopted from W. H. Press, B. P. Flannery, S. A. Teukolsky, and W. T. Vetterling, *Numerical Recipes, the Art of Scientific Computing*, Cambridge University Press, New York, (1986).

54. S. M. Sze, *Physics of Semiconductor Devices*, 2nd edition, John Wiley and Sons, New York, (1981).